HIERARCHICAL MODEL OF GAS EXCHANGE WITHIN THE ACINAR AIRWAYS OF THE HUMAN LUNG

A Dissertation presented to

the Faculty of the Graduate School

University of Missouri

Submitted in Partial Fulfillment

of the Requirements for the Degree

of

Doctor of Philosophy

---

by

MICHAEL LOUIS MAYO

Dr. Peter Pfeifer, Dissertation Supervisor

JULY 2009

The undersigned, appointed by the Dean of the Graduate School, have examined the dissertation entitled:

HIERARCHICAL MODEL OF GAS EXCHANGE WITHIN THE ACINAR AIRWAYS OF THE HUMAN LUNG

presented by MICHAEL LOUIS MAYO

a candidate for the degree of Doctor of Philosophy

and hereby certify that in their opinion it is worthy of acceptance.

Dr. Peter Pfeifer

Dr. Virginia Huxley

Dr. Shi-Jie Chen

Dr. Ioan Kosztin

Dr. Carlos Wexler

ACKNOWLEDGMENTS

I will never be able to adequately express my appreciation to Dr. Peter Pfeifer, for his years of support in the production of this work. From him I learned how to approach important questions and how to conduct professional scientific research. I have always been impressed by his deep wisdom and powerful physical insights, of which he has always shared with me enthusiastically. It has truly been a pleasure to work alongside such an outstanding scientific figure.

I want to thank the members of my thesis committee for their friendly suggestions, which allowed me to improve upon the present work. In particular, I thank Dr. Virginia Huxley for her comments, Dr. Ioan Kosztin for teaching me a great deal about systems far from equilibrium, and Dr. Shi-Jie Chen for reviewing this work on short notice.

In my personal life, there is no one person I am indebted to more than my wife, Anne Marie Mayo. Without her constant love and unwavering support, I would have had a more difficult time throughout my years in graduate school. Anne not only provided a shoulder to lean on in difficult times, but as a gifted biologist she has also contributed greatly to the present document through her insightful comments and her work in editing the many drafts of this document. Without her help in this capacity, the present document would have had a very different flavor.

I thank my parents, whom have played a pivotal role in the path that I have followed to graduate school. I find myself very fortunate to have their love and support in the decisions I have made throughout the course of my early life.

I also want to recognize the appreciation I have for everyone who has recently helped me and Anne take care of our new baby. Any parent may understand the difficulties that arise in completing such a large project on a tight deadline in parallel with the care of a newborn child. Their help was critical to the successful and timely completion of this work, and I thank them all for their generous support in these difficult times.

Contents

List of Tables

List of Figures

Abstract

The acinar airways lie at the periphery of the human lung and are responsible for the transfer of oxygen from air to the blood during respiration. This transfer occurs by the diffusion-reaction of oxygen over the irregular surface of the alveolar membranes lining the acinar airways. We present an exactly solvable diffusion-reaction model on a hierarchically branched tree, allowing a quantitative prediction of both the pulmonary efficiency of the human lung and the oxygen current reaching the blood within the pulmonary arteries, over the entire system of acinar airways responsible for the gas exchange. Our model predicts that the oxygen current is insensitive to changes in the permeability of the alveolar membranes, over a wide range of permeabilities. Such fault tolerance has been observed in other treatments of the gas exchange in the human lung and is obtained here as a fully analytical result.

Chapter 1

Introduction

Oxygen transport within the human lung has been studied extensively, both numerically and experimentally [5, 6, 7, 8, 9, 2]. Though much is known about the general function of the human lung, investigations relating its structure to its function have been sparse. Few models exist, either numeric or analytic, that make accurate, quantitative predictions of either the pulmonary efficiency of the lung or of the oxygen current transported to the blood from the air–a process intimately coupled with the survival of an organism. The lack of quantitative models is exacerbated by the fact that, until very recently, it was essentially unknown that the transmembrane oxygen current could be inferred from experimental data available for the lung. To the best of our knowledge, Hou and his collaborators recently reported the first such estimates of the oxygen current from the available physiological data.[1]

Particularly insightful are accurate analytic models of the non-equilibrium transport of oxygen within the lung, as they hold the promise of allowing one to elucidate the connection between the lung's structure and its function as a gas exchanger. To the best of our knowledge only one such analytic model currently exists[10, 1], in which physiological data has been applied to make quantitative predictions of the oxygen current reaching the blood. In this thesis we will develop a new model of the gas exchange system, and we will provide independent evidence of several features observed in other treatments.

Previous studies of the gas exchange within the mammalian lung have focused mainly

on numerical simulations of oxygen transfer across several model geometries for the global structure of its alveolar membranes.[5, 9] Recently, Hou et al.[10, 1] and Grebenkov et al.[11] have proposed two very different analytic models of oxygen transfer within the lung; however, only Hou and his collaborators make predictions with comparisons against experimental data. Hou's renormalization model allows one to study the alveolar membranes as a space-filling structure, and this model performs remarkably well compared with the available experimental data.

We consider the transport of oxygen from the air to the blood as a process which is dependent upon several factors, and a central hypothesis in this thesis is that the surface area of the alveolar membranes plays a critical role in its transport to the blood. From previous studies of the gas exchange process, it is not entirely clear which properties of the lung are evolutionary advantageous against environmental stressors. The global operating principles that the respiratory structure utilizes in its delivery of oxygen to the blood also remain unknown.

In this thesis we propose a new model for an acinar branch in which the diffusional screening of oxygen from the alveolar membranes will play a critical role in regulating the transmembrane oxygen current binding to the red blood cells within the pulmonary arteries. We then develop an analytic model of the gas exchange within the acinar airways, and we use this model to make quantitative predictions for the transmembrane oxygen current and pulmonary efficiency of the human lung acinus.

Our model of gas exchange is motivated by the recent discovery of a new interpretation for a transport parameter appearing within the diffusion-reaction equations of motion for oxygen within the acinar airways, and is called the "exploration length."[12, 10, 1] The exploration length depends upon two transport parameters of the system and has units of length. Until recently, its physical interpretation has largely remained a mystery.

To the best of our knowledge, two groups are essentially responsible for the development of a physical interpretation for the exploration length. Pfeifer et al.[13, 12], and Sapoval et al.[14, 15] suggested that the exploration length measures the effective length along the alveolar membranes which a molecule explores before it usually crosses them, and for this

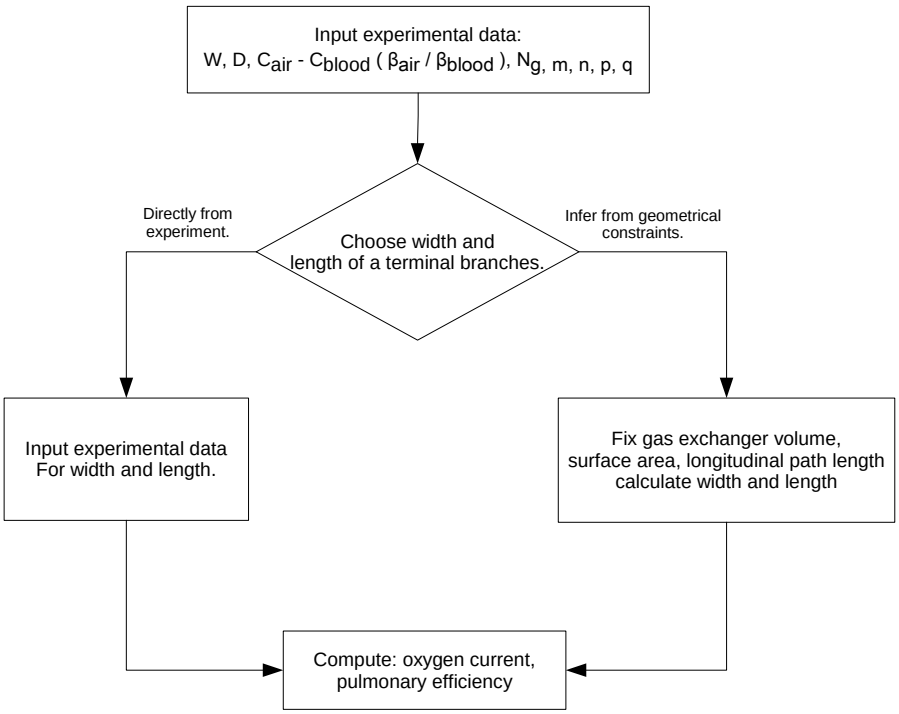

Figure 1.1: Flow chart describing a simple algorithm in the prediction of the oxygen current and pulmonary efficiency.

reason they called it the "exploration length." The existence of such a length scale implied that only geometric considerations were needed to approximate oxygen transport to the blood, and Hou et al. renormalized the alveolar membranes using the exploration length as a measure of the alveolar membranes surface area used in transport.[10, 1]

Here we develop a new analytic model for the prediction of the oxygen current reaching the hemoglobin of the red blood cells within the pulmonary arteries of the lung. Our model reproduces behavior observed in other treatments of the airways[10, 1] and provides independent evidence of the homeostatic regulation of oxygen delivered to the blood under changing demands from the body. Few steps are needed to make predictions of the transmembrane oxygen current and pulmonary efficiency of the lung, and we outline this algorithm in Figure 1.1.

In chapter 2 of this thesis, we will review and discuss those aspects of the lung's physiology that we deem to be important in the transport of oxygen. We then proceed to review the mathematical formulation of the boundary driven diffusion-reaction model frequently

used to describe the transport of oxygen to the blood within the acinar airways. Finally, we will discuss recent developments in the treatment of the diffusion-reaction problem, which includes the exploration length and its significance as a tool in the measurement of diffusional screening.

In chapter 3 we will propose a new model of an acinar branch, report its development, and conduct an analysis by comparing our model with an exact solution for for the particle concentration in the model branch. We will describe two mathematical constructions of the concentration within the model branch and identify conditions under which both treatments describe equivalent dynamics across the model branch. We will also calculate the particle current for the model branch, and compare the result against predictions for the convergence of solutions within both mathematical treatments of the branch.

In chapter 4 we will extend our model of a single acinar branch to the entire branching structure of the acinar airways. We will provide evidence suggesting that our branching model reproduces an insensitivity to membrane permeability that has recently been reported by other authors[10, 1]. Specifically, we will show that as the tree increases in size, its robust behavior extends over several orders of magnitude of membrane permeability. Our results suggests that the mammalian lung adopts a structure which optimally configured to balance the efficient delivery of oxygen to the blood with an ability to mitigate damage to its tissues.

We then discuss geometric aspects of the Cayley tree within chapter 5. We will investigate the conditions under which the scaling exponent of the tree canopy, thus its fractal dimension is equivalent to the scaling exponent described by its dimension generating functions–which approximate the Hausdorff dimension of the tree and its canopy. The advantage of the dimension generating function is that it provides a simple, analytic, way of expressing the scaling exponents for the tree. From our analysis we will quantify the space-filling ability of the tree with its fractal dimension, and use this result to extend the equi-length and width model of chapter 4 to a fractal representation of the model.

In chapter 6 we will study the space-filling ability of the tree and investigate several advantages of such a configuration. These results will provide insight into the engineering advantages of the lung's architecture and may provide an explanation for this structure in

terms of an optimization scheme designed to maximize delivery of oxygen to the blood.

In chapter 7 we apply experimental data to our model, and use the result to make predictions of the oxygen current reaching the blood, and of the pulmonary efficiency of the gas exchanger. Specifically, we outline two methods by which we will apply physiological data to our model and discuss the predictions and significance of each.

Chapter 2

Review

2.1 Introduction

In this chapter we will review the relevant background material necessary as a foundation in the development of our model of the human lung. We begin with a brief discussion of the biology and physiology of the lung and its structure and role as an acinar gas exchanger. Within the context of this review, we consciously omit many topics, and several excellent sources exist to supplement our presentation. See, for example, references [4, 3, 16].

We will continue with a brief overview of the standard mathematical formulation for a diffusion-reaction system, and we report the diffusion equation for the oxygen concentration, relevant within the context of our mathematical model. For an introduction to diffusion-reaction systems within the context of the Fokker-Plank equation, see ref. [17].

We conclude our review with a discussion of several major recent developments within the description of oxygen diffusion through the human lung acinus. We will emphasize those developments that directly motivated the construction of our model branch, and we will present a brief discussion of the exploration length, and its implications for the screening of surface sites on the membranes.

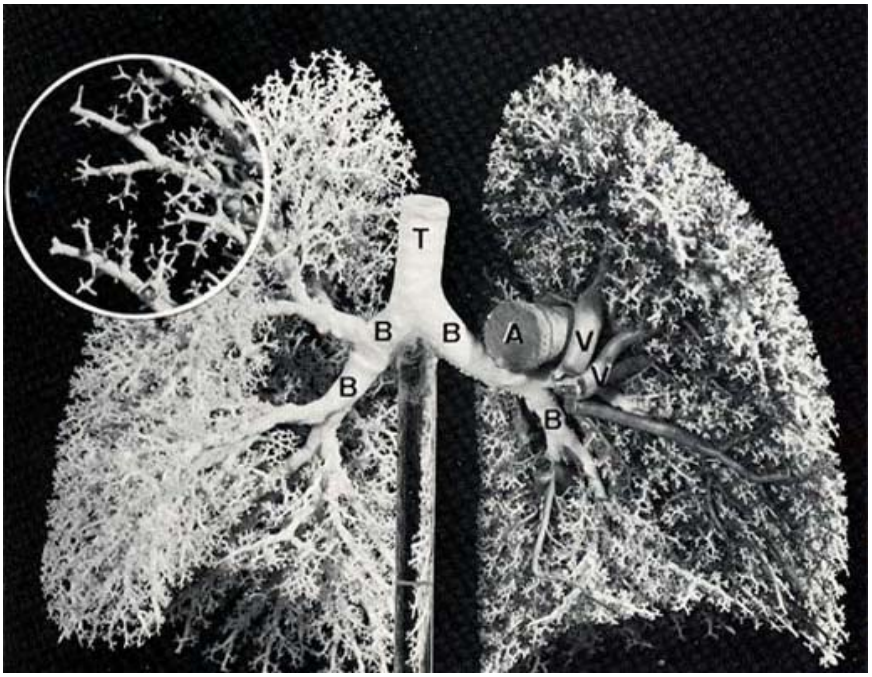

Figure 2.1: Resin cast of the airways within the human lung [3].

2.2 Human lung physiology in the context of oxygen transport

Respiration may be characterized by two processes: inhalation and exhalation. During inhalation, air passes to the trachea, where it propagates through the bronchial tree by convection and is ultimately absorbed into the blood for distribution throughout the body. Exhalation serves to remove carbon dioxide from the body–a by-product of ATP synthesis. Transport of oxygen to the blood during inhalation is, arguably, the dominant role of the human lung.[3] The ability of an organism to remove carbon dioxide from the body is, however, equally necessary for the survival of an organism. In this thesis, we focus exclusively on the transport of oxygen to the hemoglobin of the red blood cells and develop a model to predict its current; however, the model of acinar gas exchange we present may also be used to describe the transport of carbon dioxide from the blood to the air with an appropriate choice of input parameters.

We will take the transport of oxygen from the air to the blood as a series of several

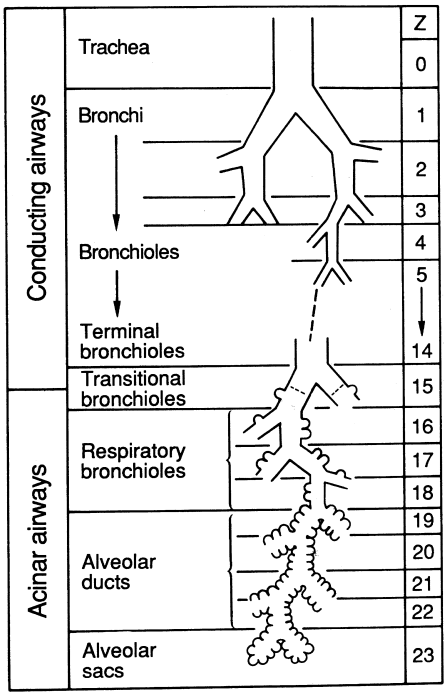

Figure 2.2: Organizational structure of the airways in the human lung [3].

intermediate processes. First, we will consider the convective transport of oxygen through the bronchial tree, until a molecule's diffusional speed falls below its convective speed. Next, we will consider the transport of oxygen, under diffusion, to the distal regions of the airways. Finally, we will consider the transport of oxygen across the alveolar membranes and its subsequent uptake by the hemoglobin within the red blood cells.

We define the bronchial tree to be those portions of the lung airways that are "...purely conducting structures whose main function is to move the air into the peripheral units."[3] Our definition includes the trachea, and continues to describe those dichotomously branching airways in which convection is exclusively the dominant transport process. An illustration of the branching airways of the bronchial tubes is shown in Figure 2.1.

An epithelial cell sheet lines the airways of the bronchial tree, such that the cells form a tightly-packed, gapless surface. Therefore, as oxygen is moved by convection through the bronchial tree it does not usually cross the junctions between cells in the epithelium. Below the basement membranes of the epithelial layer in the bronchial tree is a layer of smooth muscle cells, and below the smooth muscle cells is another layer of cartilage.

The branches in the bronchial airways split dichotomously into daughter branches at the

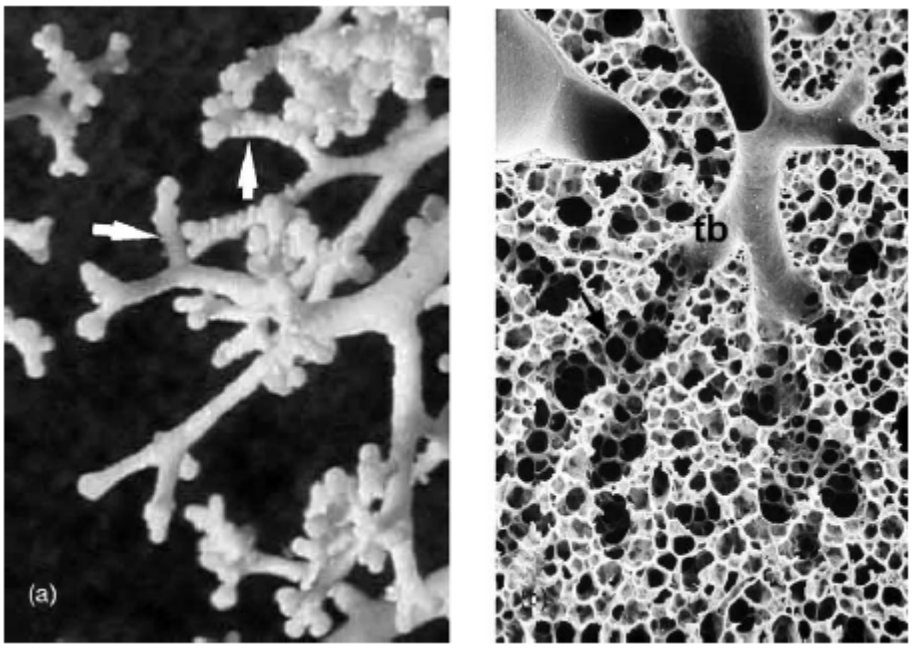

(a) (b)

Figure 2.3: (a) Resin cast of the human lung and (b) an electron micrograph of perfusion-fixed rabbit lung [2].

end of each of its parent branches. The total cross-section of the bronchial tree increases exponentially as oxygen moves deeper toward its distral regions, and its convective speed eventually falls below its diffusional speed. Those airways in which oxygen is transported by both convection and diffusion are called the transitionary bronchioles. Figure 2.2 illustrates the organizational structure of the human lung and reports that the transitionary bronchioles appear near the fifteenth branching generation.

In the transitionary bronchioles, the epithelial layer of the airway walls is much thinner than those in the bronchial tree, and contains essentially no cartilage and very little smooth muscle cells below the basement membranes. The permeability of the cell membranes is related to the global permeability of the alveolar membranes because the junctions between the cells within the epithelial layer form gaps which compose a tiny fraction of the total surface area of the alveolar membranes.

The transition from convective to diffusive transport is not only characterized by a thinning of the airway walls, but also by the appearance of alveolar sacs that begin to

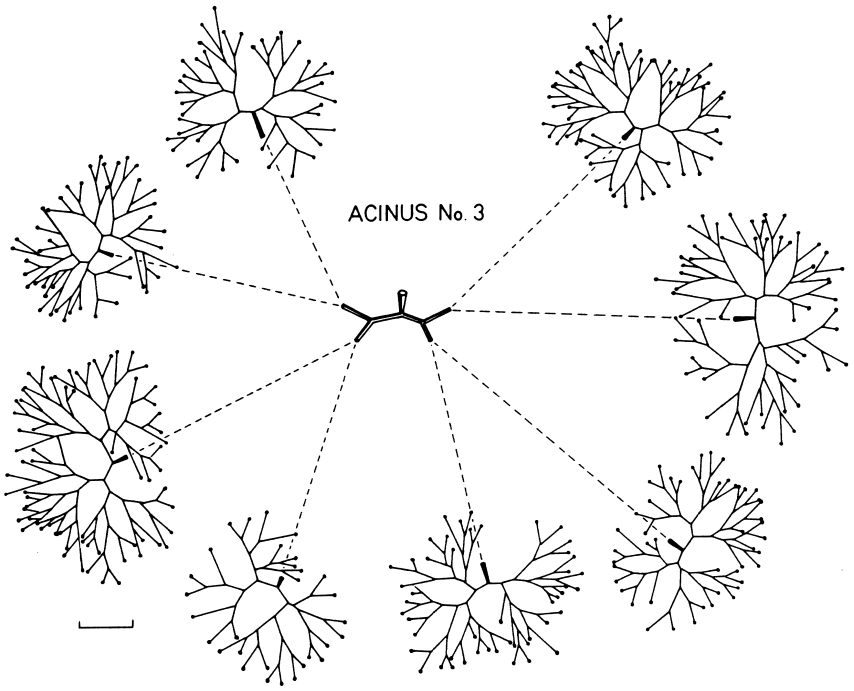

Figure 2.4: Topological structure of several 1/8 subacini [4].

populate the walls in the transitionary bronchioles. The membranes lining the alveoli are the main workhorse of the gas exchange process within the human lung. These membranes are very thin, and are composed of both an epithelial and endothelial layer of cells joined by the fusion of their basement membranes. The alveoli themselves are typically tightly packed, and their membranes appear to form a space-filling surface in contact with the acinar gas.[10, 18]

We adopt a definition of the human lung acinus from Weibel[4], and define it to be "...the largest parenchymal lung unit in which all airways are alveolated and participate to some degree, in the gas exchange process." Our adoption of this definition excludes the transitionary bronchioles from consideration within the acinar airways, and we will assume that diffusion is exclusively the mechanism by which oxygen is transported within a single gas exchanger of the human lung.

The airways of the lung acinus are those that are exclusively alveolated, thus the walls of the acinar ducts are completely populated by alveoli. The ends of the terminal branches in the human lung acinus are also covered with alveolar sacs. Figure 2.3(b) presents a

scanning electron micrograph of a perfusion-fixed rabbit lung, and one can clearly observe the transition from the smooth-walled bronchioles into the alveolated ducts of the acinar airways.

The alveolar epithelium is composed of two cell types: type I (EP1) and type II (EP2). Type II cells play a fundamental role in the acinar gas exchange, as their principle function is "...the synthesis, storage, and secretion of surfactant."[3] The surfactant secreted by type II alveolar epithelial cells is composed of proteins and phospholipids that spread homogeneously across the membranes to produce a thin barrier, which partitions the acinar gas from the tissue of the alveolar membranes. The primary function of this thin film is to attenuate the surface tension of the membranes, affecting their global mechanical stability.

The collection of alveolar sacs is not independently mechanically stable. Furthermore, alveolar surfactant couples with the alveolar membranes to decrease their surface tension under a decrease in alveolar volume, while increasing their surface tension under an increase in alveolar volume. Therefore, surfactant plays a critical role in the mechanical equilibrium of the alveoli within the pulmonary acinus of the human lung, working to prevent their collapse.

Diseases of the lung which affect the secretion of alveolar surfactant from its type II cells can impact oxygen transport in dramatic ways. For example, prematurely delivered infants may lack the necessary development of their type II cells of the alveolar epithelium affecting the lung's ability to sufficiently generate alveolar surfactant to maintain the mechanical equilibrium of their alveolar membranes. Therefore, the mechanical stability of the alveolar membranes becomes compromised, and large portions of the airways collapse. Ventilation of the alveolar membranes then decreases, and the partial pressure of oxygen decreases such that the airways fail to provide enough oxygen to the blood to meet the body's demand.

Several interesting aspects of the topological structure of the acinar airways exist, and examples of the branching structure of several acini appear within Figure 2.4. The acinar ducts conserve the branching symmetry of the bronchial tree and continue to split dichotomously across each generation within the acinus. Interestingly, the mean length and diameter of the acinar ducts, as reported by Weibel et al. [4], appear to be conserved across

each branching generation within the airways of the lung acinus.

We conclude our review of the structure and physiology of the airways within the human lung by summarizing several main points of interest. We found that the conducting airways of the bronchial tree branch dichotomously, and the acinar ducts of the human lung acinus conserve this structure. We adopted a working definition of the acinar airways, summarized as those airways in the human lung that are exclusively alveolated. Finally, we saw that the transport mechanism of oxygen propagation within the acinar airways is diffusion, and that the alveolar membranes remain mechanically stable under normal operating conditions.

2.3 Mathematical description of diffusion

2.3.1 Fokker-Plank equation

We will represent the diffusion of oxygen through the acinar airways as a Markov process. The probability of finding a molecule at coordinates $(\vec{x}, t)$ is given by

$$p(\vec{x}, t|\vec{x}_0, t_0) = \int d^3x' p(\vec{x}, t|\vec{x}', t')p(\vec{x}', t'|\vec{x}_0, t_0). \tag{2.3.1}$$

Without a loss of generality, we take the system to be one dimensional. Therefore, we seek an equation of motion for the transition probability, $p(x, t|x_0, t_0)$, which we can find directly from Equation 2.3.1, through the application of the forward Kramers-Moyal expansion [17]:

$$\partial_t p(x, t|x_0, t_0) = \mathcal{L}p(x, t|x_0, t_0) \tag{2.3.2a}$$

$$\mathcal{L} := \sum_{n=1}^{\infty} \left(-\frac{\partial}{\partial x}\right)^n D^{(n)}(x, t). \tag{2.3.2b}$$

$\mathcal{L}$ is the Kramers-Moyal operator and

$$D^{(n)}(x, t) = \lim_{\tau \to 0} \frac{M_n(x, t, \tau)}{\tau n!} \tag{2.3.3a}$$

$$M_n(x, t, \tau) := \int dy (y - x)^n p(y, t + \tau|x', t'). \tag{2.3.3b}$$

Thus, the calculation of the transition probability is reduced to the study of the eigenfunctions of an appropriate operator for the system of study.

We will connect the probability density to the concentration of a diffusing species by noting that the concentration within the domain may be found from the initial concentration through

$$C(x,t) = \int dx_0 p(x,t|x_0,0)C(x_0,0).$$

In the absence of an external potential, Equations 2.3.2 and 2.3.3 give, for $n = 2$,

$$\partial_t C(x,t) = D\partial_x{}^2 C(x,t), \tag{2.3.4}$$

where $D^{(1)}(x,t) = 0$ and $D^{(2)}(x,t) = D$ are calculated through the associated Langevin equation. The extension to three spacial dimensions is straightforward and gives

$$\partial_t C(\vec{x},t) = D\vec{\nabla}^2 C(\vec{x},t). \tag{2.3.5}$$

2.3.2 Diffusion-reaction of oxygen

In Section 2.3.1 we reviewed a mathematical description of oxygen diffusion within an arbitrary domain, and in this section we apply these results to the physical restrictions within the lung acinus. We assume that after averaging across many inhalation and exhalation cycles the resulting oxygen concentration distribution is independent of time. Equation 2.3.5 will then reduce to

$$\vec{\nabla}^2 C_{air}(\vec{x}) = 0, \tag{2.3.6}$$

where we have labeled $C_{air}(\vec{x})$ as the oxygen concentration in the acinar gas, measured at a position $\vec{x}$ within an arbitrary coordinate system of the acinar airways.

The Diffusion Equation, Equation 2.3.5, satisfies an equation of continuity relating the oxygen concentration to its flux, $\partial_t C_{air}(\vec{x},t) + \vec{\nabla} \cdot \vec{J} = 0$. The oxygen flux on the diffusion side of the alveolar membrane may be identified as

$$\vec{J} = -D\vec{\nabla} C_{air}(\vec{x}),$$

and is commonly referred to as Fick's Second Law. Oxygen flux crossing the membrane is driven by the difference in oxygen concentration between its air and blood sides, i.e., $J = W(C_{air}(\vec{x}) - C_{\text{blood}})$. We assume the flux is continuous across the boundary, and as a consequence have

$$\vec{\nabla} C_{air}(\vec{x}) \cdot \hat{n}(\vec{x}) = \frac{W}{D} \left(C_{air}(\vec{x}) - C_{\text{blood}} \right), \tag{2.3.7}$$

where $\vec{x}$ is evaluated at the membranes, C_{blood} is the constant concentration on the blood side of the membrane, and D is the coefficient of diffusion of oxygen within the acinar gas. The coefficient of diffusion has units $[D] = L^2/T$, where L and T are arbitrary units of length and time, respectively.

We take the mean permeability of the alveolar membranes to oxygen, W, with units $[W] = L/T$, to be constant. As suggested from the unit analysis, we would expect a higher (lower) membrane permeability to lead to more (less) oxygen crossing the alveolar membranes within a given unit of time.

Equation 2.3.7 is intermediate between absorbing (Dirichlet) and reflecting (von Neumann) boundary conditions, hence the term "mixed." We may recover these two descriptions, either a perfectly reflecting membrane as in the von Neumann condition, or an absorbing membrane as in the Dirichlet condition, by considering the asymptotic limits of the parameter W. In the case $W \to 0$, we recover the perfectly reflecting membrane condition, while in the limit $W \to \infty$, we recover a description of the membranes as an oxygen sink.

The analogy between the diffusion-reaction of oxygen across the alveolar membranes and that of an electric potential field within an electrolytic solution is striking, and several authors have made progress in Laplacian transport across comlex interfaces, through the study of this connection.[19] Table 2.1 provides a comparison of other physical systems that are mathematically equivalent to the diffusion-reaction problem of oxygen within the acinar airways.

In the electrolytic cell, the current flux is driven by a difference in the electric potential of the electrodes. Similarly, a difference in oxygen concentration will drive the current flux, described by Fick's Law[10]. We seek to write the mixed boundary condition entirely in terms of the oxygen concentration difference. We must then investigate how the concen-

tration difference, $C(\vec{x})$, is related to the concentration on the bulk side of the membrane, $C_{air}(\vec{x})$.

Consider a source-receptor problem, in which oxygen molecules propagate from the source impact, and possibly react with a membrane boundary with arbitrarily complicated interfacial geometry. We will also take the oxygen concentration over the source to be constant, such that $C_{air}(\vec{x}) = C_{ent}$ for $\vec{x}$ at its entrance. The receptor, represented by the alveolar membranes, is also held at constant concentration on the blood side of the membrane and is expressed as C_{blood}. Equations 2.3.6 and 2.3.7 will now take the following form:

$$\begin{aligned}
&\vec{\nabla}^2 C_{air}(\vec{x}) = 0, \text{ for } \vec{x} \text{ in the bulk ,} \\
&C_{air}(\vec{x}) = C_{ent}, \text{ for } \vec{x} \text{ at the source,} \\
&\vec{\nabla} C_{air}(\vec{x}) \cdot \hat{n}(\vec{x}) = \frac{W}{D} \left(C_{air}(\vec{x}) - C_{\text{blood}} \right), \text{ for } \vec{x} \text{ at the membrane.}
\end{aligned}$$

We will take the oxygen concentration to have the following dependence on the parameters of the system [10]: $C_{air}(\vec{x}) = C_{air}(\vec{x}; C_{ent}, C_{\text{blood}}, D/W)$, and define the concentration difference between the bulk and blood sides of the membrane to be $C(\vec{x}) := C_{air}(\vec{x}; C_{ent}, C_{\text{blood}}, D/W) - C_{\text{blood}}$. The resulting equation of motion and mixed boundary condition is given by

$$\begin{aligned}
&\vec{\nabla}^2 C(\vec{x}) = 0, \text{ for } \vec{x} \text{ in the bulk ,} \\
&C(\vec{x}) = C_{ent} - C_{\text{blood}}, \text{ for } \vec{x} \text{ at the source,} \\
&\vec{\nabla} C(\vec{x}) \cdot \hat{n}(\vec{x}) = \frac{W}{D} C(\vec{x}), \text{ for } \vec{x} \text{ at the membrane.}
\end{aligned}$$

By inspection of $C(\vec{x})$ with $C_{air}(\vec{x})$, we have $C(\vec{x}) = C_{air}(\vec{x}; C_{ent} - C_{\text{blood}}, 0, D/W)$. Therefore, $C(\vec{x})$ is sufficient to describe the dynamics of the concentration distribution.

System	Flux	Equation of motion	Length scale
Electrochemical	$\vec{J} = -\rho^{-1}\vec{\nabla}V$	$\vec{\nabla}^2 V = 0$	$\Lambda = R/\rho$
Heat conduction	$\vec{J} = -K\vec{\nabla}T$	$\vec{\nabla}^2 T = 0$	$\Lambda = K/H$
Diffusion-reaction	$\vec{J} = -D\vec{\nabla}C$	$\vec{\nabla}^2 C = 0$	$\Lambda = D/W$

Table 2.1: Mathematically equivalent physical systems. ρ^{-1} = inverse electrolyte resistivity, K = thermal diffusivity, D = diffusion coefficient, R^{-1} = inverse surface resistance, H = surface conductance, and W = surface permeability.

Accordingly, we have[10],

$$\begin{aligned} C_{air}(\vec{x}; C_{ent}, C_{\text{blood}}, D/W) &= C_{air}(\vec{x}; C_{ent} - C_{\text{blood}}, 0, D/W) + C_{\text{blood}} \\ &= C(\vec{x}) + C_{\text{blood}}. \end{aligned} \tag{2.3.10a}$$

In conclusion, we have found that we may describe the oxygen dynamics of the system in terms of the concentration difference between the bulk and blood sides of the alveolar membranes. Equation 2.3.10a is the result of such an analysis, and we found that the concentration depended upon the parameter D/W, appearing within the equations of motion. Furthermore, we applied the results of Section 2.3.1 to the physical picture of oxygen diffusion within the human lung acinus to arrive at the relevant equations of motion for the system.

2.4 Recent advances in diffusion-reaction systems

2.4.1 Exploration length

The parameter D/W resides within the mathematical framework of the diffusion-reaction of oxygen across the alveolar membranes of the acinar airways in the human lung. Until recently its physical interpretation had largely remained a mystery. Pfeifer et al.[20, 13, 18] and Sapoval et al.[21] have recently suggested a new interpretation for this parameter, demonstrating its physical significance in the estimation of the effective surface area of alveolar membranes used in the transport of oxygen from the air to the blood. We outline their result as follows.

Consider a set with fractal dimension D_f embedded within a space of topological dimen-

sion two. Let Λ be the distance along the set that a diffusing particle travels in time τ, and let there exist an inner cut-off l below which $D_f = 1$ for $\Lambda < l$. Let $\sqrt{\langle x^2 \rangle} = \sqrt{D\tau^\alpha}$ be the root mean square distance this particle travels in time τ, and let us assume the diffusion is not anomalous; i.e. we take $\alpha = 1$. We consider diffusion near the set such that it is locally flat, and take the global permeability of the set to be W. If the particle concentration near the curve is $(D\tau)^{-1}$, and the particle flux across the curve is given by $J = W\Delta C$, then we have[10]

$$W = \frac{1}{\tau\Lambda\,(D\tau)^{-1}},$$

and it follows that

$$\Lambda = \frac{D}{W}. \tag{2.4.11}$$

We identify Λ as the distance along the interfacial set in which a typical particle travels before it crosses. Since the exploration length gives the length along a flat patch of the interface used in transport, its description may be extended to lengths $\Lambda > l$ by assuming that $\Lambda = Nl$ for some $N > 1$. In this way, the exploration length gives the length *along* the prefractal interface used in transport.

$\Lambda = D/W$ can be extended to cases of topological dimension three. Consider an interfacial surface with fractal dimension $2 \leq D_f \leq 3$, embedded within a space of topological dimension three. If one intersects a plane with a fractal set of dimension D_f embedded in a space of topological dimension three, then the dimension of the intersection is given by $D_f - 1$[1].

2.4.2 Diffusional screening and active zones in oxygen transport

In Section 2.4.1 we reviewed the development of exploration length, $\Lambda = D/W$, as a quantifiable measure of surface screening. We saw that if the permeability of the membranes is taken to be small, then the length along the membranes that the oxygen molecules explore before they usually cross becomes very large. Conversely, when W is taken to be very large, the exploration length becomes very small, and the oxygen molecules typically cross the

[1]The extension of the exploration length to topological dimension three relies on intersection theorems in measure theory. See, for example, ref. [22].

membranes on their first impact with its surface.

Sapoval et al.[14, 15], and Pfeifer et al.[13, 12] were able to extend Makarov's result to cases in which the interface satisfied a mixed boundary condition, intermediate between perfectly absorbing and reflecting. They identified this new length, Λ, as the exploration length appearing within the equations of motion for particles diffusing toward a partially absorbing boundary.

Since this discovery, numerical studies of surface screening have almost exclusively been the primary investigative tool used in the study of diffusional transport across an interface with mixed boundary condition. Fractal geometry has become a standard model of interfacial comlpexity because of its simple generating algorithms and complicated surface geometry. Surface sites participating in particle transport and measured by the exploration length have been called *active zones*[10].

2.5 Summary and conclusions

We have presented a review of several aspects of the gas exchange process within the human lung. We reviewed the structure and physiology of the acinar airways of the human lung and introduced a picture in which we emphasized those properties of the airways which are important in understanding oxygen transport from the air to the hemoglobin in the red blood cells.

We also reviewed the development of a mathematical representation of oxygen diffusion in terms of the Fokker-Plank equation. From this description we developed a mathematical model representing the diffusion of oxygen through the acinar airways and its reaction on the membrane surface to produce a blood side current.

We then reviewed several recent major developments in the mathematical treatment of oxygen diffusion throughout the acinar airways. We first reviewed the discovery of a new physical interpretation of the parameter $\Lambda = D/W$. We discussed the history of its discovery, and its interpretation as the length along the surface which an oxygen molecule explores before it usually crosses the surface. Its discovery suggested that only geometrical

considerations were needed to estimate the transmembrane oxygen current, and showed that diffusional screening is a critical mechanism regulating the transport of oxygen to the blood.

Chapter 3

Model of a single acinar branch

3.1 Introduction

In other treatments of the lung acinus[10, 1], the exploration length was considered to measure those portions of the alveolar membranes that exclusively participated in the transport of oxygen to the blood. Here, we observe that the details of the interfacial geometry are washed out by the exploration length in the measuremeant of the oxygen current transported across the alveolar membranes in the lung. Under the assumption that the details of the interfacial geometry are irrelevant to the transport of oxygen across it, we propose to model an acinar branch within the lung acinus as a cylinder with smooth walls.

The transport of oxygen across the alveolar membranes and the transport of oxygen across the surface of our model branch will be connected through the exploration length. In the model branch the exploration length, Λ, will be used to infer how much of its surface area is used in transport. For the acinar airways, we will use experimental data for the coefficient of diffusion for oxygen in the acinar gas D, and the permeability of the alveolar membranes W. The connection takes the form $\Lambda = D/W$. A prediction of this connection, is that our fully-branching model of the lung should reproduce behavior associated with the human lung under the assumption that the exploration length is the only parameter important to the screening of oxygen from the alveolar membranes.

In this chapter we begin the development of such a branching model of the human

lung by first developing a model of a single acinar duct. We will develop and explore the connection between two treatments of our proposed model branch, and we will identify the conditions under which they generate equivalent predictions of the oxygen current crossing its surface.

3.2 Laplace treatment of the single branch

The diffusion-reaction of oxygen through a cylinder with mixed boundary condition is exactly solved by taking advantage of its geometrical symmetry. We call such a treatment of the model branch the "Laplace treatment," and its solutions will serve as the model by which we compare other approximate methods we develop in the following sections. The Laplace treatment generates exact solutions for the cylinder, therefore other numerical approximations, such as the finite element method, will not be used for comparison.

Consider a cylinder with open ends $x = 0$ and $x = L$, where x is the axial coordinate of the cylinder. Let R and L be the radius and length of the cylinder, respectively. The steady state diffusion equation for the oxygen concentration is given by

$$\vec{\nabla}^2 C(\vec{x}) = 0. \tag{3.2.1}$$

Flux conservation at the interfacial boundary of the cylindrical surface gives

$$\vec{\nabla} C(\vec{x}) \cdot \hat{n}(\vec{x}) = \frac{C(\vec{x})}{\Lambda}, \tag{3.2.2}$$

where $\Lambda = D/W$; we take the surface normal to be directed radially inward toward the central axis. The following boundary conditions are imposed across the entrance and exit cross-sections of the cylinder:

$$C(r, \theta, 0) = C_{ent}(r), \tag{3.2.3a}$$

$$C(r, \theta, L) = C_{ext}(r). \tag{3.2.3b}$$

We assume these two expressions are well-behaved functions of r and allow for the con-

centration distributions within the branch to radially vary. Such expressions serve as test functions for the response of the oxygen current to radial density distributions in oxygen concentration.

Equations 3.2.1, and 3.2.2, along with their associated boundary conditions, form a closed system and can be solved[1] to give

$$C(r,x) = \sum_{i=1}^{\infty} 2\left(\frac{\delta_i}{R}\right)^2 \frac{J_0\left(\delta_i \frac{r}{R}\right)\left(f_i(R)\sinh\left(\delta_i \frac{L-x}{R}\right) + g_i(R)\sinh\left(\delta_i \frac{x}{R}\right)\right)}{\sinh\left(\delta_i \frac{L}{R}\right)\left(J_0(\delta_i)\right)^2\left(\delta_i^2 + \left(\frac{R}{\Lambda}\right)^2\right)}, \tag{3.2.4a}$$

$$f_i(R) := \int_0^R rC_{ent}(r)J_0\left(\delta_i \frac{r}{R}\right)dr, \tag{3.2.4b}$$

$$g_i(R) := \int_0^R rC_{ext}(r)J_0\left(\delta_i \frac{r}{R}\right)dr, \tag{3.2.4c}$$

where boundary conditions are given by Equation 3.2.3.

A notable case of Equation 3.2.4a arises when the boundary conditions are constant: $C(r,0) = C_{ent}$ and $C(r,L) = C_{ext}$. These may be used with the equation of motion, Equation 3.2.1, and its auxiliary equation, Equation 3.2.2, to give

$$C(r,x) = \sum_{i=1}^{\infty} \left(\frac{2R}{\Lambda}\right) \frac{J_0\left(\delta_i \frac{r}{R}\right)\left(C_{ent}\sinh(\delta_i \frac{L-x}{R}) + C_{ext}\sinh(\delta_i \frac{x}{R})\right)}{J_0(\delta_i)\sinh(\delta_i \frac{L}{R})\left(\delta_i^2 + \left(\frac{R}{\Lambda}\right)^2\right)}, \tag{3.2.5}$$

where δ_i are the ascending positive roots of

$$\delta_i J_1(\delta_i) - \frac{R}{\Lambda}J_0(\delta_i) = 0. \tag{3.2.6}$$

The intersections in Figure 3.1 give the roots of Equation 3.2.6. Since R/Λ multiplies $J_0(\delta_i)$ in Equation 3.2.6, the intersection of the functions depend upon R/Λ.

Two limits arise naturally from Equation 3.2.6: either $R/\Lambda \to 0$, in which case Equation 3.2.5 needs the roots of $J_1(\delta_i) = 0$, or $R/\Lambda \to \infty$, in which case Equation 3.2.5 needs the roots of $J_0(\delta_i)$. For large terms in the series the difference in these roots approaches $\pi/2$.[23]

Another natural choice of boundary conditions is given by the reflection of oxygen

[1] See appendix A for details.

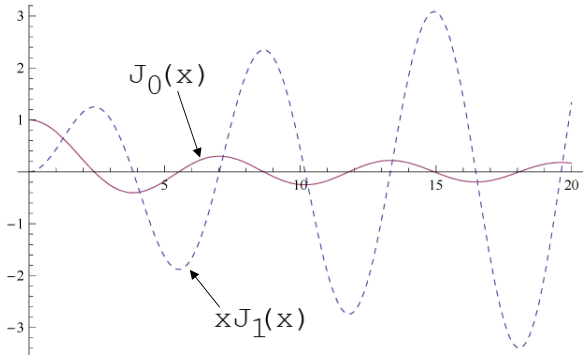

Figure 3.1: The intersections represent the roots of Equation 3.2.6. Here, $R/\Lambda = 1.0$.

molecules from the entrance and exit cross-sections of the cylinder. In this picture, oxygen molecules must leave the branch exclusively through its cylindrical surface. We take the reflecting boundary conditions to be

$$\partial_x C(x)|_{x=0} = 0, , \tag{3.2.7a}$$

$$\partial_x C(x)|_{x=L} = 0, \tag{3.2.7b}$$

$$C(r,x)|_{x=0} = C_{ent}(r). \tag{3.2.7c}$$

The solution for the oxygen concentration is given by

$$C(r,x) = \sum_{i=1}^{\infty} 2\left(\frac{\delta_i}{R}\right)^2 \frac{f_i(R) J_0(\delta_i \frac{r}{R}) \cosh\left(\delta_i \frac{L-x}{R}\right)}{(J_0(\delta_i))^2 \cosh\left(\delta_i \frac{L}{R}\right)\left(\delta_i^2 + \left(\frac{R}{\Lambda}\right)^2\right)}, \tag{3.2.8}$$

where the $f_i(R)$ are computed from Equation 3.2.4b. A special case of Equation 3.2.8 exists when $C_{ent}(r)$ is independent of r, and $f_i(R)$ may be integrated to give

$$C(r,x) = \sum_{i=1}^{\infty} 2C_{ent}\left(\frac{R}{\Lambda}\right) \frac{J_0(\delta_i \frac{r}{R}) \cosh\left(\delta_i \frac{L-x}{R}\right)}{J_0(\delta_i) \cosh\left(\delta_i \frac{L}{R}\right)\left(\delta_i^2 + \left(\frac{R}{\Lambda}\right)^2\right)}. \tag{3.2.9}$$

3.3 Helmholtz treatment of the single branch

In the previous section, the diffusion-reaction problem was solved exactly on the cylinder under several choices of boundary conditions. In this section we develop a new approximation of the diffusion-reaction problem from first principles, and we study its behavior in

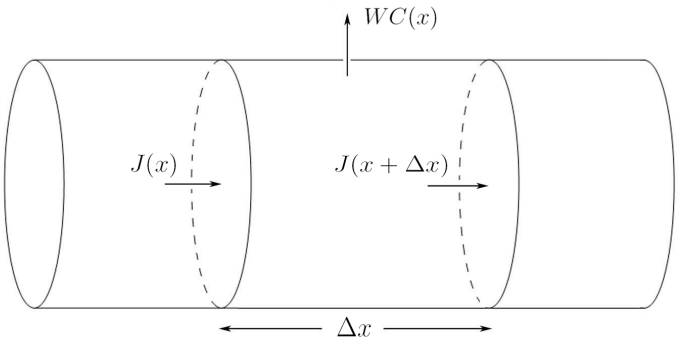

Figure 3.2: Model of a single acinar duct in the Helmholtz treatment of the cylinder.

relation to solutions computed from the Laplace treatment of the model branch.

If the oxygen flux is conserved across the cross-sections shown in Figure 3.2, we find

$$(J(x+\Delta x) - J(x))\,\pi R^2 = -WC(x)2\pi R\Delta x, \tag{3.3.10}$$

where the negative sign is an artifact of the assumption that the oxygen flux crosses the branch surface from the interior to its exterior. Under the assumption that J is a smooth, well-behaved function, we may apply Taylor's Theorem and find $J(x+\Delta x) = J(x) + J'(x)\Delta x + \mathcal{O}(\Delta x^2)$. Upon application to Equation 3.3.10, we find

$$J'(x) + \mathcal{O}(\Delta x) = -\frac{2W}{R}C(x).$$

We take the limit $\Delta x \to 0$ and apply Fick's Law, $\vec{J} = -D\vec{\nabla}C$, to find

$$\frac{d^2}{dx^2}C(x) - \lambda^2 C(x) = 0, \tag{3.3.11a}$$

$$\lambda^2 = \frac{2}{R\Lambda}. \tag{3.3.11b}$$

We note that diffusion entered the physical picture through the application of Fick's law.

We will now consider a branch where the boundary conditions on the entrance and exit

surfaces are fixed,

$$C(0) = C_{ent},$$
$$C(L) = C_{ext}.$$

The solution to Equation 3.2.1 under these boundary conditions is given by

$$C(x) = \frac{C_{ent}\sinh\left(\lambda(L-x)\right) + C_{ext}\sinh\left(\lambda x\right)}{\sinh\left(\lambda L\right)}. \tag{3.3.13}$$

The Laplace and Helmholtz treatments of the single branch are connected, in the sense that one is a limiting case of the other. We expect solutions for the current in the Laplace treatment of the branch to asymptotically converge on those solutions given in the Helmholtz treatment under equivalent boundary conditions. This is because we expect the radial dependence of the concentration to become less important as the branch radius vanishes. A relevant question to ask is, "how small must this radius be?"

We investigated this question by observing how the oxygen concentration in the Laplace treatment behaves as the quantity R/Λ vanishes. By starting with Equation 3.3.13, we found that

$$\begin{aligned} C(r,x) &= \sum_{i=1}^{\infty}\left(\frac{2R}{\Lambda}\right)\frac{J_0\left(\delta_i\frac{r}{R}\right)\left(C_{ent}\sinh(\delta_i\frac{L-x}{R}) + C_{ext}\sinh(\delta_i\frac{x}{R})\right)}{J_0(\delta_i)\sinh(\delta_i\frac{L}{R})\left(\delta_i^2 + \left(\frac{R}{\Lambda}\right)^2\right)} \\ &= \left(\frac{2R}{\Lambda}\right)\frac{J_0\left(\delta_1\frac{r}{R}\right)\left(C_{ent}\sinh(\delta_1\frac{L-x}{R}) + C_{ext}\sinh(\delta_1\frac{x}{R})\right)}{J_0(\delta_1)\sinh(\delta_1\frac{L}{R})\left(\delta_1^2 + \left(\frac{R}{\Lambda}\right)^2\right)} \\ &\quad + \sum_{i=2}^{\infty}\left(\frac{2R}{\Lambda}\right)\frac{J_0\left(\delta_i\frac{r}{R}\right)\left(C_{ent}\sinh(\delta_i\frac{L-x}{R}) + C_{ext}\sinh(\delta_i\frac{x}{R})\right)}{J_0(\delta_i)\sinh(\delta_i\frac{L}{R})\left(\delta_i^2 + \left(\frac{R}{\Lambda}\right)^2\right)} \\ &\sim \frac{C_{ent}\left(\sinh\left(\lambda(L-x)\right)\right) + C_{ext}\sinh\left(\lambda x\right)}{\sinh\left(\lambda L\right)}, \end{aligned} \tag{3.3.14}$$

where

$$\delta_1 = \sqrt{\frac{2R}{\Lambda}}\left(1 - \frac{R}{8\Lambda} + \frac{3}{64}\left(\frac{R}{\Lambda}\right)^2 + \dots\right)$$
$$\approx \sqrt{\frac{2R}{\Lambda}}. \tag{3.3.15a}$$

We identify the radius of convergence for Equation 3.3.15a as

$$R/\Lambda < 1. \tag{3.3.16}$$

This expression provides a quantitative measure of the validity of solutions within the Helmholtz treatment of the model branch.

The concentration in the Helmholtz treatment for reflecting boundary conditions, Equations 3.2.7a and 3.2.7b, is given by

$$C(x) = C_{ent}\frac{\cosh\left(\lambda(L-x)\right)}{\cosh\left(\lambda L\right)}. \tag{3.3.17}$$

Reflecting boundary conditions play a powerful role in the study of surface screening in the single branch because the oxygen molecules leave exclusively through the surface.

3.4 Oxygen current across the branch surface

In this section we compute the current crossing the surface of the branch, given that we have the solution for its concentration. We focus on two regimes of interaction between the diffusing molecules and the cylindrical boundary they are driven to cross. Given the observation that the mixed boundary condition contains both a property of the boundary surface, W, and the diffusion space, D, we expect that the oxygen current will be limited by these parameters.

We will investigate the diffusion-limited and reaction-limited oxygen currents, and give expressions for their calculation from the oxygen concentrations. We will demonstrate that the current follows a simple relationship linear in the concentration difference across the

surface of the branch, analogous to Ohm's Law from electrodynamics.

3.4.1 Diffusion-limited oxygen current

In the diffusion-limited case, the permeability of the cylindrical surface is taken to be very large, such that the exploration length nearly vanishes, $\Lambda = D/W \to 0$. Since the exploration length is very small, molecules interact with those subsets of the membranes that they first impact. Therefore, we define the diffusion-limited current to be that current produced by the cylindrical boundary in the limit $\Lambda \to 0$. More loosely, we may refer to any case of the oxygen current in which the exploration length is sufficiently small, to be the diffusion-limited current.

The oxygen current on the airway side of the branch surface may be computed directly through integration of its oxygen flux,

$$I = \int \vec{J} \cdot \hat{n} dS. \tag{3.4.18}$$

The diffusional flux is given by Fick's Law, $\vec{J} = -D\vec{\nabla}C$, and we have

$$I = D \int_{\partial\Omega} \vec{\nabla}C(\vec{x}) \cdot \hat{n}(\vec{x}) dS. \tag{3.4.19}$$

3.4.2 Reaction-limited oxygen current

Current is reaction-limited when molecules do not immediately cross the cylindrical boundary representing the alveolar membranes, but instead reflect and explore a distance along the surface equivalent to the exploration length. The probability that any single impact of a diffusing molecule resulting in the molecule crossing the membrane is related to the membrane permeability, in the sense that a lower (higher) permeability will decrease (increase) the probability of crossing the surface. This suggests that we define the reaction-limited current to be that current which is produced in the limit $\Lambda \to \infty$.

According to an argument proposed by Hou [10], we note that the mixed boundary condition will transition asymptotically to a Neumann-type boundary condition, $\vec{\nabla}C(\vec{x}) \cdot \hat{n} =$

0, in the limit $\Lambda \to \infty$. Therefore $C(\vec{x}) = C_{ent} - C_{\text{blood}}$ will solve the equation of motion, and the molecules almost always reflect from the surface, such that the concentration within the cylinder will become essentially uniform. Therefore, the concentration at every point on the surface of the membrane becomes a constant $C_{ent} - C_{\text{blood}}$.

To compute the current in the reaction-limited regime ($W \to 0$), we use Equation 3.4.18 with the concentration difference given by $C_{ent} - C_{\text{blood}}$:

$$\begin{aligned} I &= W \int_{\partial\Omega} dS C(\vec{x}) \\ &= W S_{branch}(C_{ent} - C_{\text{blood}}), \end{aligned} \tag{3.4.20a}$$

where S_{branch} is the total surface area of the model branch. In the more general case where the equation of motion is satisfied by $C(\vec{x}) = C_{air}(\vec{x}) - C_{\text{blood}}$, Equation 3.4.20a may be used to compute the current generated by the surface, and we will write the concentration $C(\vec{x})$, as [10]:

$$\begin{aligned} C(\vec{x}) &= C_{air}(\vec{x}, C_{ent} - C_{\text{blood}}, 0, D/W) - C_{\text{blood}} \\ &= C_{ent} - C_{\text{blood}} \frac{C_{air}(\vec{x}, C_{ent} - C_{\text{blood}}, 0, D/W) - C_{\text{blood}}}{C_{ent} - C_{\text{blood}}} \\ &= (C_{ent} - C_{\text{blood}}) \tilde{C}(\vec{x}; D/W), \end{aligned}$$

with

$$\tilde{C}(\vec{x}; D/W) := \frac{C_{air}(\vec{x}, C_{ent} - C_{\text{blood}}, 0, D/W) - C_{\text{blood}}}{C_{ent} - C_{\text{blood}}}.$$

We will use this to compute the reaction-controlled current ($W \to 0$) by means of Equation 3.4.20a:

$$I(D/W) = W \underbrace{\int_{\partial\Omega} dS \tilde{C}(\vec{x}; D/W)}_{S_{eff}(D/W)} (C_{ent} - C_{\text{blood}}), \tag{3.4.22}$$

where the effective surface area has functional dependence, $S_{eff}(D/W)$. The current may

then be expressed as

$$I(D/W) = WS_{eff}(D/W)(C_{ent} - C_{\text{blood}}), \tag{3.4.23}$$

where W is the permeability and

$$S_{eff}(D/W) := \int_{\partial\Omega} dS\tilde{C}(\vec{x}; D/W) \tag{3.4.24}$$

is the effective surface area of the branch surface used in transport. Remarkably, the functional form of Equation 3.4.23 holds for all values of $\Lambda = D/W$ [10], and it implies that the concentration difference *across the surface* drives the oxygen current. In other words, the concentration difference is to be taken directly across the surface for *any* solution of the oxygen current that can be expressed as linear in the concentration difference. Due to this interpretation for the concentration difference, we interpret the function S_{eff} as the amount of surface area used directly for transport.[10, 1]

In the electrodynamic picture, such a linear dependence upon the oxygen concentration is analogous to the electric potential difference across an interface drives the electron current. To take further advantage of this analogy, we note taht the conductance alveolar membranes is given by $WS_{eff}(D/W)$.

To explore how surface screening affects the transport properties of the current generated by the model branch, we computed the current using Equation 3.4.19. An advantage in the study of a branch with reflecting boundary conditions is that the current is globally restricted to leave only through its surface, and not through the end cross sections.

The current given by the Laplace treatment may be calculated through an application of Equation 3.2.9 to Equation 3.4.19:

$$I(\Lambda) = \frac{4\pi R^3 DC_{ent}}{\Lambda^2} \sum_{i=1}^{\infty} \frac{\tanh\left(\delta_i \frac{L}{R}\right)}{\delta_i \left(\delta_i^2 + \left(\frac{R}{\Lambda}\right)^2\right)}. \tag{3.4.25}$$

Alternatively, the oxygen current produced within the Helmholtz treatment of the model

branch may be found though an application of Equation 3.3.17 to Equation 3.4.19:

$$I(\Lambda) = \pi DC_{ent}\left(\frac{2R^3}{\Lambda}\right)^{1/2}\tanh(\lambda L). \tag{3.4.26}$$

Through a side-by-side inspection of Equations 3.4.25 and 3.4.26, we can see clear functional similarities. In the same way Equation 3.3.13 was shown to coincide with Equation 3.2.5 when $R/\Lambda < 1$, Equation 3.4.26 will also coincide with Equation 3.4.25. Thus, we find that

$$\begin{aligned} I &= \frac{4\pi R^3 DC_{ent}}{\Lambda^2}\sum_{i=1}^{\infty}\frac{\tanh\left(\delta_i\frac{L}{R}\right)}{\delta_i\left(\delta_i^2+\left(\frac{R}{\Lambda}\right)^2\right)} \\ &= \frac{4\pi R^3 DC_{ent}}{\Lambda^2}\frac{\tanh\left(\delta_1\frac{L}{R}\right)}{\delta_1\left(\delta_1^2+\left(\frac{R}{\Lambda}\right)^2\right)} + \mathcal{O}(R^2) \\ &\sim \pi DC_{ent}\left(\frac{2R^3}{\Lambda}\right)^{1/2}\tanh(\lambda L), \end{aligned}$$

where $\delta_1 \approx \sqrt{\frac{2R}{\Lambda}}$ when $R/\Lambda < 1$.

3.5 Results

Interestingly, Equation 3.3.16 is not dependent upon the length of the cylinder. This is surprising because cylinders of several different aspect ratios may satisfy the same convergence radius and may define an equivalence class of branch structures. Such a result may lead to counter-intuitive situations such as the existence of a solution in which a disc may yield good approximation to those of the Laplace treatment. Therefore, the width of a branch alone may not provide a unique measure of validity for the model, and we need to also determine the transport parameters of the system. In this way, the transport and structural parameters of the tree are strongly coupled. This connection may be deeply rooted in the operation of biological structures, such as the acinar airways, and may emerge from restrictions generated by evolutionary pressures on an organism.

Another important result of our analysis is that one may write the oxygen current crossing the surface of the model branch as a linear function of the oxygen concentration

difference across its surface. As suggested through our analysis, if the oxygen current may be put into a form linear in the concentration difference, then that concentration difference may be interpreted as being taken across the interface itself. It is somewhat of a miracle that Ohm's Law holds at all, because a charged particle within a potential difference will be accelerated. Ohm's Law loosely states that the speed of the particle is proportional to the potential difference, and it is equally remarkable that the oxygen current depends only linearly on the concentration difference across the alveolar membranes.

Figures 3.3 through 3.6 show several concentration and current profiles computed with solutions from the Laplace treatment of the model branch. These solutions were computed such that the truncated contributions to the current were less than 1% with respect to that of the nontruncated solution. The identification of the truncation term was made by first decomposing the series into negligable and non-neglibable portions, and then defining the relative error for the those contributions. The contributions were then approximated using the Euler-Maclaurin approximation of a series in terms of an integral, and the relevant integration was performed. The result gave a bound on the appropriate term in the series for a given relative error:

$$i > \frac{2}{\pi^2 \epsilon} \cdot \frac{R}{\Lambda}, \tag{3.5.27}$$

where ϵ is the fixed relative error of the truncated terms (for example, $\epsilon = 0.01$), R is the radius of the branch, and $\Lambda = D/W$ is the exploration length for the oxygen molecules in the branch.

Equation 3.5.27 reflects the expectation that the demand for a smaller relative error in the series will imply taking a larger value for the truncation term i. Remarkably, the radius and transport parameters enter into the choice of truncation term by virtue of the term R/Λ. A result of Equation 3.5.27 is that for fixed ϵ, one must choose $R/\Lambda = \pi^2\epsilon/2$ so that $i = 1$. In such a case, the leading order term will completely describe the concentration computed within the Laplace treatment.

Approaching Equation 3.5.27 with the goal of choosing ϵ, we find that in order to have $i = 1$, ϵ must satisfy $\epsilon \geq 0.203 R/\Lambda$. This implies that in order to gain better approximation of solutions from the Laplace treatment, R/Λ must become increasingly smaller and further

from 1. Similar conclusions were also reached in the analysis leading to Equation 3.3.16.

Figure 3.3 depicts several concentration profiles with differing choices for the exploration length Λ. As expected, we find that a larger choice for exploration length decreases the concentration difference across the branch surface (reflected in the fact that we have chosen to evaluate the concentration at $r = R = 0.1$).

In Figure 3.4 we study the radial sensitivity of the concentration within the branch, and we find that the sensitivity is greatest for small values of the transport parameters ($\Lambda = D/W = 0.1$). We conclude that the radial variation in the concentration is essentially uniform for large values (in this example, $\Lambda = 10$) of the exploration length.

In Figure 3.5 we study the relationship between concentrations derived from the Laplace and Helmholtz treatments of the branch. Here we studied how the concentration in the Helmholtz treatment compares with the radial variations of those computed from the Laplace treatment. As expected, the concentration from the Helmholtz treatment is always smaller than that of the Laplace treatment for concentration, evaluated at the axis. Interestingly, the Helmholtz treatment concentration is larger than the Laplace treatment concentration evaluated at the radius, near the entrance of the branch, but then becomes smaller than this concentration near the end of the branch. This transition occurs very quickly, with the concentration in the Helmholtz treatment yielding an overestimate near the entrance and an underestimate near the end of the branch.

In Figure 3.6 we present current profiles for reflecting boundary conditions computed in both the Laplace and Helmholtz treatments of the branch. We find good agreement between the treatments from the entrance of the branch until approximately $\Lambda \approx 0.1 = R$. From this observation, we conclude that a significant deviation from that of the Laplace treatment occurs when $R/\Lambda \approx 1$. This is in good agreement with the predictions of both Equation 3.3.16 and Equation 3.5.27.

3.6 Summary and Conclusions

In this chapter we have proposed a model of an acinar branch motivated by a new interpretation of the transport parameter, Λ, appearing within the mathematical description of the diffusion-reaction process within the acinar airways of the human lung. Solutions for the oxygen current and concentration within the model branch are exactly solvable in the standard formulation of the diffusion-reaction problem, leading to a treatment that we call the "Laplace treatment" of the branch. A reformulation of the diffusion-reaction equations of motion was proposed within the context of our model geometry, resulting in a Helmholtz-style equation of motion. We described the resulting treatment of the model in this picture as the "Helmholtz treatment" of the branch.

Interestingly, the diffusion and reaction equations are separate expressions in the Laplace treatment, while the diffusion-reaction of oxygen molecules in the Helmholtz treatment is naturally described through one equation. Clearly such a union of the diffusion and reaction terms in the Helmholtz treatment is a result of the loss in radial variation in oxygen concentration; however, it is far from clear how the equations of motion dynamically transform between these treatments as $R \to 0$.

We conclude that solutions derived from the Laplace treatment for the model branch, are sufficiently approximated by those from the Helmholtz treatment under the restriction $R/\Lambda < 1$. This is a remarkable result for two reasons. First, it connects, in a quantitative and surprisingly way, the structure of the model branch and the transport parameters associated with the diffusion of oxygen in the acinus of the human lung. Second, it provides bounds on the validity of the Helmholtz treatment as an approximation for the diffusion-reaction dynamics of oxygen within the model branch. We conclude that knowledge of only the width of the branch is insufficient to predict whether approximations for the concentration and current made by the Helmholtz treatment are valid.

We presented an analysis first conducted by Hou in his PhD thesis[10] resulting in the description of the current crossing the surface of the branch as a function of $\Lambda = D/W$. We also found the current to be linear in the concentration difference across the surface of the branch, $I = WS_{eff}\,(C_{ent} - C_{blood})$, and noted its analogy with Ohm's Law from

electrodynamics. $S_{eff}(D/W)$ was interpreted as the effective surface area used in transport of oxygen molecules from the interior of the branch to its exterior, and it represents those portions of the surface that are accessed by diffusing oxygen molecules. We concluded that surface screening may be quantified through the calculation of $S_{eff}(D/W)$, and due to its appearance in the oxygen current, it plays a critical role in the transport of that current to the exterior of the branch.

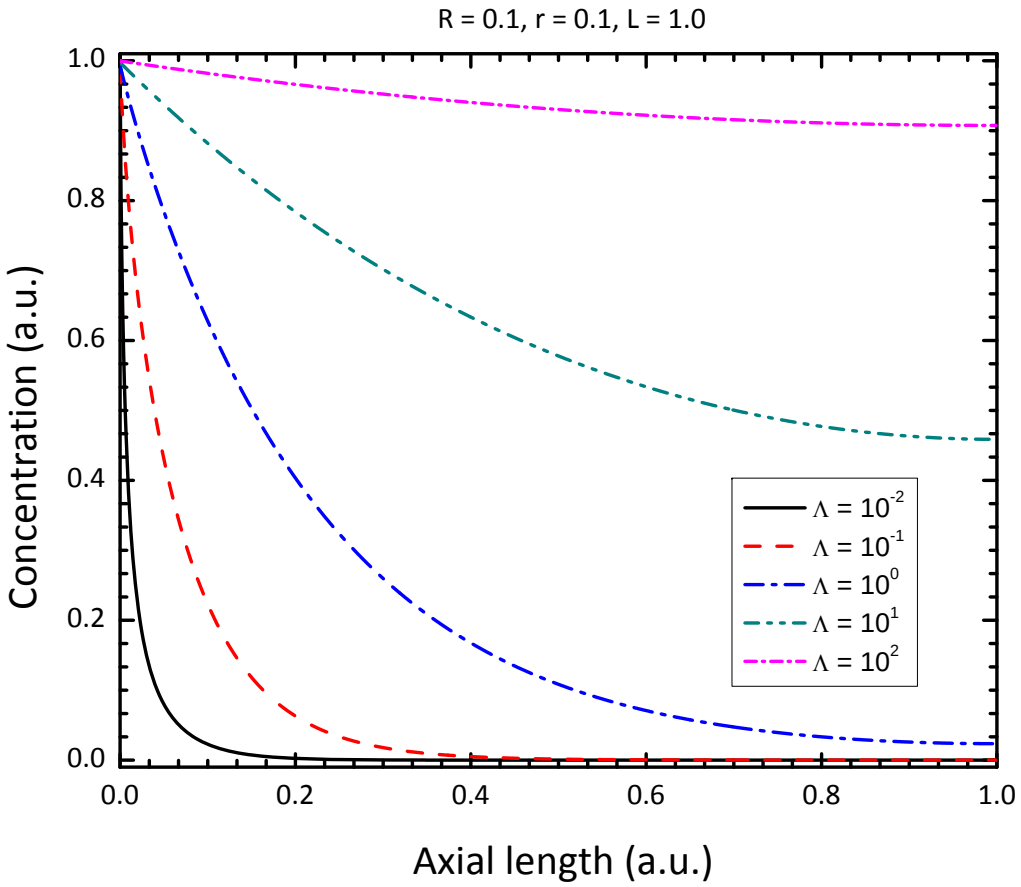

Figure 3.3: Concentration profiles with reflecting boundary conditions in the Laplace treatment of the model branch, for several choices of the screening parameter Λ. The series solution for the concentration in the Laplace treatment was truncated such that the relative error is within 1% of the full solution.

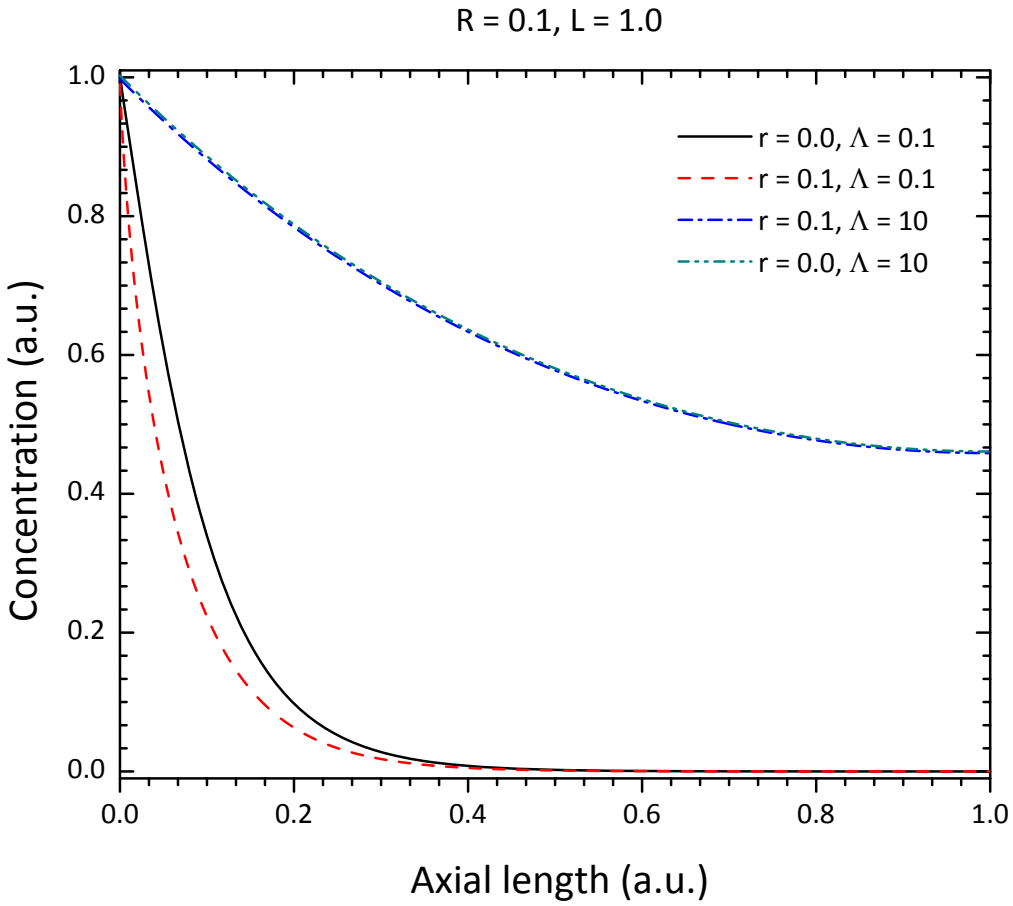

Figure 3.4: Concentration profiles with reflecting boundary conditions in the Laplace treatment with several choices for both r and Λ, demonstrating the radial dependence of the concentration under various screening regimes. The relative error in the truncation of the Laplace treatment solution for the concentration is to within 1%.

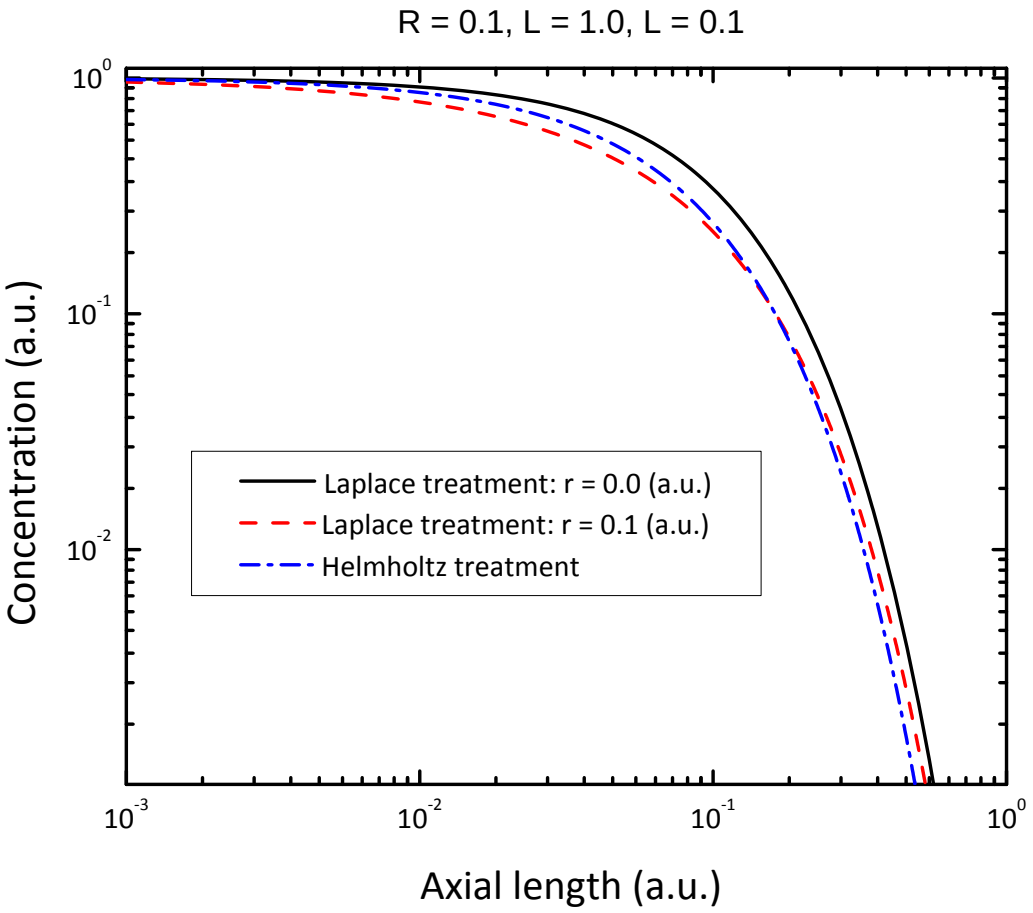

Figure 3.5: Log-Log plot of the concentration in both treatments of the model branch. Concentrations in the Laplace treatment were truncated such that they are within 1% of the solution using the full series.

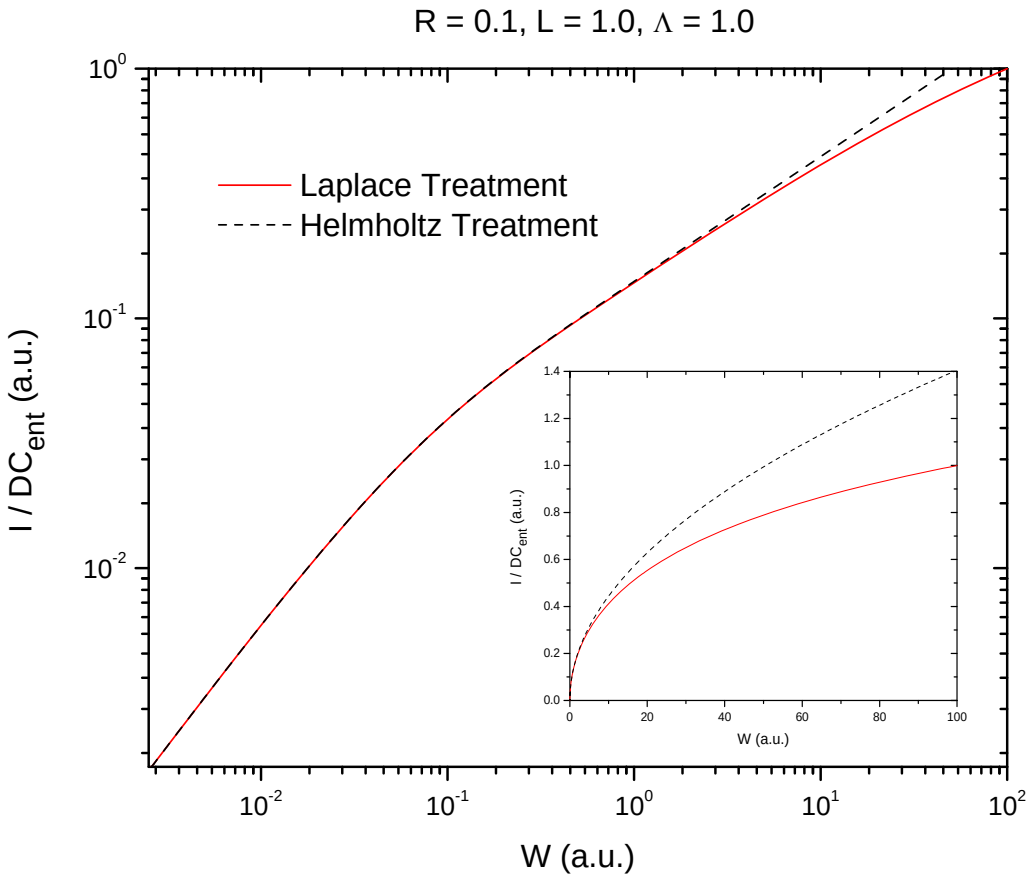

Figure 3.6: Currents crossing the surface of a model branch with reflecting boundary conditions on logarithmic and linear (inset) scale. Currents computed in the Laplace treatment of the branch have relative error to within 1% of the full solution.

Chapter 4

Hierarchical model of gas exchange

4.1 Introduction

We will quantify oxygen transport through the acinar airways by representing the airways as a branching graph. The edges of the graph will represent acinar branches, and will be associated with a model of an acinar branch we presented in chapter 3. We consider the $(m+1)$-Cayley tree to be a graph, with m daughter edges extending from each terminal vertex of a parent edge, as outlined in Figure 4.1. Figure 4.2 was constructed by appending a generator to each daughter edge, and this process can be repeated, in order to produce a tree of arbitrary depth, n. The entrance and terminal nodes of the tree are the only exceptions, as these nodes connect to only one edge within the tree.

The branching generation will be defined as the class of nodes equidistant from the $k = 0$ node along any path in the graph. We will label the nodes by $k = 1, 2, \ldots, n$, where n is the depth of the tree. The length and width of the branches will be labled by $k + 1$, with the single exception of the entrace branch described by $k = 1$.

4.2 Tree model of lung architecture

We will develop a branch by branch model of the acinar airways in which oxygen molecules propagate by diffusion and where branches are coupled with each other through the nodes of the graph. We use the $(m+1)$-Cayley tree as the skeletal structure of the model, and in

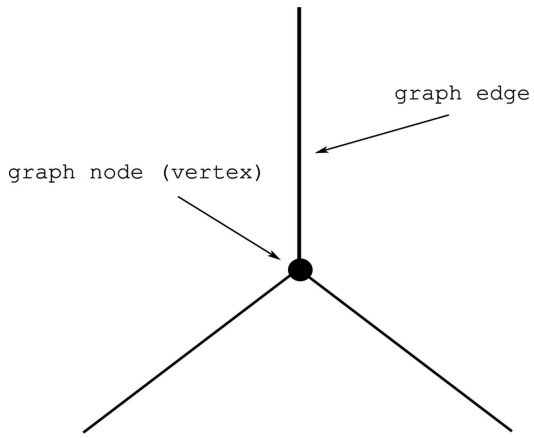

Figure 4.1: Fundamental unit of the 3-Cayley tree.

this chapter, we will assume that each branch in the tree is equivalent to every other branch in width and length. In other words, if $2R_{k+1}$ and L_{k+1} are the width and length of the $k+1$ branch respectively, then we take $L_i = L$ and $R_i = R$ for all $i = 1, 2, \ldots, n+1$.

We will construct the model by using the cylinder geometry of the model branch which we developed within chapter 3, and as such, we will consider $\vec{\nabla}^2 C(\vec{x}) = 0$ as the equation of motion for oxygen within each individual branch. On the boundary of the tubes, we have $\vec{\nabla} C(\vec{x}) \cdot \hat{n} = C(\vec{x})/\Lambda$. Instead of using these expressions to model a single branch within the tree, we will model each branch using the Helmholtz treatment of the branch (Equation 3.3.11a):

$$\frac{d^2}{dx^2} C(x) - \lambda^2 C(x) = 0,$$

where $\lambda^2 = 2/R\Lambda$.

4.2.1 Structure of the tree

The Cayley tree of our model is composed of three classes of branches, and each class is defined through its respective boundary conditions. We will outline these classes as follows:

1. **Entrance branch**. There is only one such tube which serves as the entrance to the tree. (a), gives the constant concentration over the entrance cross-section, and (b) describes the current leaving the end of the tube:

   (a) $C(x)|_{x=0} = C_{ent}$,

(b) $\partial_x C(x)|_{x=L} = -I_{ext}/DS_0$.

These boundary conditions together with Equation 3.3.11a give:

$$C(x) = \frac{\lambda DS_0 \cosh(\lambda(L-x))C_{ent} - \sinh(\lambda x)I_{ext}}{\lambda DS_0 \cosh(\lambda L)}. \tag{4.2.1}$$

2. **Intermediate branches**. The intermediate branches of the Cayley tree are classified by (a), the current entering the branch and (b), the current leaving the branch. We have:

   (a) $\partial_x C(x)|_{x=0} = -I_{ent}/DS_0$,

   (b) $\partial_x C(x)|_{x=L} = -I_{ext}/DS_0$.

   These boundary conditions give the solution as:

$$C(x) = \frac{\cosh(\lambda(L-x))I_{ent} - \cosh(\lambda x)I_{ext}}{\lambda DS_0 \sinh(\lambda L)}. \tag{4.2.2}$$

3. **Terminal branches**. In the terminal branches, we will assume that: (a) the current entering the branch is known, and (b) alveoli populate the terminal cross-sections:

   (a) $\partial_x C(x)|_{x=0} = -I_{ent}/DS_0$,

   (b) $C(x)|_{x=L} = I_{ext}/WS_0$.

   The solution is given by:

$$C(x) = \frac{\sinh(\lambda(L-x))I_{ent} + \lambda\Lambda \cosh(\lambda x)I_{ext}}{\lambda DS_0 \cosh(\lambda L)}. \tag{4.2.3}$$

In all of the above expressions the cross-sectional area of the branches is $S_0 = \pi R^2$.

4.2.2 Solution for the oxygen current

To obtain an expression for the current crossing the surface of the branches, we will follow the following procedure:

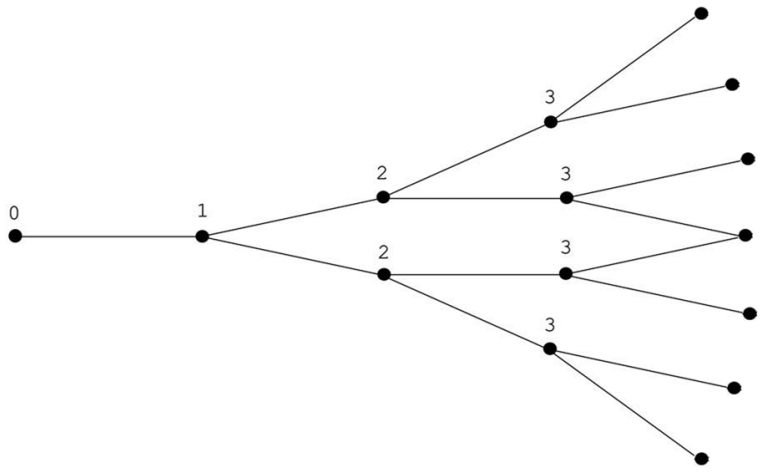

Figure 4.2: A 3-Cayley tree with $n = 3$.

1. We begin at a terminal node and solve for the entrance current $I_{ent}(C_{ent})$. This brings us to the $k = n$ node.

2. Using conservation laws[1] at the $k = n$ node, we find $I_{ext}(C_{ext})$ for the n^{th} intermediate tube.

3. Using the equation of motion for the intermediate tubes, Equation 4.2.2, we solve for $I_{ent}(C_{ent})$.

4. We continue this iterative process until we arrive at I_{ext} for the entrance tube. There, we use Equation 4.2.1 to solve for $I_{ent}(C_{ent})$, which provide the oxygen current that enters the tree. It is not immediately obvious that the oxygen current leaving the Cayley tree through the surface area of the branches, is equivalent to the oxygen current that enters the tree through its entrance branch. To address this, we suggest that the current entering the tree is equal to the current, leaving the tree in the steady state approximation:

$$I_{membrane} = \underbrace{I_{ent}^{tree} - I_{ext}^{tree}}_{\text{cylindrical side-walls}} + \underbrace{I_{ext}^{tree}}_{\text{tree end-caps}} . \tag{4.2.4}$$

[1]See Equation 2.2.6

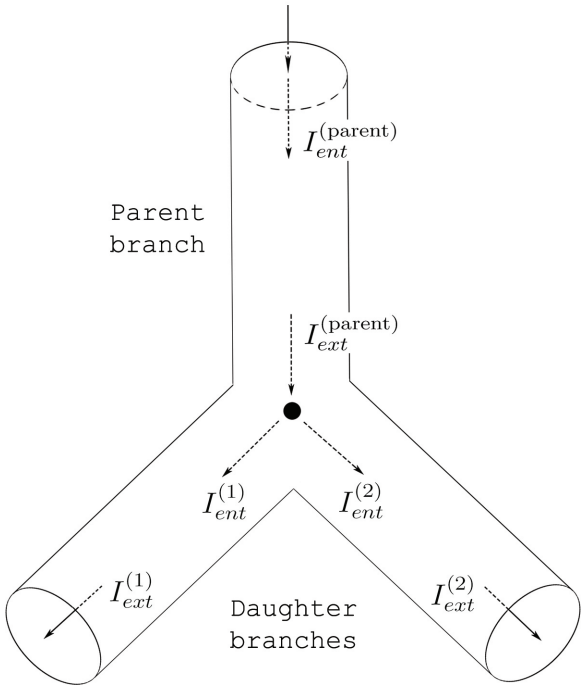

Figure 4.3: Branching within the intermediate tubes of the tree.

The current attenuated by the surface of the tree is given by[2]:

$$I(\Lambda) = \frac{D\pi R^2 C_{ent}}{m\tilde{f}^{n+1}(\Lambda)} \tag{4.2.5a}$$

$$\tilde{f}(\Lambda) := \frac{\lambda\Lambda + \tanh(\lambda L)}{m\lambda^2 \tanh(\lambda L)\Lambda + m\lambda}, \tag{4.2.5b}$$

where $\lambda = \sqrt{2/R\Lambda}$. $\tilde{f}^{n+1}(\Lambda) = \underbrace{\tilde{f} \circ \tilde{f} \circ \cdots \circ \tilde{f}}_{n+1 \text{ times}}(\Lambda)$, and $\circ$ denotes function composition. We should note that the function composition of $\tilde{f}$ operates only on the Λ explicit within Equation 4.2.5b, and not on the one implicit within λ.

Remark 4.2.1. We conducted a calculation for a tree with $n = 2$ and $m = 2$ in which the oxygen current leaving a branch was calculated by integrating the oxygen concentration along the branch's surface. We found the total current crossing the surface of the tree by summing the individual currents crossing the surface of each branch. We then compared this result to that predicted by Equation 4.2.5, and found exact agreement. We conjecture

[2]See appendix B.

that such a result will hold for a tree of arbitrary n, and conclude that Equation 4.2.4 provides the total current crossing the surface of a Cayley tree of depth n.

4.2.3 Möbius representation of the oxygen current

We may apply a class of transformations to $\tilde{f}$ that vastly simplify the evaluation of Equation 4.2.5. These are the Möbius transforms, and we apply such a transform in this section.

The remarkable idea behind the Möbius transform is to define a map under which the composition of $\tilde{f}$ is equivalent to the multiplication of 2 by 2 matrices. We will call such matrices "Möbius matrices." A Möbius matrix is a rotation of the Riemann sphere under stereographic projection of its surface onto the complex plane. Thus, we may relate orbits of $\tilde{f}$, that live in the complex plane, to rotations of the Riemann sphere, of which the Möbius matrices describe.

To begin, we write $\tilde{f}$ as:

$$\tilde{f}(\Lambda) = \frac{f_{11}\Lambda + f_{12}}{f_{21}\Lambda + f_{22}}, \tag{4.2.6}$$

and we note that its elements are given by Equation 4.2.5b: $f_{11} = \lambda$, $f_{12} = \tanh(\lambda L)$, $f_{21} = m\lambda^2 \tanh(\lambda L)$, and $f_{22} = m\lambda$. Composing $\tilde{f}$ with itself, we find:

$$\tilde{f} \circ \tilde{f}(\Lambda) = \frac{\left(f_{11}^2 + f_{12}f_{21}\right)\Lambda + f_{11}f_{12} + f_{12}f_{22}}{\left(f_{21}f_{11} + f_{22}f_{21}\right)\Lambda + f_{21}f_{12} + f_{22}^2}. \tag{4.2.7}$$

We now define the following matrix:

$$F_{ij} := \begin{pmatrix} \lambda & \tanh(\lambda L) \\ m\lambda^2 \tanh(\lambda L) & m\lambda \end{pmatrix} = \begin{pmatrix} f_{11} & f_{12} \\ f_{21} & f_{22} \end{pmatrix}, \tag{4.2.8}$$

where $i, j = 1, 2$. Multiplying this matrix by itself gives

$${F^2}_{ij} = F_{ik}F_{kj} = \begin{pmatrix} f_{11}^2 + f_{12}f_{21} & f_{11}f_{12} + f_{12}f_{22} \\ f_{21}f_{11} + f_{22}f_{21} & f_{21}f_{12} + f_{22}^2 \end{pmatrix}. \tag{4.2.9}$$

Notice that we may almost reproduce Equation 4.2.7 from the elements of Equation

4.2.9:

$$F_{ik}F_{kj}\cdot\begin{pmatrix} D \\ W \end{pmatrix} = W\begin{pmatrix} \left(f_{11}^2 + f_{12}f_{21}\right)\Lambda + f_{11}f_{12} + f_{12}f_{22} \\ \left(f_{21}f_{11} + f_{22}f_{21}\right)\Lambda + f_{21}f_{12} + f_{22}^2 \end{pmatrix}$$

$$= W\left(\left(f_{21}f_{11} + f_{22}f_{21}\right)\Lambda + f_{21}f_{12} + f_{22}^2\right)\begin{pmatrix} \tilde{f}\circ\tilde{f}(\Lambda) \\ 1 \end{pmatrix}. \qquad (4.2.10a)$$

All we need to do is divide the elements of the column vector resulting from Equation 4.2.10a to recover Equation 4.2.7. We have demonstrated that we may use a matrix, the Möbius matrix, as a calculational tool to compute $\tilde{f}^2(\Lambda)$. This approach can be generalized to

$$\tilde{f}^{n+1}(\Lambda) = \frac{D_{eff}}{W_{eff}}, \qquad (4.2.11)$$

where D_{eff} and W_{eff} can be computed by:

$$F^{n+1}\cdot\begin{pmatrix} D \\ W \end{pmatrix} = \begin{pmatrix} D_{eff} \\ W_{eff} \end{pmatrix}. \qquad (4.2.12)$$

The oxygen current can then be written in a compact form for arbitrary $n \geq 0$:

$$I = \frac{\pi R^2 DC_{ent}}{m}\cdot\frac{W_{eff}}{D_{eff}}. \qquad (4.2.13)$$

Remark 4.2.2. An analysis of the units for Equation 4.2.8 reveals that all elements within the matrix do not possess the same units. This appears to be a manifestation of the separation of Λ from within $\tilde{f}(\Lambda)$. The Möbius description of $\tilde{f}(\Lambda)$ is mathematically self-consistent, and therefore we consider the Möbius matrix technique as an intermediate calculational tool in the evaluation of $\tilde{f}(\Lambda)$.

4.2.4 Analytic form for the oxygen current

Equation 4.2.11 represents a powerful technique for reducing the effort of evaluating $\tilde{f}^{n+1}(\Lambda)$. Because we have a well-defined mapping between the composition of $\tilde{f}$ and the multipli-

cation of Möbius matrices, we can write the result of $\tilde{f}^{n+1}(\Lambda)$ in a remarkably analytic form.

Given that

$$I(\Lambda) = \frac{\pi R^2 D}{m\tilde{f}^{n+1}(\Lambda)} C_{ent}, \tag{4.2.14}$$

a tedious calculation[3] reduces Equation 4.2.11 to:

$$\tilde{f}^{n+1}(\Lambda) = \frac{D_{eff}}{W_{eff}} \frac{\frac{\sinh(\lambda L)}{\lambda} + \frac{\Lambda}{2}\left((-m+1)\cosh(\lambda L) + \sqrt{\cdot}\right) + \frac{\Lambda\sqrt{\cdot}}{\left(\frac{1}{4m}\left((m+1)\cosh(\lambda L)+\sqrt{\cdot}\right)^2\right)^{n+1}-1}}{m\lambda\Lambda\sinh(\lambda L) + \frac{1}{2}\left((m-1)\cosh(\lambda L) + \sqrt{\cdot}\right) + \frac{\sqrt{\cdot}}{\left(\frac{1}{4m}\left((m+1)\cosh(\lambda L)+\sqrt{\cdot}\right)^2\right)^{n+1}-1}}, \tag{4.2.15a}$$

where

$$\sqrt{\cdot} := \sqrt{(m+1)^2\cosh^2(\lambda L) - 4m}, \tag{4.2.16}$$

and $\lambda = \sqrt{2/R\Lambda}$.

4.3 Effective surface area and pulmonary efficiency

The surface area of the tree participating in transport may be identified through the inspection of Equation 4.2.5 with Equation 3.4.24:

$$\begin{aligned} I &= \frac{\pi R^2 D C_{ent}}{m\tilde{f}^{n+1}(\Lambda)} \\ &= W S_{eff} C_{ent}, \end{aligned}$$

which gives the effective surface area of the tree, $S_{eff,tree}$, as

$$S_{eff,tree}(\Lambda) = \frac{\pi R^2}{m}\left(\frac{\Lambda}{\tilde{f}^{n+1}(\Lambda)}\right). \tag{4.3.18}$$

In the Cayley tree model, the current is the quantity we directly computed and motivates

[3]For details, see appendix B.4.

a definition for its efficiency[19, 10, 1]:

$$\eta := \frac{\text{current crossing surface area of tree}}{\text{total current available for transport}}. \tag{4.3.19}$$

As a result of this definition, we may write the efficiency of the tree as:

$$\eta_{tree} = \frac{S_{eff,tree}}{S_{tree}},$$

where S_{tree} is the total surface area of the Cayley tree. An application of Equation 4.3.19 gives this as

$$\eta_{tree} = \frac{\pi R^2}{S_{tree}} \cdot \frac{\Lambda}{m\tilde{f}^{n+1}(\Lambda)}. \tag{4.3.20}$$

4.4 Asymptotic analysis of the oxygen current

A striking feature of the current profiles derived from Equations 4.2.14, 4.2.15a, and 4.2.16 is that plateaus in the current profile naturally emerge. We define the plateau as a region of the current profile in which $\partial I/\partial W = 0$[10, 1]. We will conduct an asymptotic analysis of Equation 4.2.14 in an attempt to understand the origin and parametric dependence of these plateaus upon the parameters of the system.

From Equation 4.2.15a, we find that the asymptotic current in the no screening regime ($\Lambda \to \infty$) is

$$I_{\Lambda\to\infty} \sim \frac{\pi R^2 DC_{ent}}{m} \cdot \frac{m^{n+1} + \frac{m\left(m^{n+1}-1\right)}{m-1} \cdot \frac{2L}{R}}{\Lambda + \frac{m(m^{n+1}-1)}{(m-1)^2} \cdot \frac{2L^2}{R}}, \tag{4.4.21}$$

and it is easy to see that $I_{\Lambda\to\infty} \propto \Lambda^{-1}$, which implies that the current is proportional to W. We may also compute the asymptotic current in the complete screening regime ($\Lambda \to 0$), where the current is completely diffusion-limited:

$$I_{\Lambda\to 0} \sim \pi DC_{ent}\sqrt{\frac{2R^3}{\Lambda}}, \tag{4.4.22}$$

and here it is clear that $I_{\Lambda\to 0} \propto \Lambda^{-1/2}$.

If we take $m >> 1$, Equation 4.4.21 may be rewritten in the following form:

$$I_{\Lambda\to\infty} \sim \frac{\pi R^2 DC_{ent}}{L} \cdot \frac{1+\frac{2L}{R}}{\frac{\Lambda}{m^n L}+\frac{2L}{R}},$$

where we have assumed $m^{n+1} >> 1$, and $m \approx m-1$. This expression suggests that if $\Lambda < 2m^n L^2/R$, then

$$I_{\Lambda\to\infty} \sim \frac{\pi R^2 DC_{ent}}{L} \cdot \left(1+\frac{R}{2L}\right) \tag{4.4.23}$$

as long as Λ is large enough for Equation 4.4.21 to hold.

Figure 4.9 depicts a program we have proposed, which is designed to quantify the plateau. The current is not well described by two power laws; however, we may find the appropriate intersections of the asymptotic currents (which themselves do satisfy simple power laws) with the constant current described by Equation 4.4.23, and infer its length $\Delta\Lambda$. According to Equation 4.4.23, if we input the data from Figure 4.9, we predict the plateau height as $I_{\Lambda\to\infty}/DC_{ent} \sim 1.99 \times 10^{-3}$–very close to the apparent value for the plateau within this figure.

Using Equations 4.4.21 and 4.4.22 as guides, we can conclude that the length of the plateau is related to the depth, n, and the number of daughter branches at each node, m, associated to the tree. As these quantities increase, the plateau width, as described in Figure 4.9, increases but is bounded from above and below by the currents which follow power law relationships.

4.5 Results

In this chapter we analyzed the performance of our model as in Figures 4.5 to4.8. The human lung transports and binds oxygen to the hemoglobin of the red blood cells within the pulmonary arteries and is subject to restrictions in both its structural and transport parameters. Nevertheless, the lung successfully performs under a wide range of varying conditions, and these regulating mechanisms of fault tolerance are not well understood. In this context, our model may be used to study the origin of these mechanisms and to

determine how they couple to the lung's performance as a gas exchanger.

In Figures 4.5 and 4.6, we indicate the dependence of both the oxygen current and the efficiency of the acinar gas exchanger on the permeability of the alveolar membranes, W. We have chosen two cases to exhibit: $2R = 0.01$ cm and $2R = 0.1$ cm. In both cases, the oxygen current displays a tolerance to error in membrane permeability, and we found that as the diameter of the branch increases, the current also increases. This feature is due to the increase in oxygen available for transport as the entrance diameter increases.

Another feature associated with the branch diameter is the length of the current plateau, which describes its tolerance to changes in membrane permeability. Previous treatments of the airways have predicted such an effect[10, 1], and these authors attribute its emergence as a consequence of diffusional screening. More specifically, if we take the current as $I = DC_{ent}S_{eff}(\Lambda)/\Lambda$, then for $I =$ constant we have $S_{eff}(\Lambda) \approx \Lambda$. We saw that this occurs, in the diffusion-limited case, when $\Lambda \propto R$. For the reaction-limited current, we found a screening transition to occur at $\Lambda \approx m^2 2L^2/R$ (when $m >> 1$).

In our treatment of the airways, we take the exploration length as a measure of its active zones. As a consequence, the emergence of the plateaus in our treatment may be related to that in other models. The plateaus emerge as the surface area of the tree increases, and in turn, the surface area of the tree depends on the structural parameters R, L, m, and n. Therefore, adjustment in these parameters will lead to the presentation of plateaus in the current.

In support of this hypothesis, Figure 4.4 provides a contrast between the emergence of plateaus with fixed $m = 2$, and a tree with $n = 2$ fixed (inset). We find that both trees produce plateaus; however, the tree with n variable provides an efficient way to quickly fill the available space while maintaining its ability to tolerate fluctuations in membrane permeability. This suggests that the lung's simple dichotomous branching scheme automatically maximizes the total membrane surface area, while simultaneously improving its ability to supply oxygen to the blood over a wide range of operating conditions.

The efficiency of the gas exchanger is illustrated within Figures 4.5, 4.6, and 4.7. We found that for trees with fixed $m = 2$, the efficiency of the Cayley tree decreases with

increasing n. We conclude that a "larger" tree is less efficient, but is also less sensitive to changes in membrane permeability. This feature has several advantages, as the gas exchanger requires no external mechanism to regulate its performance, and it relies completely on its fixed structure to maintain the homeostatic regulation in the current. A further advantage is in the tree's increased ability to quickly fill the available space left open by the terminal branches of the bronchial tree. This allows a maximum surface area over which to distribute the alveolar membranes.

In Figure 4.7 we varied the number of daughter branches extending from each node in the Cayley tree. As in the case of Figure 4.6, we found that the most efficient structural configuration is the tree containing the fewest number of total branches. These observations support predictions made through the expression for the efficiency, $\eta = S_{eff}/S_{tree}$. If S_{tree} increases faster than S_{eff}, then we would expect the efficiency of the gas exchanger to decrease.

To isolate the global dependence of the current on the structural parameter m, we compared two trees similar in the total number of branches they contain. One choice presented to a growing tree is how many daughter branches it should form at each branch point. We see from Figure 4.8 that a more efficient tree is the one in which its growth is dominated by daughter branching over generational depth, $(m > n)$, however, such efficiency comes at a cost to its ability to regulate oxygen current under a loss of permeability. This suggests that a tree minimizing its daughter branchings while simultaneously maximizing its depth, results in a system that quickly fills the available space, maximizes alveolar surface area, and produces a gas exchanger in which homeostasis emerges as a regulating mechanism of the oxygen current.

We found that the tree works to simultaneously optimize its tolerance to error and to maximize its overall efficiency. In our model, diffusional screening of the Cayley tree's surface from diffusing particles is of critical importantance to its operation as a gas exchanger. We find that the tree "opens up" more of its surface to generate an increase in oxygen current, while simultaneously increasing its efficiency at a cost of reducing its tolerance to error. We conclude that to reach these goals, a growing tree should minimize its daughter

branchings, m, while simultaneously maximizing its depth–a mechanism that maximizes the total surface area of the membranes, while quickly filling the space left empty by the termination of the bronchial tree.

4.6 Summary and Conclusions

Equations 4.2.14 and 4.2.15a report a remarkably analytic solution for the oxygen current crossing the alveolar membranes of the tree. Modeling the acinar airways is an especially difficult task because the alveoli form a space filling surface, and an exact analytic solution of the full boundary-valued equation of motion is beyond current methods. We introduced a simplified model of the airways that relied upon the fact that the exploration length appears within the equations of motion, and we hypothesized that the active zones of the alveolar membranes are represented through this tunable parameter. We found a remarkably analytic solution for the oxygen current crossing the alveolar membranes of the tree, which relies on very few structural and transport parameters.

From the study of our model we found that the the tree automatically regulates oxygen current through its structure, in part, by the optimization of the parameters n and m. We calculated the efficiency of our model, and found that as the structural parameters are tuned to represent a "larger" tree, the efficiency of the gas exchanger decreases. From these results, we concluded that a smaller tree is more efficient but is less robust against changes in membrane permeability. Similar conclusions have previously been reported in numerical studies of other model geometries[9].

We studied the current plateaus and designed a method to quantify their width. We found, as a rule of thumb, that if the depth of the tree increases then so does the width of the plateau. Bounds for $\Delta\Lambda$ describing the width of the current plateau can be found numerically, and will depend upon both the number of daughter branches across a node, as well as upon the depth of the tree. The width increases much more rapidly with an increase in n, rather than with an increase in m. This follows from the fact that an exponential growth in the number of branches within a dichotomously branching tree, $N \propto$

2^n, increases the number of branches within the tree (thus its surface area) far more rapidly than polynomial growth in its number of branches $N \propto m^2$.

In conclusion, we found that the current generated by the Cayley tree model exhibits screening transitions that do not exist in the current generated by a single branch, studied within chapter 3. We investigated the current plateaus and found asymptotic relationships in the analytic formula which supports the scaling relationships observed in their graphical representations. We interpreted these plateaus as representing the homeostatic regulation of oxygen current by the tree. Through this analysis we showed, as a general result, that a smaller tree is more sensitive to changes in its surface permeability. Though a larger tree uses less of its surface area in the transport of particles across it, and hence possesses a lower efficiency, we found that such a tree is more robust to error in its transport parameters. In general, we concluded that such a tree operates by competing to maximize its generated current, and thus its surface area accessed by particles, while simultaneously maximizing its tolerance to error. We showed that such a competition results in a choice of $m = 2$, which demonstrates a natural choice for biological structures that work as a distribution network in the transport of mass by diffusion.

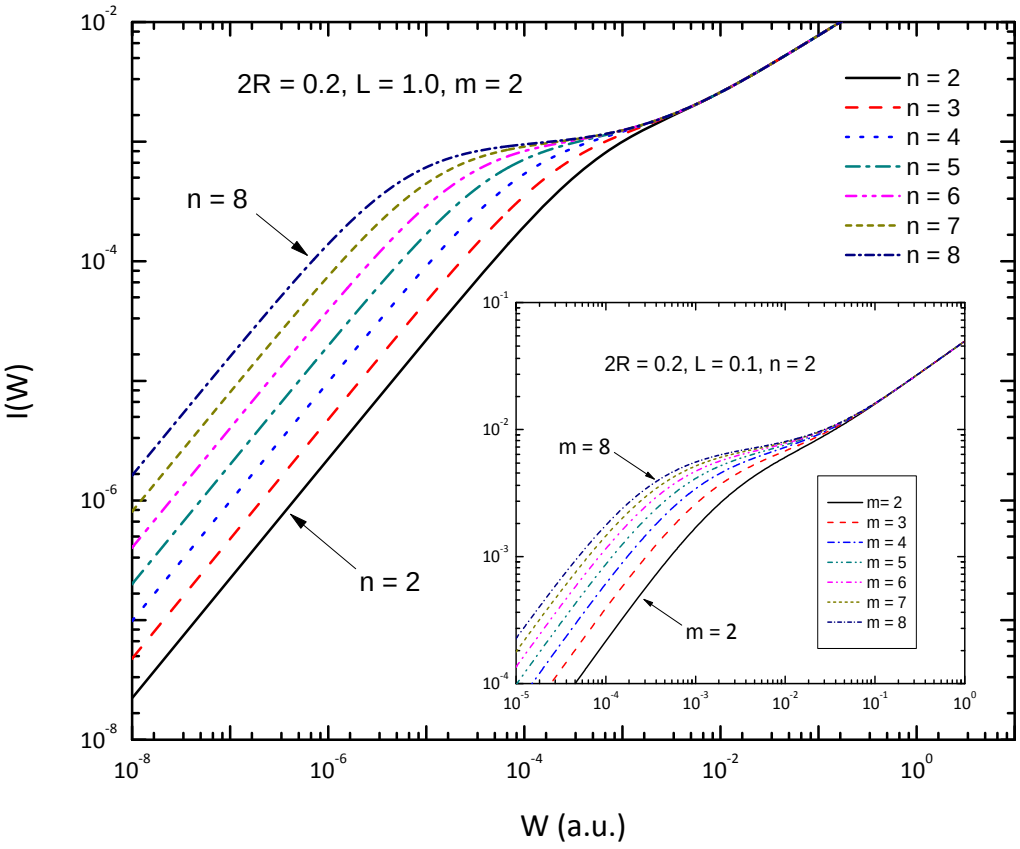

Figure 4.4: Graph of Equation 4.3.19. The number of daughter branches extending from each parent branch is fixed and taken to be m = 2, while the depth of the tree is fixed by n = 2 (inset).

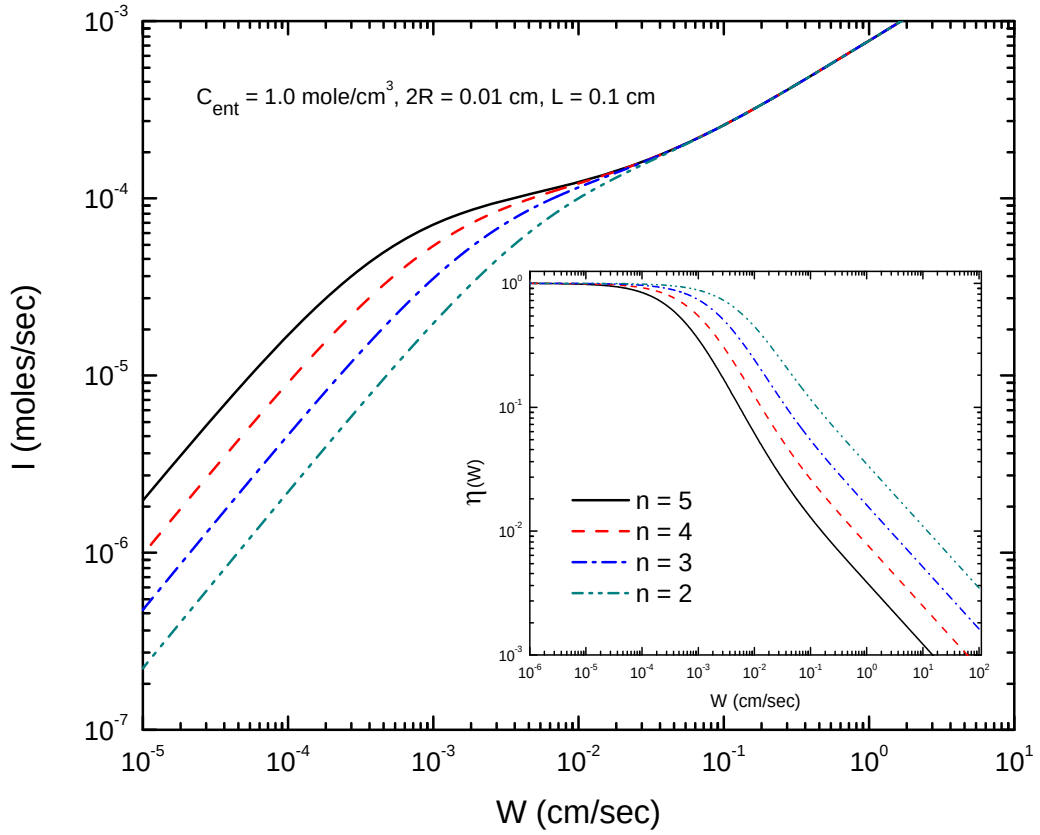

Figure 4.5: Oxygen current in the equi-length and width model, with D = 0.243 cm^2 / sec, $m = 2$, $2R = 0.01$ cm, and $L = 0.1$ cm.

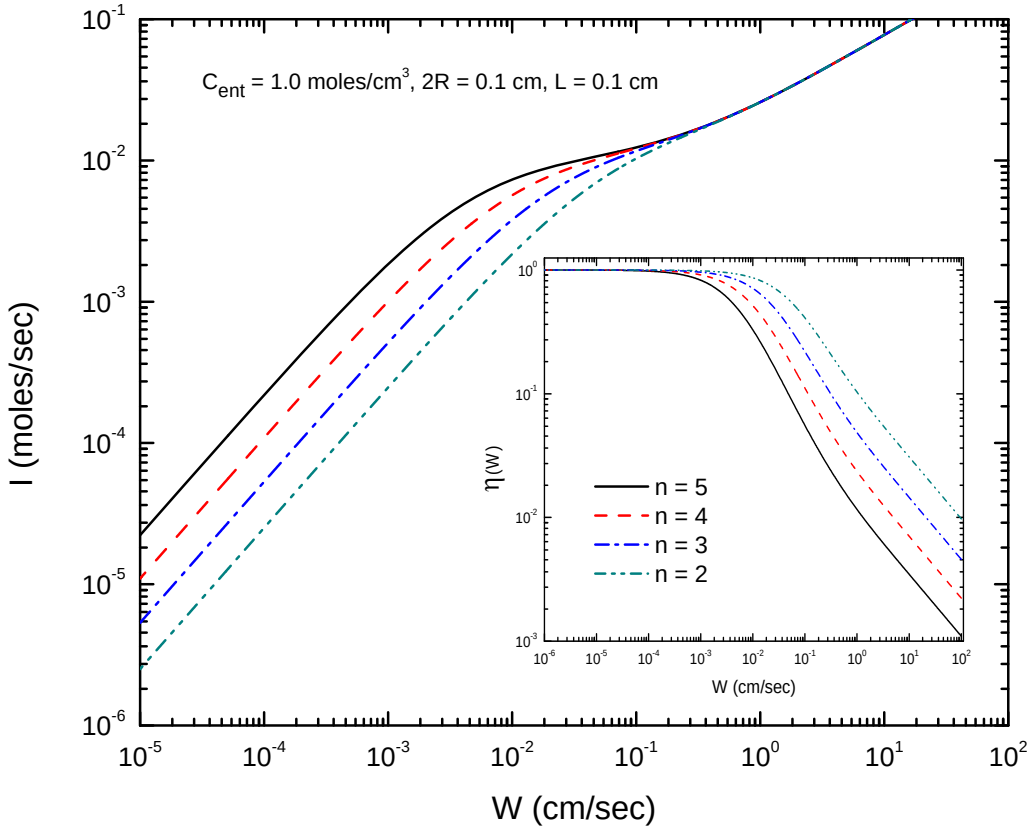

Figure 4.6: Oxygen current in the equi-length and width model, with D = 0.243 cm^2 / sec, $m = 2$, $2R = 0.1$ cm, and $L = 0.1$ cm.

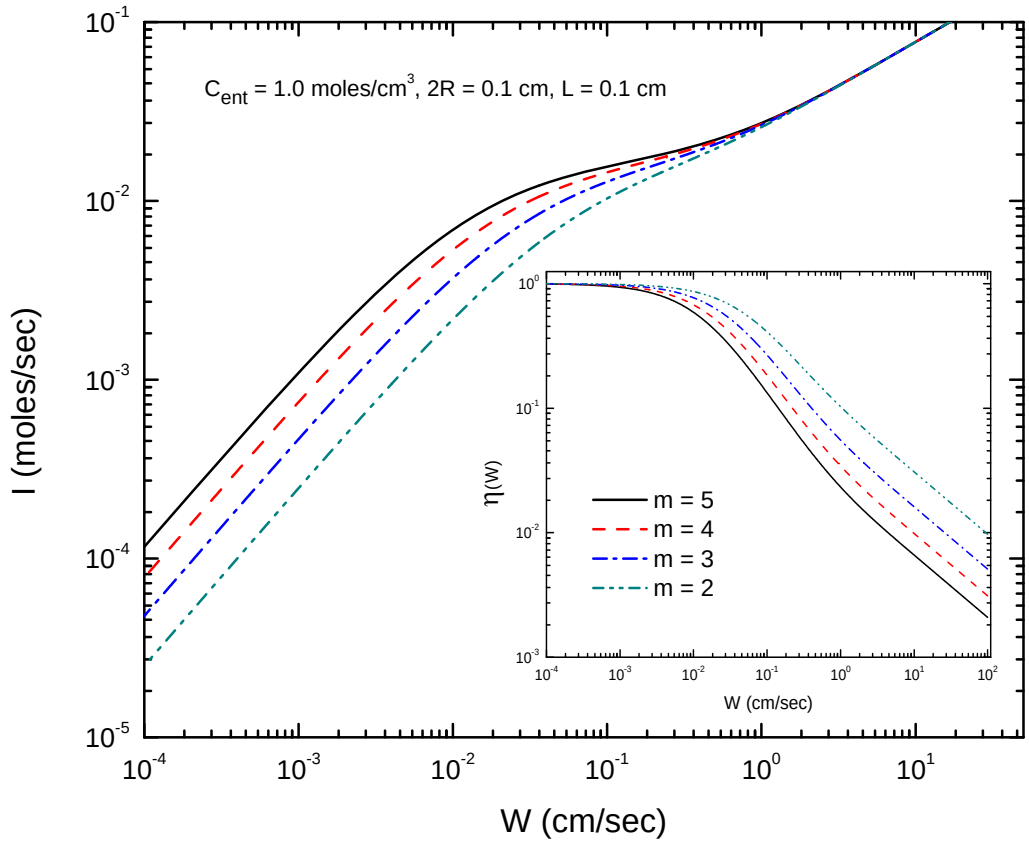

Figure 4.7: Oxygen current in the equi-length and width model for several values of m, with $n = 2$ and $D = 0.243$ cm^2 / sec.

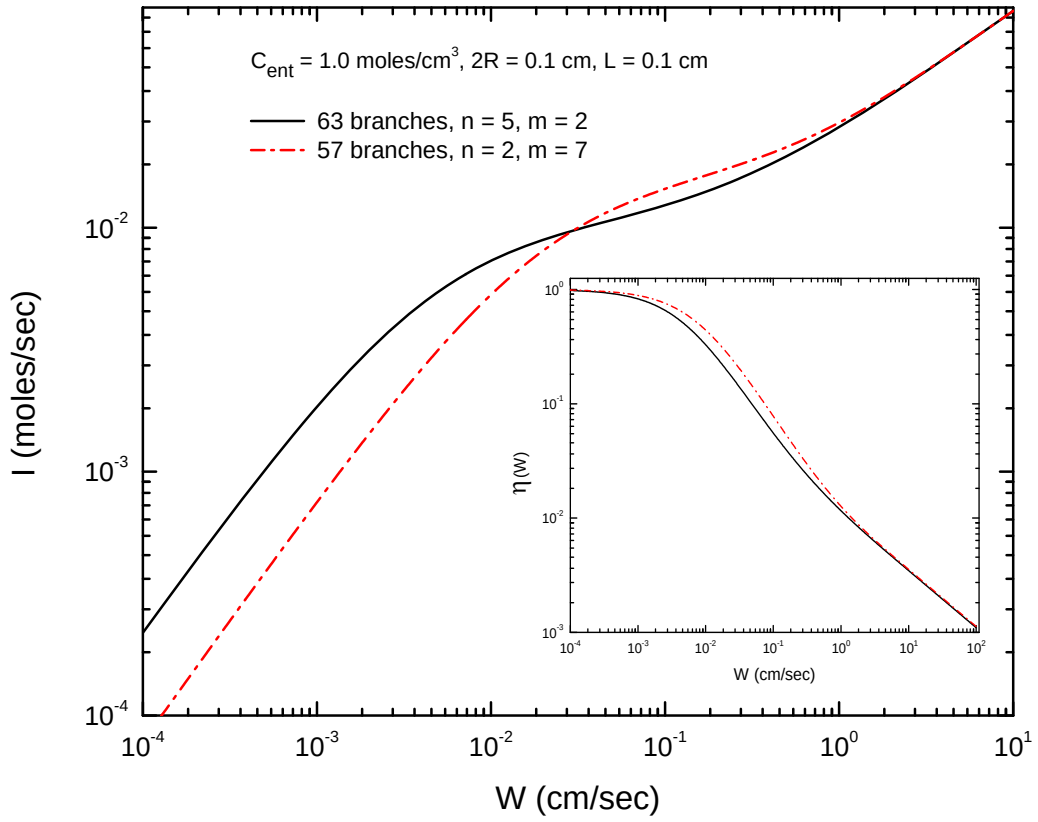

Figure 4.8: Contrast of oxygen current in two cases: $m = 7$ and $n = 2$, and $n = 5$ and $m = 2$.

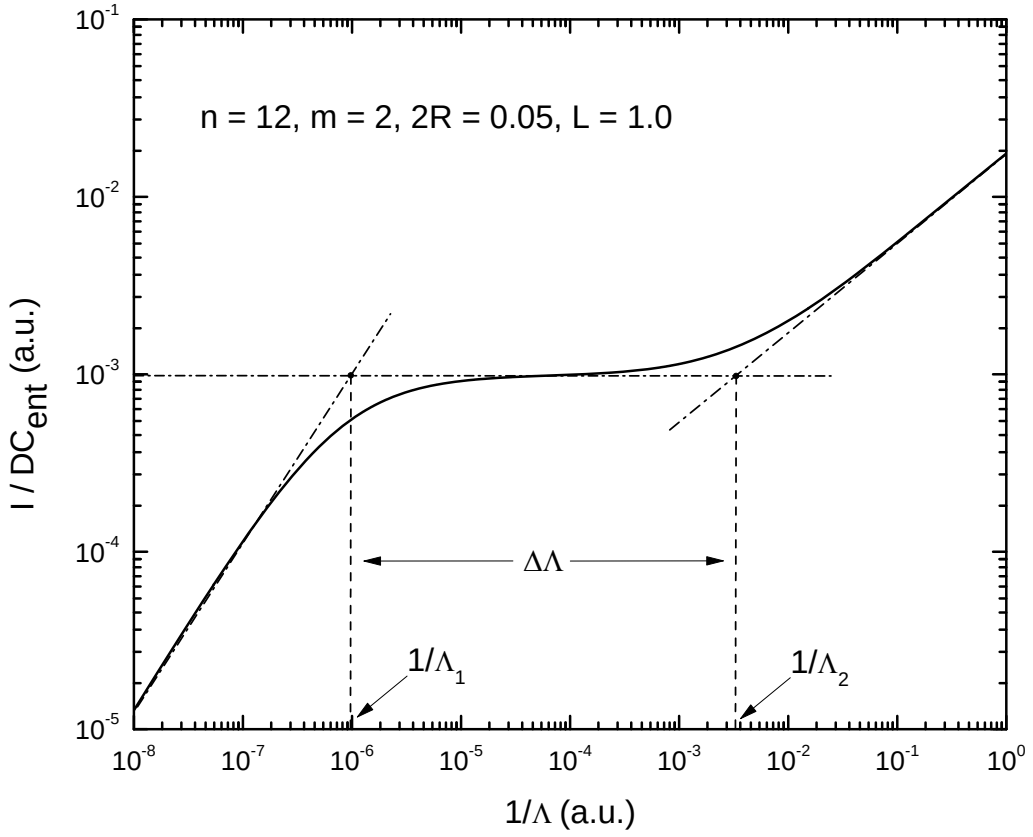

Figure 4.9: Suggested method to quantify the current plateau.

Chapter 5

Geometric aspects of the Cayley tree

5.1 Introduction

In this chapter we study the geometry of the Cayley tree and investigate its ability to fill the embedding space. Our goal is to identify the circumstances under which the scaling exponents of the Cayley tree converge to those generated through approximations of its Hausdorff dimension. A thorough understanding of such scaling behavior will allow us to quantitatively study the effects of different structural configurations of the Cayley tree on the particle current its surface generates.

5.2 Dimension-generating function

Fractal objects are often produced from generators with unequal parts. The scaling exponents of such objects are quantified through the dimension-generating functions (DGF)[24]. In this section we define the scaling ratio across branches within the Cayley tree, and also define the appropriate dimension-generating functions which will provide scaling ratios for both the length and width of the branches.

Let k label nodes within the Cayley tree, such that $k = 0, 2, \ldots, n$. The branches themselves are labeled with the subscript $k+1$, such that L_{k+1} gives the length of the $k+1$

branch.

In the construction of the graph, the k^{th} node is connected to the entrance of the $k+1^{th}$ branch. We label the daughter branches, connected at their entrance to node generation k, by a superscript (i), where $i = 1, 2, \ldots, m$. We will now define $p_{k+1}^{(i)}$ to be the ratio between the lengths of the i^{th} daughter branch, across the k^{th} node generation, and its associated parent branch:

$$p_{k+1}^{(i)} := \frac{L_{k+1}^{(i)}}{L_k}. \tag{5.2.1}$$

Similarly, we define $q_{k+1}^{(i)}$ to be

$$q_{k+1}^{(i)} := \frac{R_{k+1}^{(i)}}{R_k}. \tag{5.2.2}$$

Note that the scaling ratios are labeled in terms of their respective daughter branches. For a parent branch connected to the entrance of m-many daughter branches, the following expression holds across each node in the tree:[24]

$$(R_{k+1}^{(1)})^{\Delta_{DGF}} + (R_{k+1}^{(2)})^{\Delta_{DGF}} + \cdots + (R_{k+1}^{(m)})^{\Delta_{DGF}} = (R_k)^{\Delta_{DGF}},$$

where $k = 0, 2, \ldots, n$. It follows that

$$\sum_{i=1}^{m} (q_{k+1}^{(i)})^{\Delta_{DGF}} = 1.$$

Following Mandelbrot[24], we define the dimension-generating function to be

$$DGF(\Delta_{DGF}; q_{k+1}^{(i)}) := \sum_{i=1}^{m} (q_{k+1}^{(i)})^{\Delta_{DGF}}, \tag{5.2.3}$$

where the intersection $DGF(\Delta_{DGF}; q_{k+1}^{(i)}) = 1$ defines the scaling exponent Δ_{DGF}. We may similarly define a function relating the lengths of the branches across generations:

$$DGF(D_{DGF}; p_{k+1}^{(i)}) := \sum_{i=1}^{m} (p_{k+1}^{(i)})^{D_{DGF}}. \tag{5.2.4}$$

A powerful advantage of the dimension-generating function is that it coincides with the

Hausdorff dimension of the set[24][1]. We will use this feature to investigate the geometric scaling laws of the Cayley tree in the next section.

5.3 Scaling exponents

In this section we will develop expressions for the geometry of the tree which will be used to determine its scaling exponents. We will cover the tree with balls of diameter $2R_{n+1}$. As an approximation of the Hausdorff dimension, the box counting dimension satisfies $N(R_{n+1}) \propto {R_{n+1}}^{-D_f}$, where $N(R_{n+1})$ is the number of balls of radius R_{n+1} needed to cover the surface, and D_f is its fractal dimension.

Let $2R_1$ and L_1 be the width and length, respectively, of the entrance branch of a $(m+1)$-Cayley tree. We consider $2R_1$ and L_1 to be fixed, and use them as the primary parameters. Other choices, such as the width and length of the terminal branches, will not be used because, for example, the width and length of the terminal branches of the tree depend upon its depth.

5.3.1 Geometry of the Cayley tree model

Here will consider a $(m+1)$-Cayley tree of depth n, associated to each of its edges are cylinders of width ${2R^{(i)}}_{k+1}$, and length ${L^{(i)}}_{k+1}$ for each node $k = 1, 2, \ldots, n$. Scaling between its branches are given by Equation 5.2.1, and Equation 5.2.2. We also define $\prod_{j=1}^{0}(\cdot) := 1$. We give the following propositions without proof.

Proposition 5.3.1. *The total volume of an $(m+1)$-Cayley tree is given by*

$$V_{tree} = \pi {R_1}^2 L_1 \sum_{k=0}^{n} \prod_{j=1}^{k} \left(\sum_{i=1}^{m} (q_{j+1}^{(i)})^2 p_{j+1}^{(i)} \right). \tag{5.3.5}$$

Proposition 5.3.2. *For an $(m+1)$-Cayley tree of depth n its cumulative surface area is given by*

$$S_{cumulative} = 2\pi R_1 L_1 \sum_{k=0}^{n} \prod_{j=1}^{k} \left(\sum_{i=1}^{m} q_{j+1}^{(i)} p_{j+1}^{(i)} \right). \tag{5.3.6}$$

[1] At the time of this writing, we are unaware of any counterexamples.

Proposition 5.3.3. *Consider an $(m+1)$-Cayley tree of depth n. Then the total cross sectional area of its terminal branches is given by*

$$S_{end\ caps} = \pi {R_1}^2 \prod_{j=1}^{n} \left(\sum_{i=1}^{m} \left(q_{j+1}^{(i)} \right)^2 \right). \tag{5.3.7}$$

From Proposition 5.3.2 and Proposition 5.3.3, the total area of the tree may be written as

$$\begin{aligned} S_{tree} &= S_{\text{cumulative}} + S_{\text{end caps}} \\ &= 2\pi R_1 L_1 \sum_{k=0}^{n} \prod_{j=1}^{k} \left(\sum_{i=1}^{m} q_{j+1}^{(i)} p_{j+1}^{(i)} \right) + \pi {R_1}^2 \prod_{j=1}^{n} \left(\sum_{i=1}^{m} \left(q_{j+1}^{(i)} \right)^2 \right). \end{aligned} \tag{5.3.8a}$$

We will define the longitudinal path length of the tree, L_p, as the cumulative axial length along any path from the entrance node to a terminal node on the tree, as shown in Figure 5.1.

Proposition 5.3.4. *Consider an $(m+1)$-Cayley tree of depth n. Then its longitudinal path length is given by*

$$L_p = L_1 \sum_{k=0}^{n} \prod_{j=1}^{k} p_{j+1}^{(i_k)}. \tag{5.3.9}$$

Here, $i_k \in \{1, 2, \ldots, m\}$ (with $i_0 := 0$) is chosen at each branch point and defines the path that one takes from the entrance branch to the terminal sites. Accordingly, a tree may have several different longitudinal path lengths if daughter branches are not equal to each other in length or width. Conversely, if the daughter branches are all equivalent, then $p_{k+1}^{(1)} = p_{k+1}^{(2)} = \cdots = p_{k+1}^{(m)} = p_{k+1}$ and the index (i_k) may be dropped. Furthermore, if the scaling ratios satisfy $p = p_{k+1} = q = q_{k+1}$ for all $k = 0, 1, \ldots, n$, then Equation 5.3.9 may be written as

$$L_p = L_1 \sum_{k=0}^{n} (p)^k. \tag{5.3.10}$$

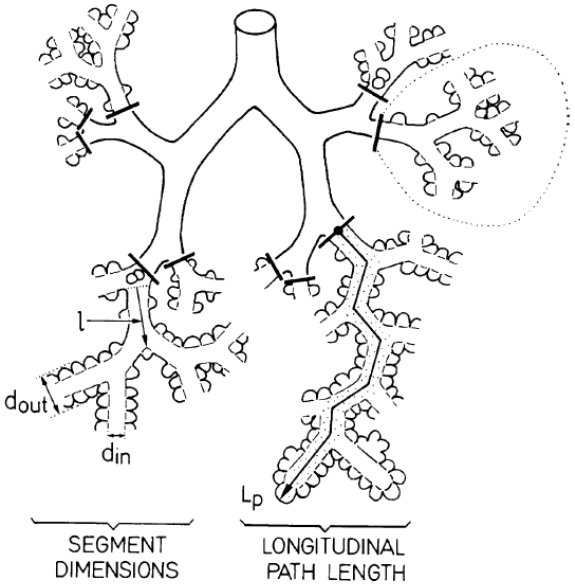

Figure 5.1: Longitudinal path length within the acinar airways of the human lung. Straight lines mark the beginning of the transitionary bronchioles [2].

5.3.2 Fractal dimension of the tree and its canopy

From Equations 5.2.1 and 5.2.2, we have $q^n = R_{n+1}/R_1$ and $p^n = L_{n+1}/L_1$, respectively. In these expressions, q and p satisfy $q \leq q^{(1)} \leq \cdots \leq q^{(m)}$ and $p \leq p^{(1)} \leq \cdots \leq p^{(m)}$, respectively. We are now in a position to make the following operational definitions:

Definition 5.3.1. Let $2R_{n+1}$ be the smallest branch diameter, of the set of terminal branches in a $(m+1)$-Cayley tree of depth n, such that it serves as its inner cut-off. We define the *canopy dimension*, D_f, to be the scaling exponent of the set covering the canopy of the tree, and satisfying $S_{\text{end caps}} \propto {R_{n+1}}^{2-D_f}$.

Definition 5.3.2. We define the *tree dimension*, D_{tree}, to be the scaling exponent of the set covering the cumulative surface area of a $(m+1)$-Cayley tree of depth n, in which the following expression is satisfied: $S_{tree} \propto {R_{n+1}}^{2-D_{tree}}$.

5.4 Results

When ${q^{(1)}}_{k+1} = {q^{(2)}}_{k+1} = q$ for all $k = 1, 2, \ldots, n$ with $m = 2$, we found that the scaling exponent of the dimension-generating function is equivalent to the fractal canopy dimension

of the Cayley tree for all choices of $q \in [0, 2^{-1/3}]$. This result is reflected in Figure 5.4. This is particularly interesting, as the dimension-generating function provides a more straightforward way to compute the scaling exponent, and thus the fractal canopy dimension.

More generally, we analyzed several different choices of $p^{(i)}$ and $q^{(i)}$ in order to determine the scaling exponents of Equations 5.2.3, 5.2.4, and 5.3.6 and to determine their relationship with those exponents defined by the associated dimension-generating functions. To preface this discussion we suggest the following definition:

Definition 5.4.1. Scaling within the Cayley tree is called *equiscaling* if, across a node $k \in \{1, 2, \ldots, n\}$, the following relations hold between its branches: $p^{(1)} = q^{(1)}, p^{(2)} = q^{(2)}, \ldots, p^{(m)} = q^{(m)}$.

We have chosen to define the equiscaling of the tree, instead of its self similarity, because self similar structures scale equally in each of their spacial coordinates.

In Figure 5.2 we have depicted a tree in which each daughter branch has the same structural properties as the others, i.e., $R_{k+1}^{(1)} = R_{k+1}^{(2)} = \cdots = R_{k+1}^{(m)}$ and $L_{k+1}^{(1)} = L_{k+1}^{(2)} = \cdots = L_{k+1}^{(m)}$. It follows from Equation 5.2.1, Equation 5.2.1, and the definition of the dimension-generating function, that $p = q = m^{-1/D_{DGF}}$. Its exponent, D_{DGF}, can be solved for analytically and is given by

$$D_{DGF} = -\frac{\ln m}{\ln p}.$$

From Figure 5.2 it is clear that convergence of the tree dimension and that of the dimension-generating function exists for values between two and three. This is not entirely surprising, as the tree dimension originates from the cumulative surface area of the tree, which is bounded from below by 2. A major conclusion of this analysis is that the dimension-generating function describes a scaling exponent equivalent to the tree dimension for $D_{tree} \in [2, 3]$.

In contrast to the scaling shown within Figure 5.2, Figure 5.3 depicts the scaling exponents of a dichotomously branching Cayley tree in which $p = p^{(1)} = q^{(1)}$, where $p^{(2)} = q^{(2)} = 2^{-1/3}$ is fixed. Generally, the exponents given by the cumulative surface

area of the tree and the dimension-generating function are not equivalent; however, it is interesting to note that there are two unique intersections in the curves of Figure 5.3. We expect that these two exponents converge for $p = 2^{-1/3}$, however, it is somewhat unexpected that another intersection exists for $p \approx 0.613$, which is apparently a consequence of the tree dimension underestimating the scaling exponent given by the dimension-generating function.

In Figure 5.4 we contrast the canopy dimension with the scaling dimension of the DGF under two conditions: (1) $q = q^{(1)} \in \left(0, 2^{-1/3}\right]$ with $q^{(2)} = 2^{-1/3}$ fixed, and (2) $q = q^{(1)} = q^{(2)} \in \left(0, 2^{-1/3}\right]$. Clearly the canopy dimension coincides with the scaling exponent of the dimension-generating function, described above in case (2), over its entire domain. From this we conclude that the canopy dimension is well-described by the dimension-generating function, in the case where the terminal branches are scaled to the same ratio q.

We also analyzed the total surface area of an equiscaled Cayley tree, and we found that convergence of its scaling exponent on that defined by the dimension-generating function exists between topological dimensions two and three.

5.5 Methods

5.5.1 Computation of scaling exponents

We conducted this study using the expressions given by Equation 5.3.8a and Equation 5.3.7, the results were given in Figure 5.2, Figure 5.3, and Figure 5.4. The computations were conducted by treating the scaling exponent as the slope in a log-log plot of the appropriate Cayley tree geometry, and n was chosen to be sufficiently large in order to generate a constant slope within the plot.

For example, we calculated the fractal dimension for the cumulative surface area of the Cayley tree by computing a set of coordinates $(q^n R_1, S_{\text{cumulative}})$, where the inner cut-off of the tree is connected to the width of the entrance branch by $R_{n+1} = q^n R_1$, under the assumption that $q \leq p$. For the purposes of computing the scaling exponents, we took R_1 and L_1 to be of unit length. We took n sufficiently large such that the asymptotic slope was

constant, $\ln(S_{\text{cumulative}})/\ln(q^n R_1) = 2 - D_{tree}$. In most cases we chose $n = 10^2$, otherwise we chose $n = 10^4$.

5.5.2 Useful theorems

For a Cayley tree in which $p = p^{(1)} = p^{(2)} = \cdots = p^{(m)}$ and $q = q^{(1)} = q^{(2)} = \cdots = q^{(m)}$, the scaling ratios connect the tree and canopy and dimension through $p = m^{-1/D_{tree}}$ and $q = m^{-1/D_f}$, respectively. We have taken p and q to be the same across all node generations within the tree. In such an equiscaled tree, the daughter branches within the same generation have equivalent widths and lengths.

In several cases, we used the following theorems to study the scaling behavior of the Cayley tree geometry.

Theorem 5.5.1. *Let the volume of an $(m+1)$-Cayley tree be given by Equation 5.5.19. Let R_{n+1} be the inner cut-off and satisfy $R_{n+1} < L_{n+1}$. For each $k = 1, 2, \ldots, n$, take $p_{k+1}^{(1)} = p_{k+1}^{(2)} = \cdots = p_{k+1}^{(m)} = p$ and $q_{k+1}^{(1)} = q_{k+1}^{(2)} = \cdots = q_{k+1}^{(m)} = q$. Then we have*

$$V_{tree} = \pi {R_1}^2 L_1 \frac{m^{1-2/D_f - 1/D_{tree}} \left(\frac{R_{n+1}}{R_1}\right)^{2 - D_f(1-1/D_{tree})} - 1}{m^{1-2/D_f-1/D_{tree}} - 1}. \tag{5.5.11}$$

Proof of Theorem 5.5.1. The volume of an $(m+1)$-Cayley tree, in which cylinders are associated with the graph edges, is given by Equation 5.5.19:

$$V_{tree} = \pi {R_1}^2 L_1 \sum_{k=0}^{n} \prod_{j=1}^{k} \left(\sum_{i=1}^{m} (q_{j+1}^{(i)})^2 p_{j+1}^{(i)} \right). \tag{5.5.12}$$

For each $k \in \{1, 2, \ldots, n\}$, we take $p_{k+1}^{(1)} = p_{k+1}^{(2)} = \cdots = p_{k+1}^{(m)} = p$ and $q_{k+1}^{(1)} = q_{k+1}^{(2)} = \cdots = q_{k+1}^{(m)} = q$. From Equation 5.5.12, these relations imply

$$V_{tree} = \pi {R_1}^2 L_1 \sum_{k=0}^{n} \left(m q^2 p\right)^k. \tag{5.5.13}$$

Equation 5.5.13 is a geometric series, and can be summed analytically:

$$\begin{aligned} V_{tree} &= \pi {R_1}^2 L_1 \frac{1-\left(mq^2p\right)^{n+1}}{1-mq^2p}, \\ &= \pi {R_1}^2 L_1 \frac{1-m^n q^{2n} p^n \left(mq^2p\right)}{1-mq^2p}. \end{aligned} \tag{5.5.14a}$$

Since $q^n = R_{n+1}/R_1$ and $p^n = L_{n+1}/L_1$, we have, from Equation 5.5.14a,

$$V_{tree} = \pi {R_1}^2 L_1 \frac{1-m^n \left(\frac{R_{n+1}}{R_1}\right)^2 \frac{L_{n+1}}{L_1} mq^2p}{1-mq^2p}. \tag{5.5.15}$$

We take the smallest length scale within the $(m+1)$-Cayley tree to be the inner cut-off of the tree, which is the radius of the terminal branch, R_{n+1}. Therefore n determines R_{n+1}, so we take $m^n = (R_{n+1}/R_1)^{-D_f}$. We apply this to Equation 5.5.15 and obtain

$$V_{tree} = \pi {R_1}^2 L_1 \frac{1-m^{1-2/D_f-1/D_tree} \left(\frac{R_{n+1}}{R_1}\right)^{2-D_f} \frac{L_{n+1}}{L_1}}{1-m^{1-2/D_f-1/D_tree}}, \tag{5.5.16}$$

where we used $q = m^{-1/D_f}$ and $p = m^{-1/D_{tree}}$. We need to write L_{n+1}/L_1 in terms of R_{n+1}/R_1, and we take their product to obtain

$$\frac{L_{n+1}}{L_1} = \left(\frac{R_{n+1}}{R_1}\right)^{-D_f/D_{tree}}.$$

We apply this expression to Equation 5.5.16 and arrive at

$$V_{tree} = \pi {R_1}^2 L_1 \frac{m^{1-2/D_f-1/D_{tree}} \left(\frac{R_{n+1}}{R_1}\right)^{2-D_f(1-1/D_{tree})} - 1}{m^{1-2/D_f-1/D_{tree}} - 1}.$$

□

Corollary 5.5.2. *Let the $(m+1)$-Cayley tree be equiscaled, such that $p_{k+1} = q_{k+1} = m^{-1/D_f}$ for all $k \in \{1, 2, \ldots, n\}$. Then its volume given by*

$$V_{tree} = \pi {R_1}^2 L_1 \frac{m^{1-3/D_f} \left(\frac{R_{n+1}}{R_1}\right)^{3-D_f} - 1}{m^{1-3/D_f} - 1}. \tag{5.5.17}$$

Theorem 5.5.3. *Let the cumulative surface area of an $(m+1)$-Cayley tree be given by Equation 5.3.6. Also, let R_{n+1} be the inner cut-off and satisfy $R_{n+1} < L_{n+1}$. For each $k \in \{1, 2, \ldots, n\}$, take $p_{k+1}^{(1)} = p_{k+1}^{(2)} = \cdots = p_{k+1}^{(m)} = p$ and $q_{k+1}^{(1)} = q_{k+1}^{(2)} = \cdots = q_{k+1}^{(m)} = q$. Then the cumulative surface area is given by*

$$S_{cumulative} = 2\pi R_1 L_1 \frac{m^{1-1/D_f-1/D_{tree}} \left(\frac{R_{n+1}}{R_1}\right)^{1-D_f(1-1/D_{tree})} - 1}{m^{1-1/D_f-1/D_{tree}} - 1}. \tag{5.5.18}$$

The proof of the remaining theorems is sufficiently similar to that of Theorem 5.5.1, so that we do not include them here.

Corollary 5.5.4. *Let the $(m+1)$-Cayley tree be equiscaled, such that $p_{k+1} = q_{k+1} = m^{-1/D_f}$ for all $k \in \{1, 2, \ldots, n\}$. Then its cumulative surface area is given by*

$$S_{cumulative} = 2\pi R_1 L_1 \frac{m^{1-2/D_f} \left(\frac{R_{n+1}}{R_1}\right)^{2-D_f} - 1}{m^{1-2/D_f} - 1}. \tag{5.5.19}$$

Theorem 5.5.5. *Let the total cross-sectional area of the terminal branches in an $(m+1)$-Cayley tree be given by Equation 5.3.7. Let R_{n+1} be the inner cut-off and satisfy $R_{n+1} < L_{n+1}$. For each $k \in \{1, 2, \ldots, n\}$, take $p_{k+1}^{(1)} = p_{k+1}^{(2)} = \cdots = p_{k+1}^{(m)} = p$ and $q_{k+1}^{(1)} = q_{k+1}^{(2)} = \cdots = q_{k+1}^{(m)} = q$. The cross-sectional area of the terminal branches is then given by*

$$S_{end\ caps} = \pi {R_1}^2 \left(\frac{R_{n+1}}{R_1}\right)^{2-D_f}. \tag{5.5.20}$$

5.6 Summary and conclusions

In this chapter we have defined scaling exponents for the Cayley tree and derived expressions for the scaling properties of the tree. Specifically, we defined the tree and canopy dimensions, and we demonstrated their equivalence with the scaling exponents of the dimension-generating function for fractal dimensions between two and three. We found that $D_f = \Delta_{DGF}$.

In this way, we were able to identify the parameter values under which we may use the dimension-generating function to produce the tree or canopy dimensions. We applied these relations to the area of the tree and its canopy, generating analytical expressions for the global scaling structure of the tree.

A major accomplishment of this analysis is our ability to quantify the canopy dimension of the tree, using a simple analytic expression. Under these circumstances, the main scaling parameters may be transformed from the scaling ratios, p and q, to the fractal dimension of the canopy, D_f. Our analysis demonstrated the equivalence between the scaling ratios and the canopy dimension of the Cayley tree. The equiscaled tree is therefore equivalently described by either its scaling ratio or canopy dimension, which provides a powerful connection between the local and global structure of the Cayley tree.

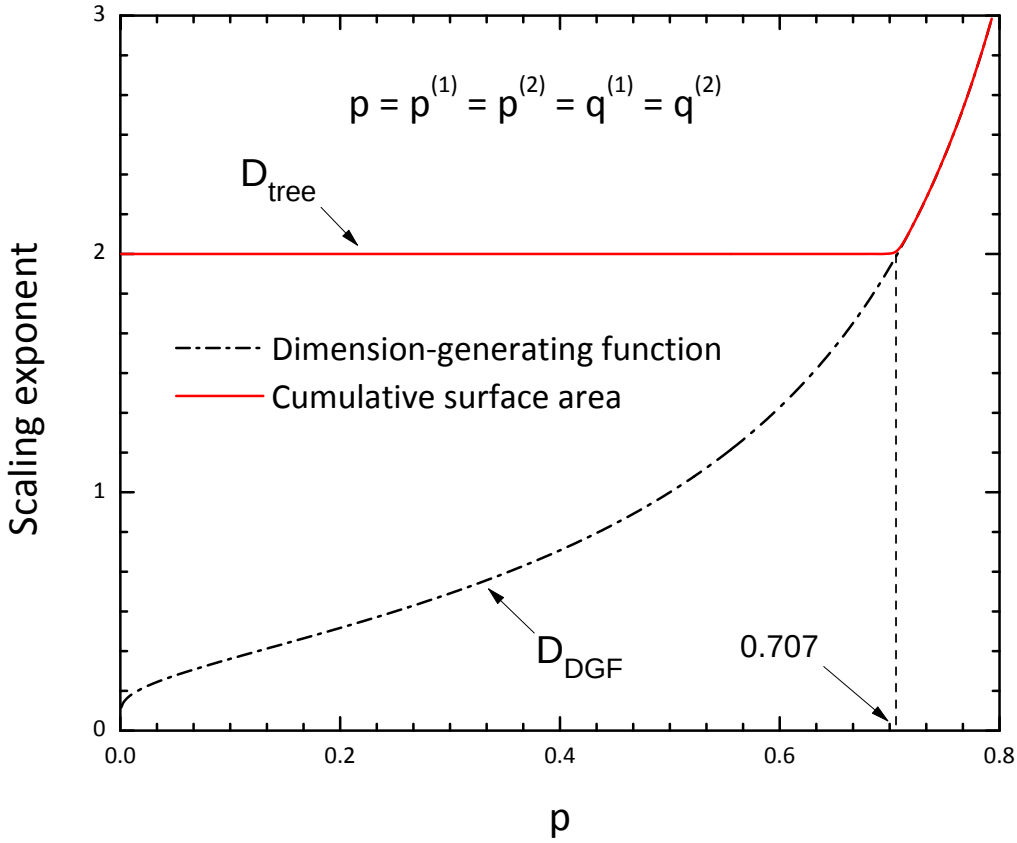

Figure 5.2: Scaling exponents in a Cayley tree given by the dimension-generating function and the cumulative tree area, for which $m = 2$ and $p = p^{(i)} = q^{(i)}$.

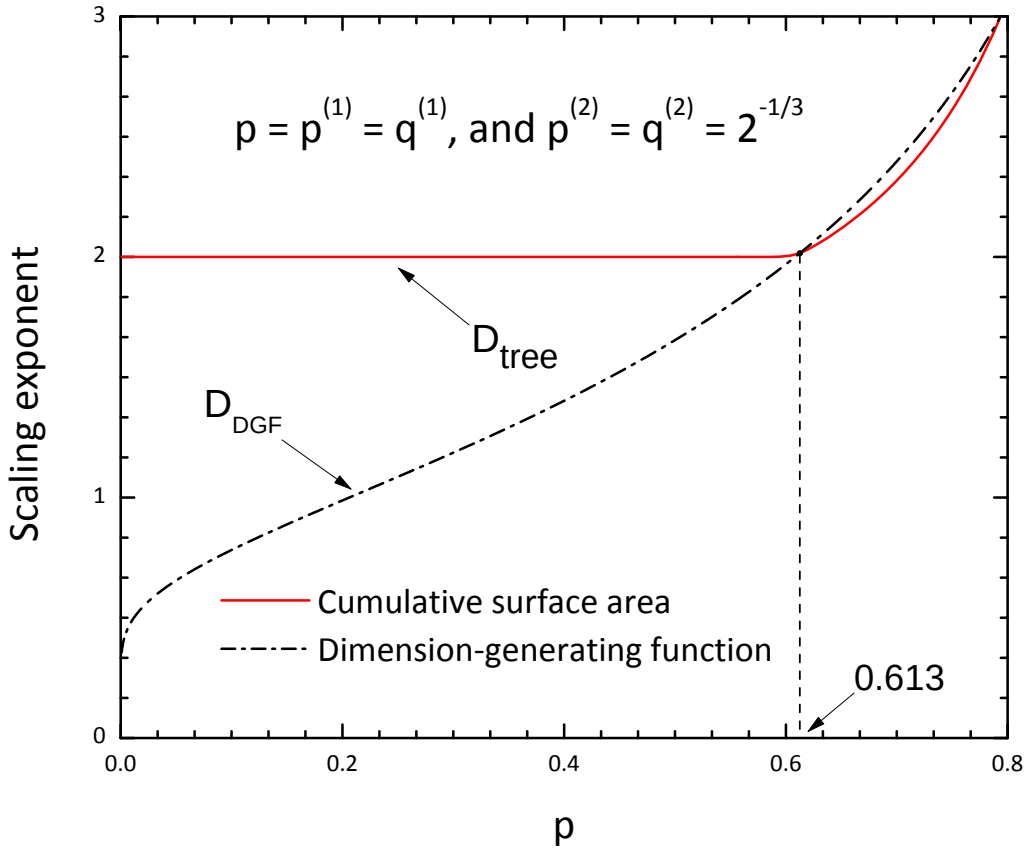

Figure 5.3: Scaling exponents in a Cayley tree given by the dimension-generating function (DGF) and the cumulative tree area, for which $m = 2$, $p = p^{(1)} = q^{(1)}$, and $p^{(2)} = q^{(2)} = 2^{-1/3}$.

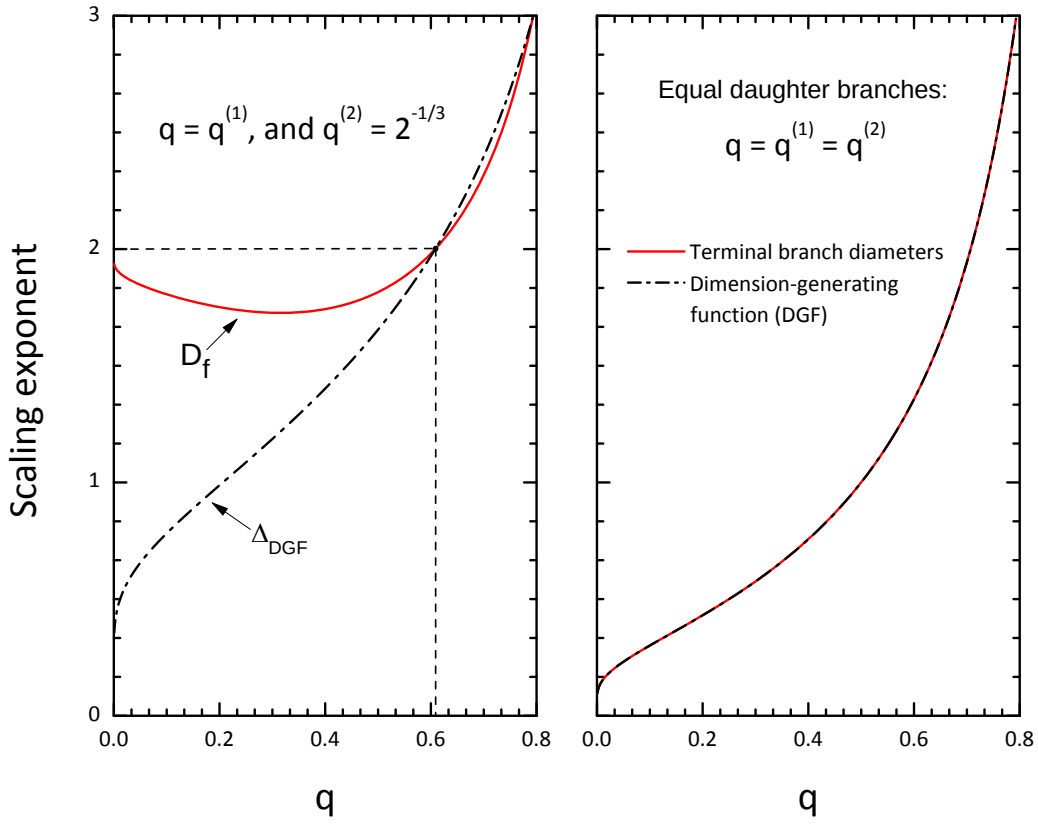

Figure 5.4: Scaling exponents for the diameters of the terminal branches in the Cayley tree given by the fractal canopy dimension and the dimension-generating function, and demonstration of their equivalence (Δ_{DGF}=D_f) when daughter branches are of equal width and length.

Chapter 6

Fractal model of oxygen transport

6.1 Introduction

In chapter 4 we developed a model of oxygen transport within the lung, under the assumption that each branch in the tree had the same length and width. In what follows, we will refer to this model as the equi-length and width model.

The introduction of branch scaling generates a nontrivial extension of the equi-length and width model, and in this chapter we develop such a model and study its scaling behavior. Specifically, we investigate the space-filling ability of the tree through its tunable structural parameters and we show that such a space-filling configuration reproduces the robust behavior observed in the equi-length and width model, which is described within chapter 4.

6.2 Methods

In this section we will describe an extension of the equi-length and width model to cases in which the tree fills, or partially fills, its embedding space. To accomplish this we will apply the scaling relations p and q to our model (see chapter 5), resulting in a tree that possesses a parametric dependence on the fractal dimension of the canopy, D_f. We will use this parametric dependence to investigate the relationship between the oxygen current and the structural composition of the tree.

Consider the equi-length and width model of oxygen transport, which we described in chapter 4. Recall that we began by propagating the current back through the tree, beginning with the terminal branches. We then identified the current leaving the alveolar membranes of the model tree with the current entering the tree. A similar procedure can be used to compute the Möbius matrix for the oxygen current in the fractal tree. In particular, we will write the oxygen concentration within the terminal branches in terms of the scaling ratios p and q. We will then propagate this current back through the tree under the assumption that each daughter branch is equal to all others in its generation, regarding width and length.

The Möbius matrix associated with the map $\tilde{f}_k$ (see Equation 2.2.7 and 2.2.5) is given by[1]

$$F_{ij}^{(k)} = \begin{pmatrix} q^{-2}\sqrt{\frac{2}{R_1\Lambda}} & q^{\frac{k-5}{2}} \tanh\left(\sqrt{\frac{2{L_1}^2}{R_1\Lambda}}(\frac{p}{\sqrt{q}})^{k-1}\right) \\ q^{\frac{1-k}{2}}\frac{2m}{R_1\Lambda}\tanh\left(\sqrt{\frac{2{L_1}^2}{R_1\Lambda}}(\frac{p}{\sqrt{q}})^{k-1}\right) & m\sqrt{\frac{2}{R_1\Lambda}} \end{pmatrix}, \tag{6.2.1}$$

where R_1 and L_1 are the respective radius and length of the entrance branch, and p and q define the scaling ratios across the length and width of the branches within the tree, respectively. In an equiscaled tree, the width and length of the terminal branches are connected to those of the entrance branch through the relations $R_{n+1} = q^n R_1$ and $L_{n+1} = p^n L_1$. We then compute the products of $F_{ij}^{(k)}$:

$$\prod_{k=1}^{n+1} F_{ij}^{(k)} \cdot \begin{pmatrix} D \\ W \end{pmatrix} = \begin{pmatrix} D_{eff} \\ W_{eff} \end{pmatrix}, \tag{6.2.2}$$

The transmembrane oxygen current for the fractal Calyey tree model may be expressed as[2]:

$$I = \frac{D\pi {R_1}^2 C_{ent}}{mq^2} \cdot \frac{W_{eff}}{D_{eff}}, \tag{6.2.3}$$

with D_{eff} and W_{eff} computed from Equation 6.2.2.

[1] Please see Appendix B.

[2] Please see Appendix B.3 for details.

6.3 Results

In many respects, the extension of the equi-length and width model to the fractal representation reveals structure in the oxygen current which is similar to that of the equi-length and width model. For example, we found striking plateaus in the oxygen current using the equi-length and width model, and this feature is reproduced in the fractal representation, which we observe from Figure 6.1. Specifically, we can see that as n increases, the gas exchanger becomes slightly more robust to fluctuations in oxygen current. This behavior was also observed in the equi-length and width model.

Another feature reproduced through the fractal extension of the equi-length and width model is demonstrated through the efficiency of the gas exchanger. Inset within Figure 6.1, we find that the most efficient gas exchanger is one in which the depth of the tree is minimized. Such a tree possesses a minimum of membrane surface area; therefore, the gas exchanger uses a greater fraction of its surface to generate a current. In this way, most surface sites are unscreened and the effective surface area approaches the total surface area of the gas exchanger.

Entirely new features are also observed in the fractal extension of the equi-length and width model. In contrast to the equi-length and width model, Figure 6.1 indicates that as the depth of the tree increases, the magnitude of the current also increases. This feature was observed within the equi-length and width model of the tree in chapter 4; however, the current became independent of n in the large W limit; i.e. in the complete screening regime. In contrast with this behavior, we find that the fractal tree exhibits a current in the complete screening regime that depends upon the depth of the tree.

The mechanism by which the oxgyen molecules retain information about the tree's generational depth can be explained through the scaling of branch diameters within the tree. Consider the oxygen current depicted in Figure 6.2. In this case we have taken $p = 2^{-1/3}$ and $q = 1$. In other words, the length of the branches scale to fill the embedding space, while the diameters scale to overfill the available space. In comparing Figure 6.2 with Figure 6.1, we find that in the complete screening regime, the current depends upon the depth of the tree for $q < 1$.

To explain this n-dependence of the oxygen current, we first recall how the the tree is constructed. We define the geometry of the terminal branches through the parameters $2R_{n+1}$ and L_{n+1}. Through the scaling parameters, p and q, the lengths and diameters of the branches increase as we move from the terminal branches of the tree to its entrance branch. We know from the equi-length and width model that if the branch diameter increases, then the oxygen current will correspondingly increase–a result of the increase in oxygen molecules availabe for transport across the entrance of the tree. Since q regulates the diameter of the entrance branch, it follows that as the depth of the tree increases, the diameter of its entrance branch will correspondingly increase and therefore, the current will increase.

A triumph of our extension of the equi-length and width model to a fractal representation is that we may now study how the structure of the tree affects its performance as a gas exchanger. As we can see from Figure 6.3, the current plateaus are sensitive to the fractal dimension of the tree canopy. If the tree canopy is planar, then the current is sensitive to the membrane permeability. In comparison with the fractal representation, the equi-length and width model provides the best stability; however, this is to be expected as the equi-length and width model quickly overfills space and maximizes the surface area of the alveolar membranes.

Given two trees with similar homeostatic performance, one in the equi-length and width model and one in the fractal representation, an advantage of the equi-length and width model over the fractal representation is that homeostasis emerges in a tree of smaller depth. We may see that this is indeed the case by analyzing Figure 6.3. Here, the equi-length and width model provides the most robust current in any of the trees with $n = 5$.

Figure 6.4 gives the currents and efficiencies for several tree configurations, and we find that the least efficient configuration is $n = 5$, $m = 2$. This result suggests that between a tree with a canopy in the plane, and a tree with a space-filling canopy, the tree with space-filling canopy will be the preferred architecture due to its increased ability to tolerate fluctuations in permeability.

6.4 Summary and Conclusions

In this chapter we extended the equi-length and width model of the Cayley tree to a fractal representation, where the structural orientation of the tree can be described through the dimension of its canopy, D_f. Using this extended representation of the equi-length and width model, we were able to analyze the effects of several different choices of canopy dimensions on the current leaving the tree. Generally, we found that the most efficient configuration of the tree is one in which the tree canopy fills a plane. The reason for this result is that the tree wastes a minimum of its surface area for oxygen transport. In contrast to this, a tree with a space filling canopy will be less efficient in utilizing its surface area for transport; however, such a configuration allows the tree to adapt to changing demands by "opening up" more surface area for transport.

We compared trees in the fractal representation with those of the equi-length and width model. Our results showed that trees in the fractal representation reproduced key features found within the equi-length and width model. One such result is that of oxygen regulation by homeostasis. We found that a tree with a canopy dimension of two exhibits no current plateau when $n \leq 5$. Under these conditions, we saw that a tree with a canopy dimension of three performed better, but only weakly displayed an ability to tolerate error in membrane permeability.

We compared these trees in the fractal representation, with one in the equi-length and width model. Our results showed that the efficiency of the equi-length and width model is lower than those in the fractal representation; furthermore, its current plateaus are far more pronounced than those in the fractal representation. We conclude that a gas exchanger which maximizes its alveolar surface area, while simultaneously minimizing its efficiency, is the one which maximizes its canopy dimension to fill, or overfill, the available embedding space, given a target generational depth. Indeed, there is a danger of branch overlap in trees with $D_f \geq 3$ and large enough n.

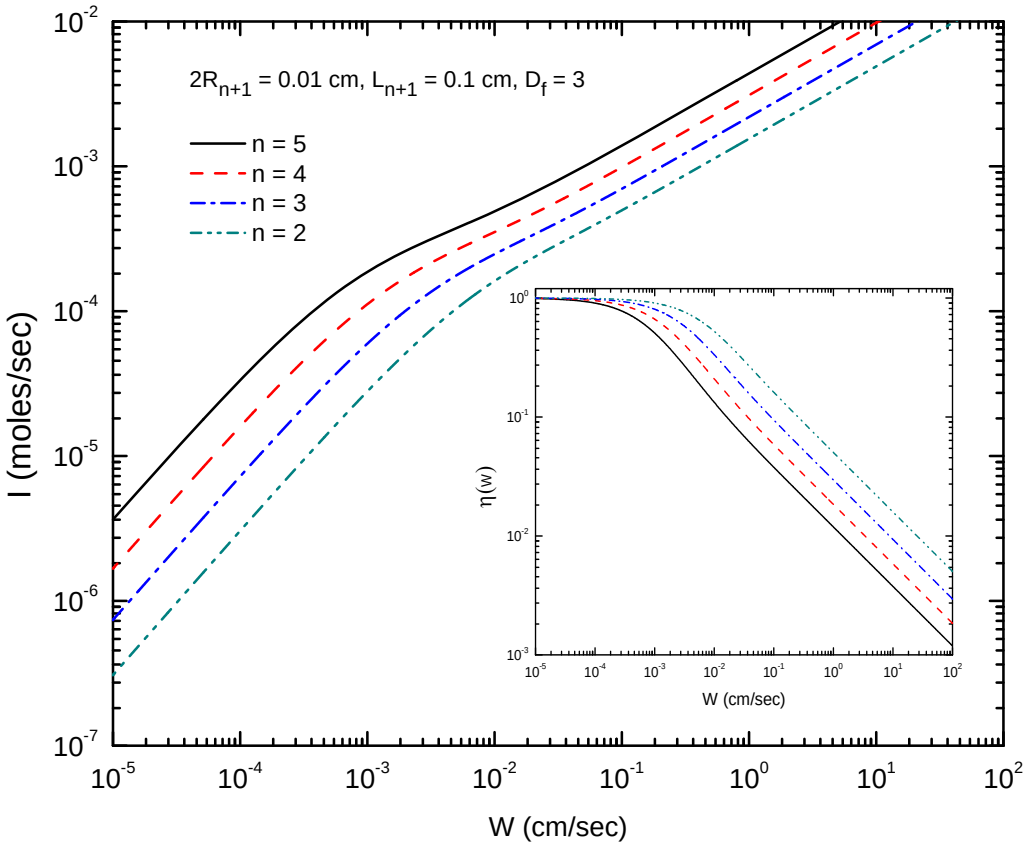

Figure 6.1: Dependence of the oxygen current upon the depth of a space-filling tree with $D_f = 3$, and associated efficiencies (inset).

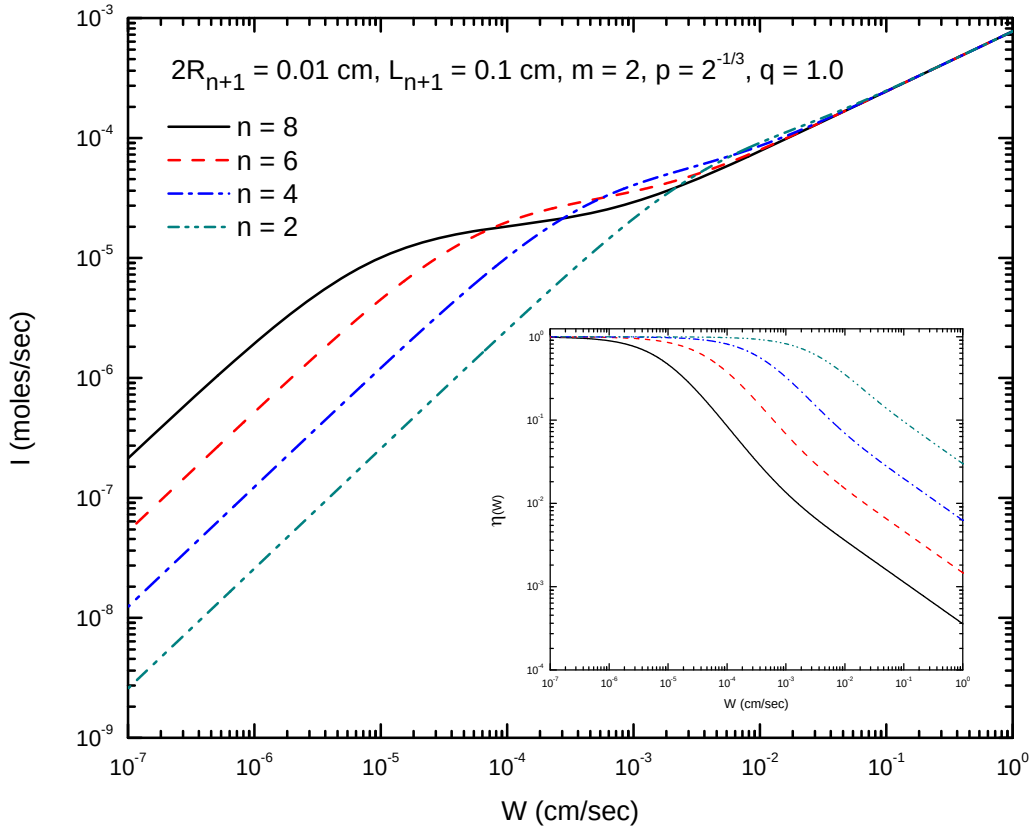

Figure 6.2: Illustration of the convergence in oxygen currents in the limit of large permeability, for a tree in which only the lengths scale to fill space. The associated efficiencies are inset.

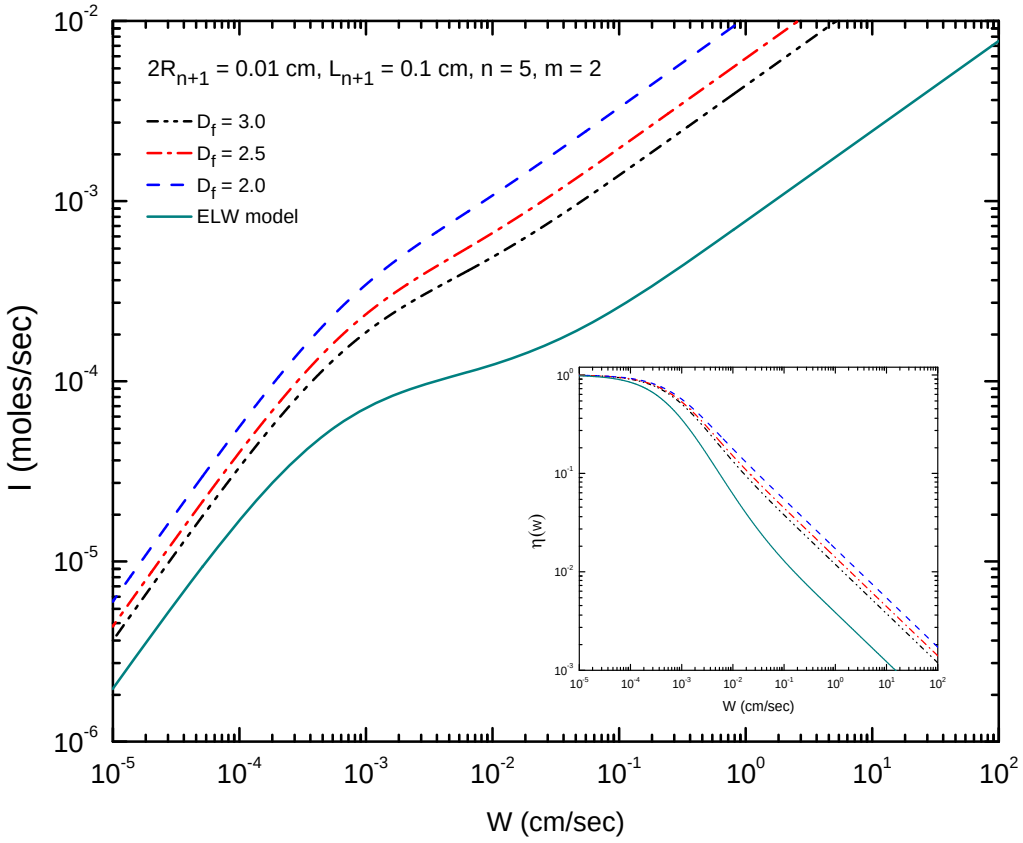

Figure 6.3: Sensitivity of the equiscaled ($p = q$) gas exchanger to its fractal canopy dimension, and comparison to the equi-length and width model (ELW model). Inset are the associated efficiencies.

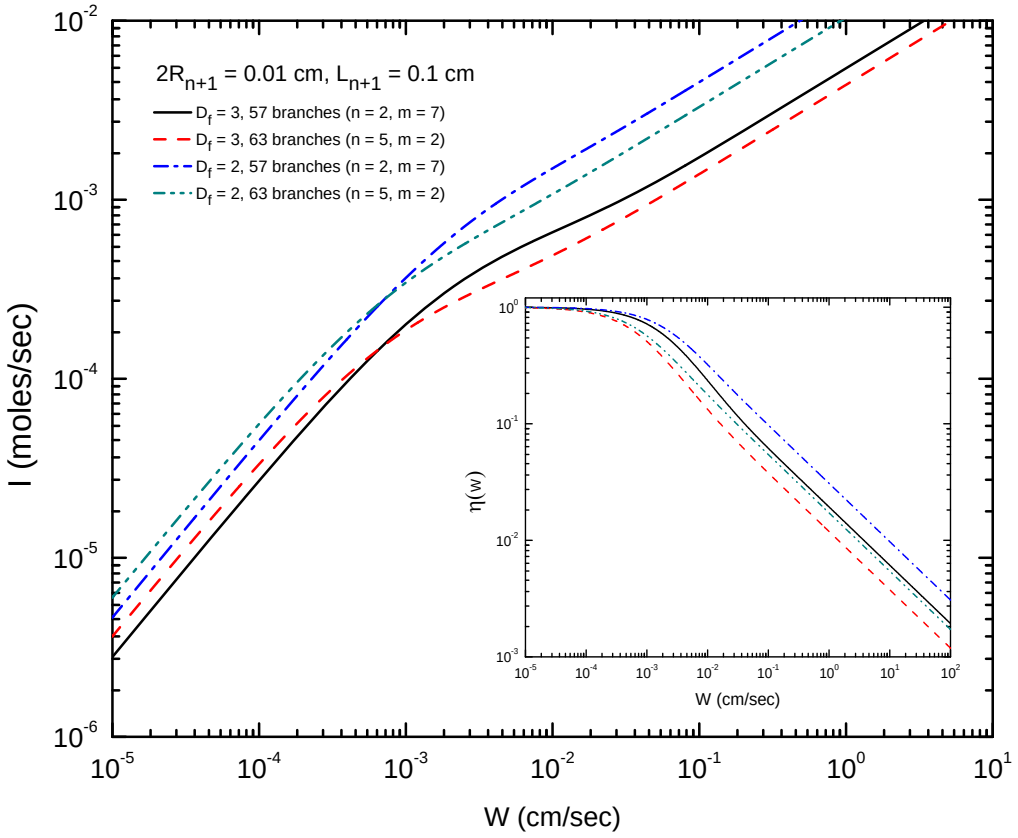

Figure 6.4: Comparison of trees that contain a similar total number of branches, and that contain both planar and space-filling canopies.

Chapter 7

Application of physiological data

7.1 Introduction

Several models of the acinar airways have recently been proposed to describe the gas exchange process within the human lung acinus [6, 9, 10, 1, 11]. In particular, such models have often been used to elucidate bio-inspired engineering strategies, with the assumption that evolutionary development has produced a transport network optimized for the delivery of oxygen to the hemoglobin of the red blood cells within the pulmonary arteries. Such a process is complicated by both fluctuating oxygen demands from the body under widely varying operating conditions, and by the potential for damage to the soft tissues involved in its function.

To study the lung as a gas exchanging mechanism, several authors have proposed model geometries from which to study the connection between the structure of the lung and its function. One of the first studies was a numerical investigation conducted by Sapoval et al. [9], in which they used a finite element method to directly solve the equations of motion for the diffusion-reaction system (see chapter 2) in a model called the "Hilbert acinus." Figure 7.1 provides an illustration of the planar Hilbert acinus. The observation that a "smaller" Hilbert acinus gave a higher transport efficiency was one accomplishment of their numerical study on the Hilbert acinus. They used this result as evidence in support of their hypothesis that the human lung acinus operates under an oxygen screening mechanism

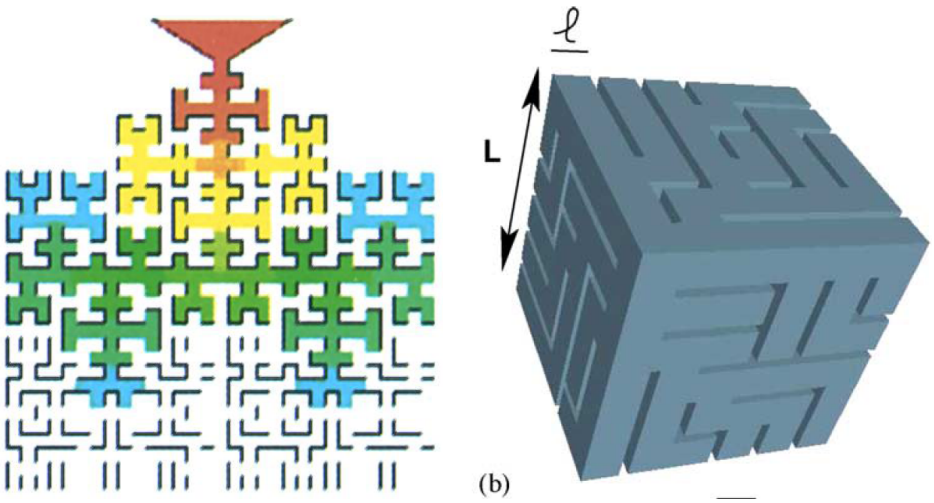

(a) Hilbert acinus.[9] (b) Kitoaka fractal model.[6]

Figure 7.1: Fractal models of a human lung acinus.

known as "diffusional screening."

Shortly thereafter Felici et al.[6] extended this result to space-filling architectures through another numerical study using a fractal model of the lung acinus called the Kitoaka fractal, shown in Figure 7.1. Their motivation for the use of the Kitoaka fractal lay in its remarkable reproduction of the branching structure of the acinar ducts in the lung acinus. They calculated efficiencies from their model, but stopped short of reporting the oxygen currents predicted by their model for the human lung.

To the best of our knowledge, the first analytical model of gas exchange in the human lung was recently proposed by Hou and his collaborators [10, 1]. They developed an algorithm, called the Rope-Walk Algorithm (RWA), which renormalized the alveolar membranes of the lung using a recently discovered interpretation for the transport parameter Λ called the "exploration length" (see chapter 2 for a detailed discussion). They recognized that the exploration length suggested that the equations of motion for oxygen within the airways could be approximated from purely geometrical considerations. Remarkably, their simplified model of gas exchange predicted oxygen currents that very closely matched the best available experimental measurements[1]. Unfortunately, their renormalization treatment neglects such anatomical aspects as acinar branching, and its influence on oxygen transport is presently not well understood. Nevertheless, their success strongly suggests

that the effective surface area of alveolar membranes is a critical aspect of the gas exchange mechanism.

Since the work of Hou et al. one other analytical model of transport has been recently suggested by Grebenkov and his collaborators.[11] Their model discretized an acinar duct, and considers the probability of oxygen absorption at discrete sites along a one-dimensional branching lattice. A triumph of this model has been the analytical description of a branching structure, in which its efficiency depends directly upon structural parameters such as the number of branching generations and daughter branches in the tree. Grebenkov et al. computed the efficiency of their model, yet neglected to apply physiological data from the human lung to their model.

In this chapter we will reproduce and extend several features of the human lung reported by these authors through the application of physiological data to the fractal model of gas exchange developed and reported within chapter 6, from which the equi-length and width model is a special case ($p = q = 1$, or $D_f \to \infty$).

7.2 Exercise and the gas exchange unit

To describe the gas exchange process we adopt a compartmentalized picture of oxygen transport from the acinar gas to the blood, as described by Hou in his PhD thesis [10], and we treat the transport of oxygen as a three-step process: (1) oxygen propagation by diffusion, from the entrance of the acinar gas exchange unit to the surface of the alveolar membranes; (2) oxygen enters the membranes and diffuses through its various layers to emerge within the blood plasma; and (3) oxygen diffuses through the blood plasma and binds exclusively to the hemoglobin of the red blood cells within the pulmonary arteries. A detailed picture of parts (2) and (3) of this transport scheme is outlined in Figure 7.2.

An important aspect of this scheme is that one may extract several pieces of information crucial to our model of gas exchange, without full consideration of the details associated with the transmembrane interactions of oxygen with its environment. As shown in Figure 7.2, we consider the alveolar membranes to be a tissue barrier separating the acinar gas from

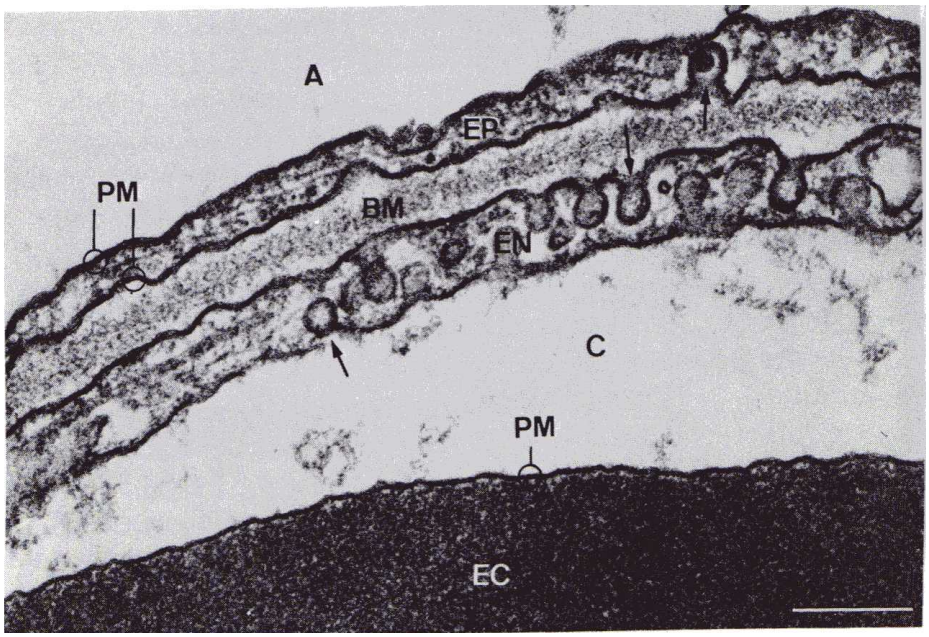

(a) Electron micro graph of alveolar membranes cross section, from [3]. Scale marker is 0.2μm.

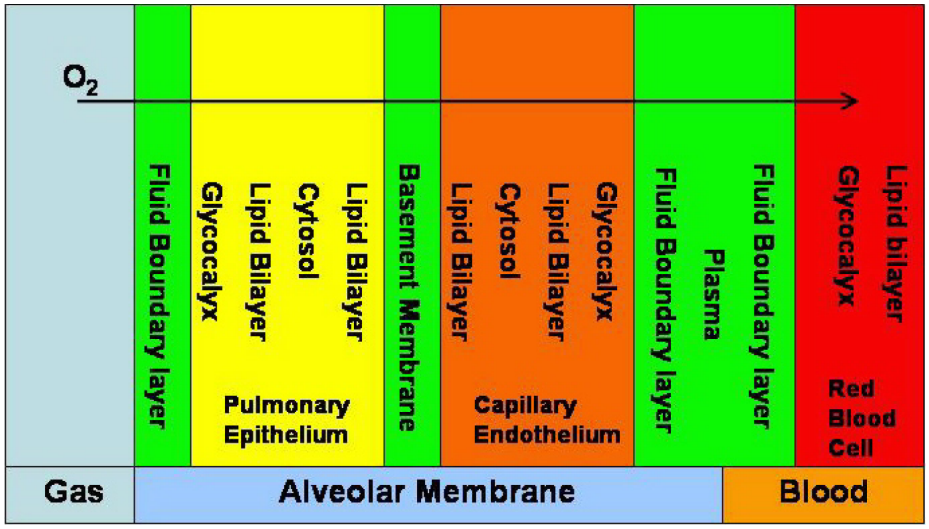

(b) Barriers to oxygen diffusion, from [10]

Figure 7.2: Barriers to oxygen diffusion from the acinar airways to the hemoglobin of the red blood cells.

the blood plasma. We then model the alveolar membranes as two fluid filled compartments: the epithelium (EP) and endothelium (EN), partitioned by the basement membranes (BM). The key hypothesis proposed by Hou, was that these fluid filled cells may effectively be represented as resistors connected in series.

This hypothesis predicts that the transmembrane current is equivalent to the current of oxygen diffusing and binding to the hemoglobin of the red blood cells. As a result, we need only calculate the current resulting from the considerations in (2) above to predict the oxygen generated by the lung and distributed throughout the body. In particular, we make the assumption that the transmembrane flux is proportional to the difference in oxygen concentration between the acinar gas and the blood side of the membranes, $J \propto \Delta C$. We thus consider the details regarding oxygen's interaction and passage across the alveolar membranes to be contained within the constant of proportionality W, called the permeability of the alveolar membranes. The transmembrane oxygen current for the lung may then be written as [1]

$$\begin{aligned} I &= \mathcal{D}_m \left(p_{air} - p_{blood}\right) \\ &= N_g W S_{eff,g} \beta_{air} \left(p_{air} - p_{blood}\right) \\ &= N_g W S_{eff,g} \left(C_{air} - C_{blood} \frac{\beta_{air}}{\beta_{blood}}\right), \end{aligned} \tag{7.2.1a}$$

where N_g is the number of equivalent gas exchangers, W is the global permeability of the alveolar membranes, β_{air} (β_{blood}) is the solubility of oxygen in air (blood), $C_{air} - C_{blood}\beta_{air}/\beta_{blood}$ is the concentration difference between the air and blood sides of the membranes, $p_{air} - p_{blood}$ is the partial pressure difference of oxygen across the membranes, $S_{eff,g}$ is the effective surface area of a single gas exchanger within the lung, and $\mathcal{D}_m$ is the diffusional capacity of the alveolar membranes. These parameters are summarized in Table 7.1.

To apply Equation 7.2.1 to the lung, we must clearly define a gas exchanger in the Cayley tree model, and how it couples with the gas exchange units within the human lung. We have taken the definition of the human lung acinus to be those airways that are exclusively

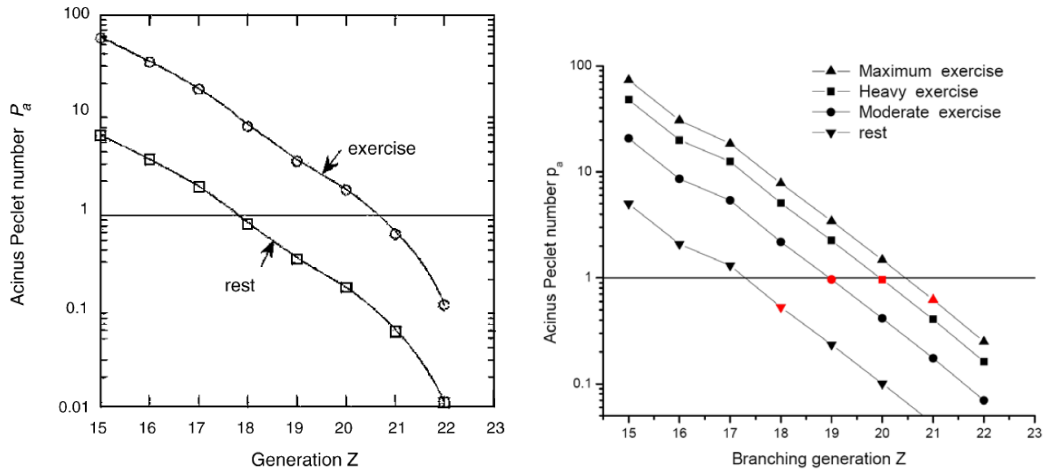

Figure 7.3: Theoretical convection-diffusion transitions computed by (a) Weibel et al. [2], and (b) Hou et al. [1].

alveolated; however, the extent to which those airways are used in gas exchange is defined by the convection-diffusion transition of oxygen. Weibel and his collaborators have introduced a measure of the convection-diffusion transition z_{cd}, called the "acinus Peclet number" [9, 2], and we adopt its definition as

$$P_a := \frac{\text{convective speed of oxygen}}{\text{diffusional speed of oxygen}}; \tag{7.2.2}$$

its intersection, $P_a = 1$, gives the branching generation of the convection-diffusion transition within the lung acinus. Hou and his collaborators have used this definition to predict the branching generation of the convection-diffusion transition for several levels of exercise [1], as shown in Figure 7.3.

We adopt the more recent predictions of Hou et al. for the convection-diffusion transition and we consider the following four regimes of exercise: rest ($z_{cd} = 18$), moderate exercise ($z_{cd} = 19$), heavy exercise ($z_{cd} = 20$), and maximum exercise ($z_{cd} = 21$). The mean value for the total number of branching generations in the lung, from the trachea to the terminal branches of the acinar airways, has been measured to be 23 [4]. Therefore, we define a gas exchanger in the context of the Cayley tree model to be a tree with depth corresponding

Exercise regimes	z_{cd}	Gas exchanger	Depth of Cayley tree
Rest	18	1/8 subacinus	n = 5
Moderate exercise	19	1/16 subacinus	n = 4
Heavy exercise	20	1/32 subacinus	n = 3
Maximum exercise	21	1/64 subacinus	n = 2

Table 7.1: Regimes of exercise as reported by Hou et al. [1].

to the appropriate regime of exercise, the results of which are provided in Table 7.1. We will define a gas exchanger in the Cayley tree to be a tree of depth n, where the depth is restricted by the size of the acinus in the appropriate regime of exercise.

7.3 Methods

In chapter 6 we developed a fractal model of oxygen transport in the lung. We found that the total current crossing the surface for a Cayley tree model of depth n was given by Equation 6.2.3:

$$I = \frac{\pi {R_1}^2 DC_{ent}}{mq^2} \cdot \frac{W_{eff}}{D_{eff}}. \tag{7.3.3}$$

We calculated D_{eff}/W_{eff} using the the Möbius representation of the iterative map $\tilde{f}_k(\Lambda)$ (see Equations 2.2.7 and 2.2.5), where the matrix is given by

$$F_{ij}^{(k)} = \begin{pmatrix} q^{-2}\sqrt{\frac{2}{R_1\Lambda}} & q^{\frac{k-5}{2}} \tanh\left(\sqrt{\frac{2{L_1}^2}{R_1\Lambda}}(\frac{p}{\sqrt{q}})^{k-1}\right) \\ q^{\frac{1-k}{2}}\frac{2m}{R_1\Lambda}\tanh\left(\sqrt{\frac{2{L_1}^2}{R_1\Lambda}}(\frac{p}{\sqrt{q}})^{k-1}\right) & m\sqrt{\frac{2}{R_1\Lambda}} \end{pmatrix}, \tag{7.3.4}$$

for a Cayley tree in which $p = {p^{(i)}}_k$ and $q = {q^{(i)}}_k \; \forall \quad i = 1, 2, \ldots, m$ and $k = 1, 2, \ldots, n$. In other words, the daughter branches extending from a parent branch, across a given branch generation k, are all equivalent in width and length.

The products of this matrix are then computed and applied to a column vector within the vector space $\mathbb{C} \times \mathbb{C}$, and the result yields a rotated vector whose entries may be used to

compute an effective exploration length D_{eff}/W_{eff}, for the tree:

$$\prod_{k=1}^{n+1} F_{ij}^{(k)} \cdot \begin{pmatrix} D \\ W \end{pmatrix} = \begin{pmatrix} D_{eff} \\ W_{eff} \end{pmatrix}. \tag{7.3.5}$$

7.3.1 Geometry of the Cayley tree

To apply restrictions on input data, we will need to quantify several geometrical aspects of the Cayley tree. Here we report several of the results obtained in chapter 5 of this thesis.

Consider a Cayley tree for which $p = p^{(i)}{}_{k+1}$ and $q = q^{(i)}{}_{k+1}$ for all $i = 1, 2, \ldots, m$ and $k = 1, 2, \ldots, n$, and let the tree be equiscaled such that the scaling ratios satisfy $p = q$ (equivalently, $D_{tree} = D_f$). Then we have

$$V_{tree} = \pi {R_1}^2 L_1 \sum_{k=0}^{n} \left(mq^2 p\right)^k, \tag{7.3.6a}$$

$$S_{tree} = 2\pi R_1 L_1 \sum_{k=0}^{n} \left(mpq\right)^k + \pi {R_1}^2 \left(mq^2\right)^n, \tag{7.3.6b}$$

$$L_p = L_1 \sum_{k=0}^{n} \left(p\right)^k. \tag{7.3.6c}$$

For these trees, one may express these results in terms of properties of the terminal branches of the tree through the relations $R_{n+1}/R_1 = q^n$, and $L_{n+1}/L_1 = p^n$.

7.3.2 Oxygen current

Here we describe the oxygen current crossing the surface of the Cayley tree model, by rewriting Equation 7.3.3 in the form of Equation 7.2.1:

$$\begin{aligned} N_g I &= N_g W C_{ent} \cdot \frac{\pi {R_1}^2 \Lambda}{mq^2} \cdot \frac{W_{eff}}{D_{eff}} \\ &= N_g W \left(C_{air} - C_{blood}\frac{\beta_{air}}{\beta_{blood}}\right) \cdot \underbrace{\frac{C_{ent}}{\left(C_{air} - C_{blood}\frac{\beta_{air}}{\beta_{blood}}\right)} \cdot \frac{D}{D_{eff}} \cdot \frac{W_{eff}}{W} \cdot \frac{\pi {R_1}^2}{mq^2}}_{S_{eff,g}}, \end{aligned} \tag{7.3.7a}$$

where we have taken the current given by the tree (Equation 7.3.3) to be that from a single gas exchanger for the lung.

In the reaction-controlled limit ($W \to 0$), Equation 7.3.3 gives $I = WS_{tree}C_{ent}$, where C_{ent} is the concentration difference between the entrance of the tree (source) and the exterior side of the tree surface (receptor). For the reaction-controlled current, C_{ent} is also the concentration difference across the tree surface, because the concentration gradient is uniform throughout the tree.

In Equation 3.4.23 we have shown that the general solution of the equations of motion has the functional form $I = WS_{eff}C_{ent}$, from which we identified S_{eff} as the effective surface area of the tree surface used in particle transport. In this form, the reaction-controlled limit gives $\lim_{W\to 0} S_{eff}\,(D/W) = S_{tree}$. Since C_{ent} is independent of W, we may take C_{ent} to be the concentration difference across the tree surface. Therefore C_{ent} = concentration difference between the tree entrance and the exterior side of the surface = concentration across the tree surface, for all W. This picture holds for the physiological data and we make the identification: $C_{ent} = C_{air} - C_{blood}\,(\beta_{air}/\beta_{blood})$. The final expression for the transmembrane oxygen current is given by

$$I_{lung} = N_g W S_{eff,g}\left(C_{air} - C_{blood}\frac{\beta_{air}}{\beta_{blood}}\right), \tag{7.3.8}$$

where

$$S_{eff,g} = \frac{D}{D_{eff}} \cdot \frac{W_{eff}}{W} \cdot \frac{\pi {R_1}^2}{mq^2}. \tag{7.3.9}$$

7.3.3 Pulmonary efficiency

An important effort in respiratory physiology is the prediction of the pulmonary efficiency of the human lung, η. We will therefore compute the efficiency of the gas exchanger in our model tree from the definition given in Equation 4.3.19. From this expression, it follows that the model efficiency may be computed by use of its effective surface area:

$$\eta_{tree} = \frac{S_{eff,g}}{S_{tree}}, \tag{7.3.10}$$

where $S_{eff,g}$ is obtained from Equation 7.3.9, and S_{tree} is given by Equation 7.3.6.

7.4 Physiological data

7.4.1 Estimation of geometric data from the resting value

Table 7.2 reports empirical data for several of the parameters needed to compute predictions of the oxygen current reaching the red blood cells of the pulmonary arteries of the lung. We inferred these physiological values from ref. [2] in the following way. As an example, we illustrate how we inferred the volume of the gas exchanger V_g, and our relevant assumptions. We took the volume of an acinus, as reported in ref. [2], to be $V_{acinus} = 0.187$ cm^3. We have assumed a gas exchange unit at rest ($n = 5$) to be a "1/8 subacinus" and took $V_g = 0.187/8$ cm^3. This procedure neglects the surface area in the first two generations of the acinus, however we note that these first generations are composed of the respiratory bronchioles in the acinus and are therefore not exclusively alveolated–minimizing their participation in gas exchange.

Let $V_{g,regime}$ be the volume of a gas exchanger in the associated regime of exercise (rest, moderate, heavy, or maximum). To infer the data for $V_{g,regime}$, we began by taking $V_{g,moderate} = V_{g,rest}/2$ under the assumption that the vast majority of acinar volume is given by the last generation of branching within the tree. A single acinar branch is neglected in the estimate $V_{g,rest}/2$, and is assumed to make a trivial contribution to $V_{g,moderate}$. We estimated the values for the remaining regimes of exercise as follows: $V_{g,heavy} = V_{g,moderate}/2$, $V_{g,max} = V_{g,heavy}/2$.

How good are these estimates? Using the Cayley tree as a model of the acinar airways, we can estimate the contribution of the neglected branches to the volume (or surface area) of the gas exchanger in the associated exercise regime. The hypothesis we wish to test is: $V_{g,moderate} = 0.5 \cdot V_{g,rest}$. From Equation 7.3.6, we find for the equi-length and width Cayley tree model ($p = q = 1$):

$$\frac{V_{tree,moderate}}{V_{tree,rest}} = \frac{\left(mq^2p\right)^5 - 1}{\left(mq^2p\right)^6 - 1} \approx 0.492, \tag{7.4.11}$$

and is very close to the value of 0.5 predicted from our hypothesis. We computed these volumes for the remaining regimes of exercise and found: $V_{g,heavy} = 0.484 \cdot V_{g,moderate}$, and $V_{g,maximum} = 0.467 \cdot V_{g,heavy}$. We conclude, to very good approximation, that the volume of successive lung subacini is given by half the value of the previous one. In the equi-length and width model, these results extend to the surface area of successive gas exchangers within the Cayley tree model of the lung acinus. Therefore, in the equi-length and width Cayley tree model of the human lung acinus, we may reasonably consider the lung acinus to be a hierarchical composition of gas exchangers while safely neglecting the geometric contributions from the complement of the intersection between a parent and daughter gas exchanger.

For a fractal tree the situation is quite different. For an equiscaled Cayley tree ($p = q$) with canopy dimension $D_f = 3$, one can show by using Equation 7.3.6, that $V_{tree,moderate} \approx 0.417 \cdot V_{tree,rest}$, $V_{tree,heavy} = 0.400 \cdot V_{tree,moderate}$, and $V_{tree,maximum} \approx 0.375 \cdot V_{tree,heavy}$. We can conclude from this analysis that the volume of successive gas exchangers is not well approximated as one half the volume of the parent gas exchanger.

Similar results may be computed connecting the surface area of successive gas exchangers within an equiscaled tree with $D_f = 3$, and in such a tree we conclude that the surface area of successive gas exchangers is not well approximated as one half of the parent one.

7.4.2 Width and length of the terminal branches

To choose the width and length of the terminal branches we need two equations that place restrictions on $2R_{n+1}$ and L_{n+1} (or equivalently, R_1 and L_1 in an equiscaled tree). These equations are given by geometrical restrictions on a gas exchanger, in that we restrict its volume V_g, surface area S_g, and longitudinal path length L_p to be the physiological values reported in Table 7.2 at rest. We make the following restrictions on Equations 7.3.6 so that we may identify appropriate choices for $2R_{n+1}$ and L_{n+1}:

Item (1): $S_g = 6.75$ cm^2, $V_g = 0.0234$ cm^3,

Item (2): $S_g = 6.75$ cm^2, $L_p = 0.456$ cm,

Description	**Symbol**	**Unit**	**Value** Exercise regime			
			Rest	Moderate	Heavy	Maximum
Global permeability of the alveolar membranes of the human lung	W	cm/sec	0.00739	0.00739	0.00739	0.00739
Coefficient of diffusion for O_2 within acinar gas	D	cm^2/sec	0.243	0.243	0.243	0.243
Concentration difference across the alveolar membranes of the human lung	$C_{air} - C_{blood}\frac{\beta_{air}}{\beta_{blood}}$	$\times 10^{-7}$ moles/cm^3	1.97	4.10	4.97	4.51
Number of gas exchangers in the human lung	N_g	$\times 10^5$	1.81	3.63	7.26	1.45
Volume of a single gas exchanger	V_g	cm^3	0.0234	0.0117	0.00584	0.00292
Surface area of a single gas exchanger	S_g	cm^2	6.75	3.36	1.69	0.844
Longitudinal path length of a single gas exchanger	L_p	cm	0.456	0.363	0.280	0.210

Table 7.2: Measured data relevant to the Cayley tree model, compiled and reported by Hou et al. [1]. Gas exchanger volume, V_g, surface area, S_g, and longitudinal path length, L_p, was estimated from experimental data reported within ref. [2].

$p = q = 1, D_f \to \infty$					
Item	Restrictions			Result	
	V_g (cm^3)	S_g (cm^2)	L_p (cm)	$2R_{n+1}$ (cm)	L_{n+1} (cm)
(1)	0.0234	6.75	–	0.0139 0.511	2.46 0.00181
(2)	–	6.75	0.456	0.299	0.076
(3)	0.0234	–	0.456	0.0788	0.076
(4)	–	–	0.456	0.0139	0.076
$p = q = 2^{-1/3}, D_f = 3$					
(1)	0.0234	6.75	–	0.00840 0.514	2.20 0.000587
(2)	–	6.75	0.456	0.305	0.0395
(3)	0.0234	–	0.456	0.0626	0.0395
(4)	–	–	0.456	0.0139	0.0395

Table 7.3: Results for the width and length of the terminal branches from geometrical constraints listed in Items (1) through (4), at rest. V_g, S_g, and L_p are the volume, surface area, and longitudinal path length of a single gas exchanger in the human lung, respectively.

Item (3): $V_g = 0.0234$ cm^3, $L_p = 0.456$ cm.

We will then use these widths and lengths to predict both the transmembrane oxygen current and the pulmonary efficiency of the human lung, under the assumption that the size of the terminal branches remains constant across all regimes of exercise.

Aside from the purely geometrical restrictions represented by Items (1) through (3) above, one may take another path in the identification of the width and length of the terminal branches for the tree. In this item, called Item (4), we make choices for physiological data based upon the best known estimates of an alveolar diameter and we use the longitudinal path length to restrict the length of a terminal duct. Using the longitudinal path length is advantageous because it is independent of the width $2R_{n+1}$. We take the width of an alveolus to be that given by Hou and his collaborators [1], as $2R_{n+1} = 0.0139$ cm.

The choice of L_{n+1} depends upon the geometry of the tree; however, in any geometry we take the longitudinal path length to be $L_p = 0.456$ cm. Together, we have

Item (4): $2R_{n+1} = 0.0139$ cm, $L_p = 0.456$ cm.

The results of the restrictions outlined in Items (1), (2), (3) and (4) are tabulated in Table 7.3.

7.4.3 Preference for the equi-length and width model

Figure 7.4 reports experimental data for the widths and lengths of the acinar ducts as reported by Haefeli-Bleuer and Weibel[4]. In this figure, the generations of ducts are counted along the horizontal axis. Haefeli-Bleuer and Weibel reported that the mean number of these generations in the lung was 23[4], suggesting that a gas exchanger with a size corresponding to 1/8 of an acinus would begin at generation 6 along the horizontal axis of Figure 7.4.

The mean duct lengths, mean outer diameters, and mean inner diameters appear to be well approximated by a linear function with slope near zero. Figure 7.4 also shows that the scaling ratios across generations are very close to 1 (within approximately 5%) for both the diameters and length of the ducts, which strongly suggests that these may be considered constant across all branch generations within the acinar airways. We will therefore give preference to the equi-length and width model, in which the acinar branches are modeled by the scaling ratios $p = q = 1$.

From Figure 7.4, we may also compute the approximate mean values of the widths and lengths of the ducts from the data within ref. [4]. The mean of the duct lengths was found to be 698 μm, while that of the outer diameters was 686 μm, while we found the mean of the inner diameters to be 311 μm. Hou et al. [1] estimated the diameter of an alveolus to be approximately 139 μm, which is approximately half of the mean inner diameter as measured by Haefeli-Bleuer and Weibel in ref. [4]. Weibel et al.[2] has since reported that Haefeli-Bleuer and Weibel provided overestimates of at least one structural parameter in their data; however, it is unclear whether other structural data for the airway ducts were also overestimated, as Hou's estimate for an alveolar diameter would seem to suggest.

7.5 Results

We conducted a study of the Cayley tree model under various levels of exercise and under several physiological choices for the scaling across branch generations in the tree. Specifically, we chose an equiscaled tree with fractal canopy dimensions $D_f \to \infty$, and $D_f = 3$; the use of the equi-length and width model was justified through experimental data provided in

reference [4]. We applied an algorithm given by the flow chart within Figure 1.1, to make predictions for both the oxygen current reaching the blood and the pulmonary efficiency of the gas exchanger.

A surprising result, reflected in Table 7.3, is the existence of non-unique solutions for the width and length of the terminal branches associated with the restriction of the model surface area and volume, described by Item (1) in our geometrical restrictions. Both choices for width and length give Cayley trees that give equivalent geometry and are self consistent (see Table 7.4); however, they correspond to trees that are qualitatively very different.

Analyzing these two different choices for the widths and lengths of the terminal branches shows that the tree with smaller width ($2R_{n+1} = 0.0139$ cm) vastly underestimates both the oxygen current and the pulmonary efficiency of the lung; whereas, the tree with much larger width ($2R_{n+1} = 0.511$ cm) overestimates these quantities. This is expected, as the current is directly proportional to the width of the entrance branch in the tree. Surprisingly, these two trees give very different efficiencies, even though they are restricted to have the same total surface area.

In Table 7.6 we have tabulated results from the equi-length and width model, given the experimental data presented within Table 7.2 and the choices for the width and length of the terminal branches derived from the geometrical restrictions presented within Table 7.3. In all cases, we find that the choice of width and length that is derived from strictly geometrical restrictions on the Cayley tree gave predictions that were different from those quantities given by the experimental data. Surprisingly, the predictions of the oxygen current from Item (3), in which the volume and longitudinal path length of the model are restricted to those of the 1/8 acinus, are much closer to the experimental data than those predictions made from Items (1) and (2).

We note that alveolar surfactant plays a critical role in the global mechanical stability of the alveolar network, and errors in its production can lead to serious complications, including respiratory distress in infants[3]. The volume of the acinar airways is regulated by alveolar surfactant, and it is interesting that restricting the volume of the airways in Item (3) to be the physiological value, leads to a much closer prediction of the current and

efficiency would than other choices. This is surprising because we expect the surface area of the gas exchanger to be the geometrical property that is the most important for oxygen transport.

We find the model with width and length that are given by Item (4) greatly underestimates the oxygen current in all regimes of exercise. At rest, this model predicts $I_{lung} = 8.81 \times 10^{-6}$ moles/sec, while the experimental data reported by Hou et al. is $I_{lung} = 2.01 \times 10^{-4}$ moles/sec[1]. Such a significant underestimate by the model is expected, because the current is proportional to the surface area used in transport. Here the model underestimates surface area of the gas exchanger by a factor of approximately 31, and we thus expect the current to be similarly underestimated.

In contrast, we find that the pulmonary efficiency of the model Item (4) makes predictions very close to those given by the experimental data for the pulmonary efficiency (see Table 7.6). In Figure 7.6 we show the pulmonary efficiencies for this model over a wide range of permeability, overlayed with the experimental data. It is clear that even though the model produces a current that is very close to the experimental value at rest, it diverges from the experimental values in exercise.

Figure 7.6 shows the efficiencies, in all regimes of exercise, for the model with the physiological parameters of Item (4). It is clear from this figure that all regimes of exercise give good agreement with the experimental data for $\Lambda = 32.8$ cm. We conclude that maximum exercise yields the most efficient gas exchanger for the human lung. Interestingly enough, even though the currents from Item (4) are not close to the experimental ones, the factor by which they scale up through exercise regimes are very similar to the experimental data.

Even more striking, is that the ratio between the currents in Item (4) is approximately constant across the following three exercise regimes: $I_{rest,exp}/I_{rest,theory} = 22.8$, $I_{moderate,experiment}/I_{moderate,theory} = 29.2$, and $I_{heavy,experiment}/I_{heavy,theory} = 27.4$. In maximum exercise we find $I_{max,experiment}/I_{max,theory} = 49.9$. The arithmetic mean for all

regimes of exercise is given by

$$< \frac{I_{experiment}}{I_{lung}} >= 32.3. \tag{7.5.12}$$

These results hint that there may be an unknown proportionality factor connecting these two quantities.

Some authors[5, 6, 2] claim that the computed efficiency from a model may be coupled with the oxygen current binding to the blood within the pulmonary arteries through the following expression: $I = W\eta S_{lung}\,(C_{air} - C_{blood}\beta_{air}/\beta_{blood})$, where η should be computed in whatever model geometry is being considered, and $S_{lung} = 122$ m^2.[2, 1] If we compute η from the Cayley tree model, we have

$$I = W \underbrace{\eta_{tree} S_{lung}}_{S_{eff,lung}} (C_{air} - C_{blood}\beta_{air}/\beta_{blood})\,. \tag{7.5.13}$$

The Cayley tree model computes the current crossing its surface; thus we have, from Equation 7.3.8, $I_{lung} = WN_g S_{eff,g}\,(C_{air} - C_{blood}\beta_{air}/\beta_{blood})$. Dividing Equation 7.5.13 by this expression, we find a relationship between the two under physiolgical conditions ($\Lambda = 32.8$ cm):

$$\frac{I}{I_{lung}} = \frac{S_g}{S_{tree}}, \tag{7.5.14}$$

where S_g is obtained from Table 7.2, for the appropriate regime of exercise. Here $\eta S_{tree} = S_{eff,g}$, and S_{tree} is given by Equation 7.3.6. Computing these ratios from Equation 7.5.14 and the data given within Table 7.4, we find the arithmetic mean throughout all regimes of exercise to be

$$< \frac{I}{I_{lung}} >= 32.7 \tag{7.5.15}$$

for the equi-length and width model. In comparison with Equation 7.5.12, we find good agreement and conjecture that the use of the model's pulmonary efficiency η_{tree}, may be the source of the proportionality discrepency between the experimental and theoretical currents given by Equation 7.5.12.

In Figure 7.7 we used Equation 7.5.13 to compute the oxygen current by using the efficiency predicted by the Cayley tree with width and length given by Item (4). Remarkably, the use of Equation 7.5.13 to infer the oxygen currents gives very good agreement with the experimental data. Equation 7.5.14 gives a relationship between the current generated by the Cayley tree model using experimental input, I_{lung}, and a current generated using its efficiency, I.

If the Cayley tree model were to give currents equivalent to that of Equation 7.5.13, then $I = I_{lung}$ implies that $S_{tree} = S_g$. In other words, the surface area of the Cayley tree must be set to the experimental value of a single gas exchanger in the lung. We have done exactly this for Items (1) and (2); however, we found poor agreement with the experimental data. This is due to the fact that one must vary the width and/or length of the branches in the model to achieve a change in surface area, and a change in these parameters directly affects the current predicted by the model.

In Figure 7.8, we used the treatment given by Equation 7.5.13 to generate predictions for the oxygen current in a lung with space-filling canopy. We found that the currents are reasonably close to the experimental ones, however, homeostasis of the oxygen current is lost as a consequence of reduced surface area associated with such scaling across branches.

As a final remark, we computed the ratio between oxygen currents at rest with fractal canopy $D_f = 2$, and $D_f = 3$. We called these currents $I_{lung,D_f=2}$, and $I_{lung,D_f=3}$, respectively. Using the experimental data given in Table 7.2 for a gas exchanger at rest, and a width and length of $2R_{n+1} = 0.0139$ cm and $L_{n+1} = 0.076$ cm, we found that $I_{lung,D_f=3}/I_{lung,D_f=2} = 0.498$.

Hou et al. conducted a similar calculation[1]; however, they computed the oxygen current in a planar Sierpinski fractal model and compared this result to a fully space-filling Sierpinski model using their analytical renormalization approach. They found that $I_{3D}/I_{2D} = 1.38 \times 10^4$.[1] Our approach is different, as the diffusion of oxygen always occurs in a space with dimension three and is not restricted to a plane, even with a planar canopy of $D_f = 2$.

7.6 Summary and conclusions

We applied the best available estimates for the transport and structural parameters to the Cayley tree model for both space-filling ($D_f = 3$) and and overfilling ($D_f \to \infty$) cases. We applied the experimental data to our model, and we made choices for the width and length of a terminal branch under several geometrical restrictions provided in Items (1) through (4).

We computed both the oxygen current binding to the hemoglobin of the red blood cells, and the pulmonary efficiency of a gas exchanger at various levels of respiratory exercise. From a comparison between our theoretical predictions and the experimental data, we found that none of our models produced predictions close to the experimental currents throughout all four regimes of exercise. We found, however, that several of the models provided estimates close to experimental data for only one or two regimes of exercise; this data was presented in Tables 7.6, and 7.7.

We concentrated our analysis on the predictions made using restrictions on the width and length of the terminal branches, outlined in Items (3) and (4). We noticed that Item (3) gave good agreement for the oxygen current at rest, while its predictions for the pulmonary efficiency were poor. Conversely, Item (4) gave a poor prediction for the oxygen current; however, its prediction for the pulmonary efficiency was very good.

We analyzed the efficiency of the model predicted by Item (4) in further detail by computing oxygen currents using the model as outlined in a method presented by other authors. Under this treatment, the efficiency of the model tree is hypothesized to be equivalent to the efficiency of the human lung. For example, if the model uses 10% of its surface area in transport, then this treatment would make the assumption that the human lung does so as well. Such a treatment washes away the differences between models, and one would seem to prefer models that make accurate predictions for the pulmonary efficiencies, regardless of their structure or origin.

Remarkably, we found that this treatment produced predictions of the oxygen current that were very close to the experimental ones–a fact reflected in its close agreement with the experimental pulmonary efficiencies. Since the Cayley tree model generates oxygen current

directly, without needing to resort to using its efficiency and an auxiliary hypothesis to infer the currents, we should naturally question the validity of such a treatment. Nevertheless, its close agreement with the experimental data suggests that the efficiency of the model, as a measure of the surface area which is active in oxygen transport, should be preferred as a calculational and predictive tool. For this reason, we elevate the model given by Item (4) to a preferred status.

Indeed, respiratory physiologists often wish to obtain the diffusional capacity of the alveolar membranes $\mathcal{D}_m$, from which the total oxygen current can be inferred from the partial pressure across them by $I = \mathcal{D}_m \left(p_{air} - p_{blood}\right)$. Thus, by computing the oxygen current in the Cayley tree model we make predictions for the pulmonary efficiency and the diffusional capacity of the alveolar membranes.

Equi-length and width model ($p = q = 1$, $D_f \to \infty$)								
REST								
Item	Parameters (cm)		V_g (cm^3)		S_g (cm^2)		L_p (cm)	
	$2R_{n+1}$	L_{n+1}	Th.	Exp.	Th.	Exp.	Th.	Exp.
(1)	0.0139 0.511	2.46 0.00181	0.0235 0.0234	0.0234	6.77 6.75	6.75	14.8 0.011	0.456
(2)	0.299	0.076	0.336	0.234	6.74	6.75	0.456	0.456
(3)	0.0788	0.076	0.0234	0.234	1.34	6.75	0.456	0.456
(4)	0.0139	0.076	0.000727	0.234	0.214	6.75	0.456	0.456
MODERATE EXERCISE								
(1)	0.0139 0.511	2.46 0.00181	0.0116 0.0115	0.0117	3.33 3.37	3.38	12.3 0.0091	0.363
(2)	0.299	0.076	0.165	0.0117	3.34	3.38	0.38	0.363
(3)	0.0788	0.076	0.0115	0.0117	0.661	3.38	0.38	0.363
(4)	0.0139	0.076	0.000358	0.0117	0.105	3.38	0.38	0.363
HEAVY EXERCISE								
(1)	0.0139 0.511	2.46 0.00181	0.0056 0.00557	0.00584	1.61 1.68	1.69	9.84 0.00724	0.28
(2)	0.299	0.076	0.0800	0.00584	1.64	1.69	0.304	0.28
(3)	0.0788	0.076	0.00556	0.00584	0.321	1.69	0.304	0.28
(4)	0.0139	0.076	0.000173	0.00584	0.0510	1.69	0.304	0.28
MAXIMUM EXERCISE								
(1)	0.0139 0.511	2.46 0.00181	0.00261 0.00260	0.00292	0.753 0.841	0.844	7.38 0.00543	0.21
(2)	0.299	0.076	0.0374	0.00292	0.781	0.844	0.228	0.21
(3)	0.0788	0.076	0.00260	0.00292	0.151	0.844	0.228	0.21
(4)	0.0139	0.076	0.0000807	0.00292	0.0238	0.844	0.228	0.21

Table 7.4: Tabulation of theoretical and experimental values for the geometry of the equi-length and width Cayley tree model ($D_f \to \infty$). Experimental values were inferred from data within reference [2].

Fractal model ($p = q = 2^{-1/3}$, $D_f = 3$)								
REST								
Item	Parameters (cm)		V_g (cm^3)		S_g (cm^2)		L_p (cm)	
	$2R_{n+1}$	L_{n+1}	Th.	Exp.	Th.	Exp.	Th.	Exp.
(1)	0.00840 0.514	2.20 0.000587	0.0234 0.0234	0.0234	6.76 6.75	6.75	25.4 0.00678	0.456
(2)	0.305	0.0395	0.554	0.234	6.74	6.75	0.456	0.456
(3)	0.0626	0.0395	0.0233	0.234	1.00	6.75	0.456	0.456
(4)	0.0139	0.0395	0.00115	0.234	0.206	6.75	0.456	0.456
MODERATE EXERCISE								
(1)	0.00840 0.514	2.20 0.000587	0.00975 0.00974	0.0117	3.09 3.38	3.38	18.4 0.00491	0.363
(2)	0.305	0.0395	0.231	0.0117	3.18	3.38	0.331	0.363
(3)	0.0626	0.0395	0.00973	0.0117	0.462	3.38	0.331	0.363
(4)	0.0139	0.0395	0.000480	0.0117	0.0940	3.38	0.331	0.363
HEAVY EXERCISE								
(1)	0.00840 0.514	2.20 0.000587	0.00390 0.00390	0.00584	1.34 1.68	1.69	12.9 0.00343	0.28
(2)	0.305	0.0395	0.0923	0.00584	1.47	1.69	0.231	0.28
(3)	0.0626	0.0395	0.00389	0.00584	0.206	1.69	0.231	0.28
(4)	0.0139	0.0395	0.000192	0.00584	0.0416	1.69	0.231	0.28
MAXIMUM EXERCISE								
(1)	0.00840 0.514	2.20 0.000587	0.00146 0.00146	0.00292	0.563 0.839	0.844	8.46 0.00226	0.21
(2)	0.305	0.0395	0.0346	0.00292	0.659	0.844	0.152	0.21
(3)	0.0626	0.0395	0.00146	0.00292	0.876	0.844	0.152	0.21
(4)	0.0139	0.0395	0.0000719	0.00292	0.0173	0.844	0.152	0.21

Table 7.5: Tabulation of theoretical and experimental values for the geometry of an equiscaled Cayley tree model with $D_f = 3$. Experimental values were inferred from data within reference [2].

Equi-length and width model ($p = q = 1$, $D_f \to \infty$)						
REST						
	Parameters		I_{lung} (10^{-4} moles/sec)		η (%)	
Item	$2R_{n+1}$ (cm)	L_{n+1} (cm)	Theory	Experiment	Theory	Experiment
(1)	0.0139 0.511	2.46 0.00181	0.0389 17.8	2.01	0.217 99.6	11
(2)	0.299	0.076	12.7	2.01	71.1	11
(3)	0.0788	0.076	1.66	2.01	46.9	11
(4)	0.0139	0.076	0.0881	2.01	15.6	11
MODERATE EXERCISE						
(1)	0.0139 0.511	2.46 0.00181	0.163 37.1	9.68	0.442 99.8	26
(2)	0.299	0.076	30.9	9.68	84.1	26
(3)	0.0788	0.076	4.80	9.68	65.9	26
(4)	0.0139	0.076	0.332	9.68	28.6	26
HEAVY EXERCISE						
(1)	0.0139 0.511	2.46 0.00181	0.394 45.0	18.0	0.914 99.9	40
(2)	0.299	0.076	40.2	18.0	92.3	40
(3)	0.0788	0.076	7.02	18.0	81.7	40
(4)	0.0139	0.076	0.657	18.0	48.2	40
MAXIMUM EXERCISE						
(1)	0.0139 0.511	2.46 0.00181	0.714 40.7	40.9	1.96 100	100
(2)	0.299	0.076	36.6	40.9	96.7	100
(3)	0.0788	0.076	6.74	40.9	92.1	100
(4)	0.0139	0.076	0.819	40.9	70.9	100

Table 7.6: Predictions for the oxygen current and pulmonary efficiency given by the equi-length and width Cayley tree model in all regimes of exercise. Experimental data used for comparison reported by Hou et al. [1].

Fractal model ($p = q = 2^{-1/3}$, $D_f = 3$)						
REST						
	Parameters		I_{lung} (10^{-4} moles/sec)		η (%)	
Item	$2R_{n+1}$ (cm)	L_{n+1} (cm)	Theory	Experiment	Theory	Experiment
(1)	0.00840 0.514	2.20 0.000587	0.103 17.8	2.01	0.580 100.0	11
(2)	0.305	0.0395	16.7	2.01	93.7	11
(3)	0.0626	0.0395	2.18	2.01	82.3	11
(4)	0.0139	0.0395	0.296	2.01	54.5	11
MODERATE EXERCISE						
(1)	0.00840 0.514	2.20 0.000587	0.305 37.2	9.68	0.898 100.0	26
(2)	0.305	0.0395	33.8	9.68	96.4	26
(3)	0.0626	0.0395	4.58	9.68	89.9	26
(4)	0.0139	0.0395	0.723	9.68	69.7	26
HEAVY EXERCISE						
(1)	0.00840 0.514	2.20 0.000587	0.524 45.0	18.0	1.44 100.0	40
(2)	0.305	0.0395	38.5	18.0	98.1	40
(3)	0.0626	0.0395	5.23	18.0	94.8	40
(4)	0.0139	0.0395	0.919	18.0	82.8	40
MAXIMUM EXERCISE						
(1)	0.00840 0.514	2.20 0.00587	0.671 40.7	40.9	2.46 100.0	100
(2)	0.305	0.0395	31.6	40.9	99.1	100
(3)	0.0626	0.0395	4.15	40.9	97.7	100
(4)	0.0139	0.0395	0.772	40.9	91.9	100

Table 7.7: Predictions for the oxygen current and pulmonary efficiency given by the space-filling fractal Cayley tree model with $D_f = 3$. Experimental data used for comparison reported by Hou et al. [1].

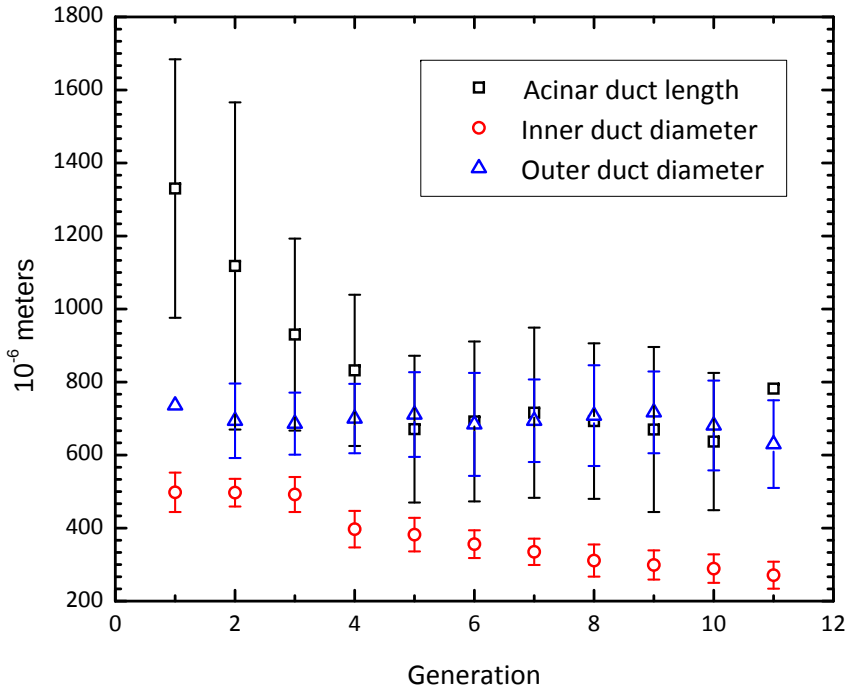

(a) Experimental data for width and length of branches within the acinus.

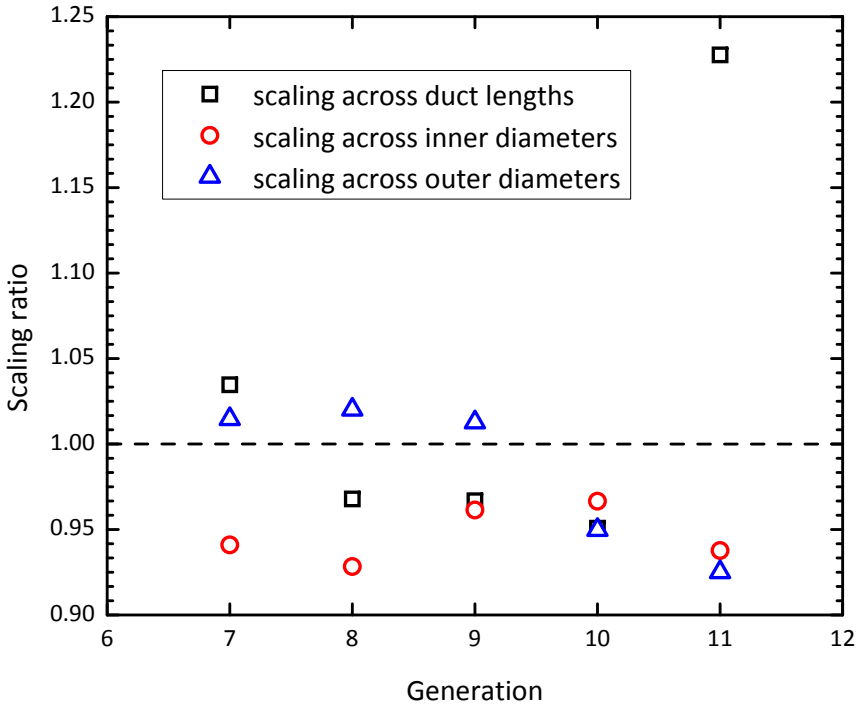

(b) Scaling ratios $q_{k+1} = R_{k+1}/R_k$ and $p_{k+1} = L_{k+1}/L_k$ within the acinar airways.

Figure 7.4: Outer diameters, inner diameters, and segment lengths of ducts within the acinar airways reproduced from data within reference [4].

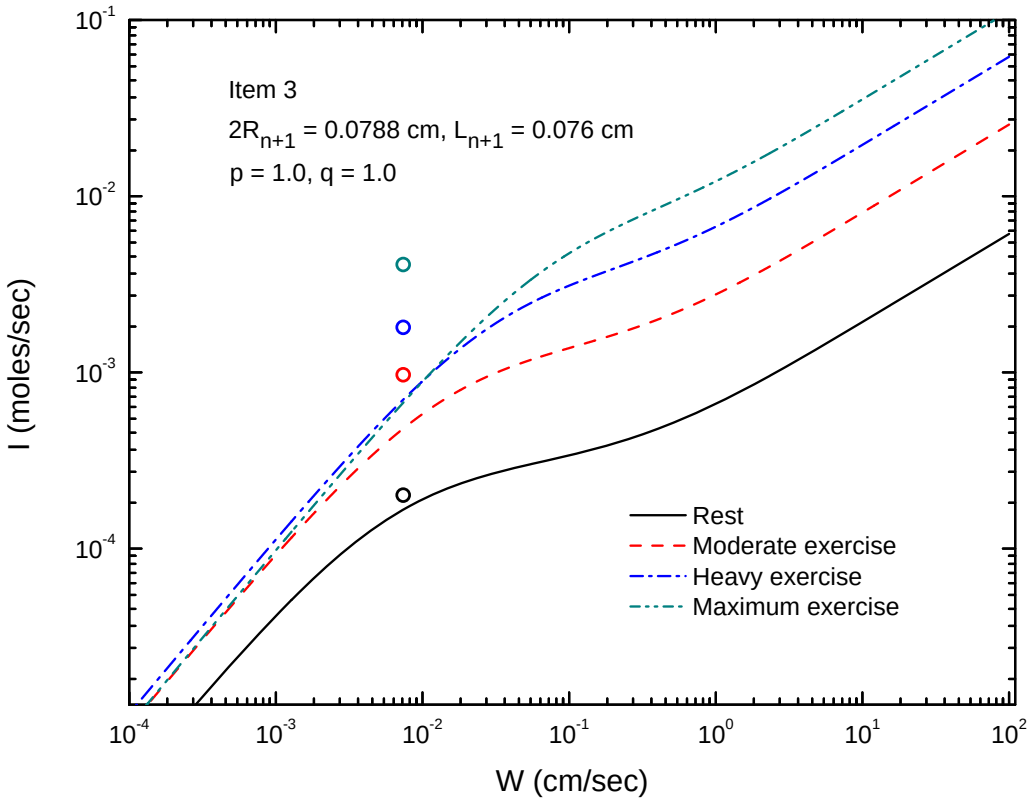

Figure 7.5: Oxygen currents predicted by the Cayley tree model with $2R_{n+1} = 0.0788$ cm and $L_{n+1} = 0.076$ cm, in the equi-length and width model. Data from experiment are represented by circles for physiological $\Lambda = 32.8$ cm.

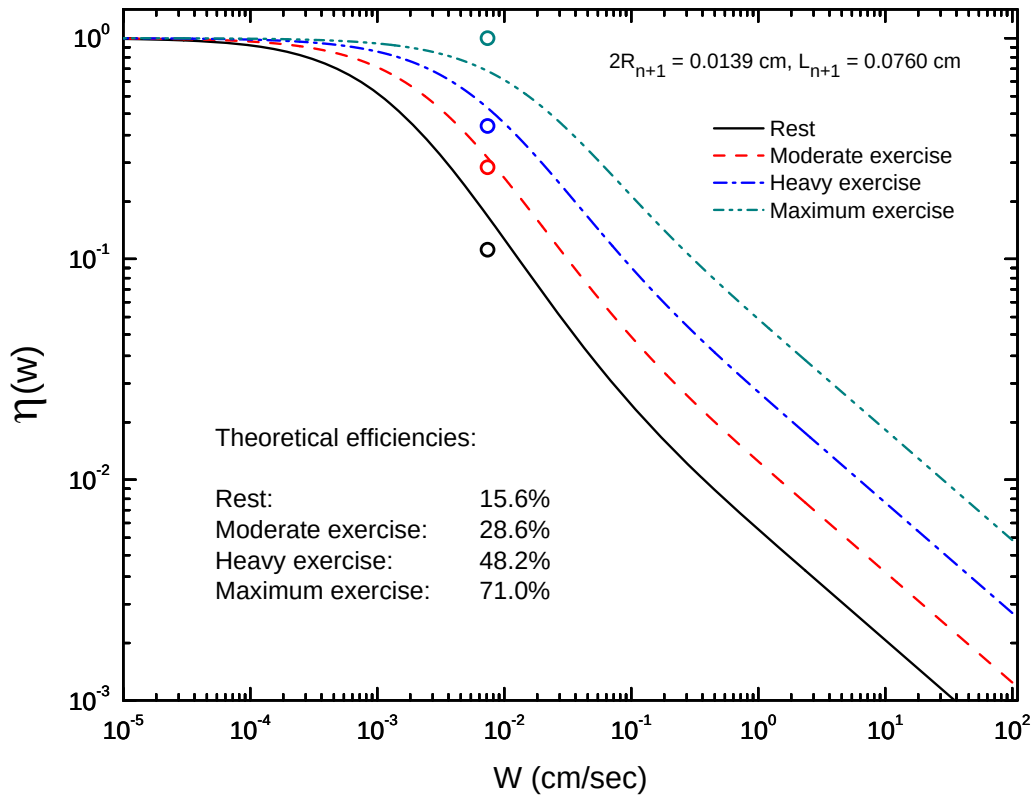

Figure 7.6: Predictions of the pulmonary efficiency in all regimes of exercise made by the equi-length and width model for physiological values of $2R_{n+1} = 0.0139$ cm and $L_{n+1} = 0.076$ cm. Data from experiment are represented by circles for physiological $\Lambda = 32.8$ cm.

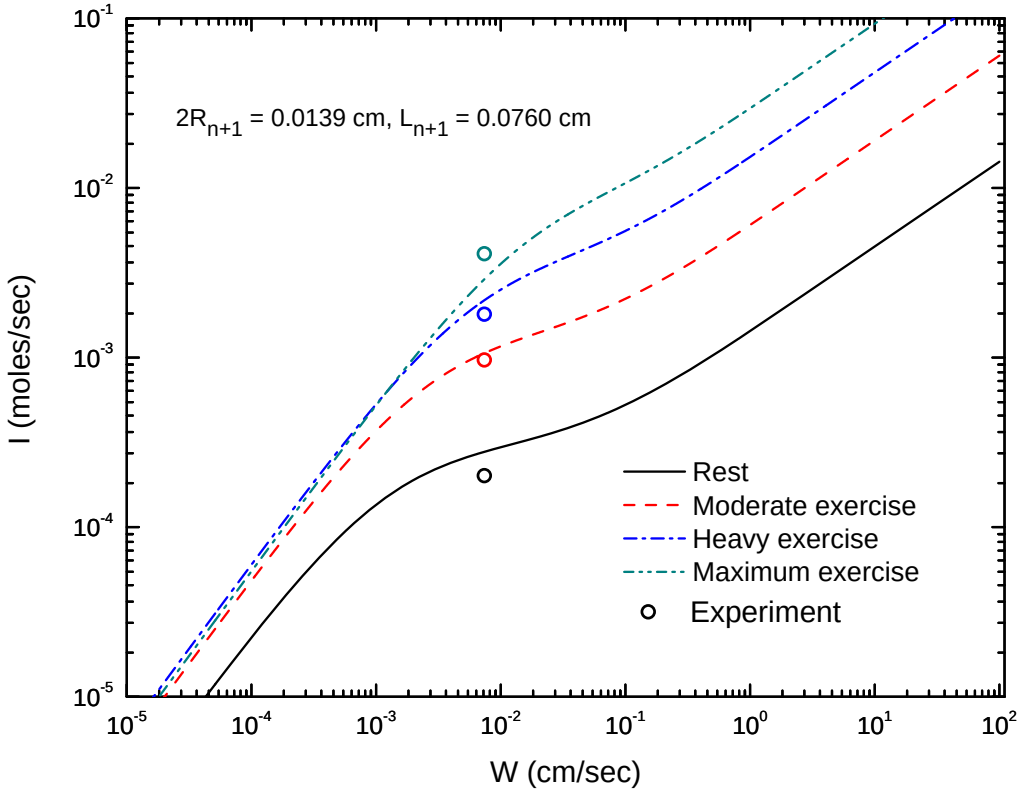

Figure 7.7: Oxygen currents in all regimes of exercise computed with Equation 7.5.13, using the efficiency of the equi-length and width Cayley tree model and data from Item (4).

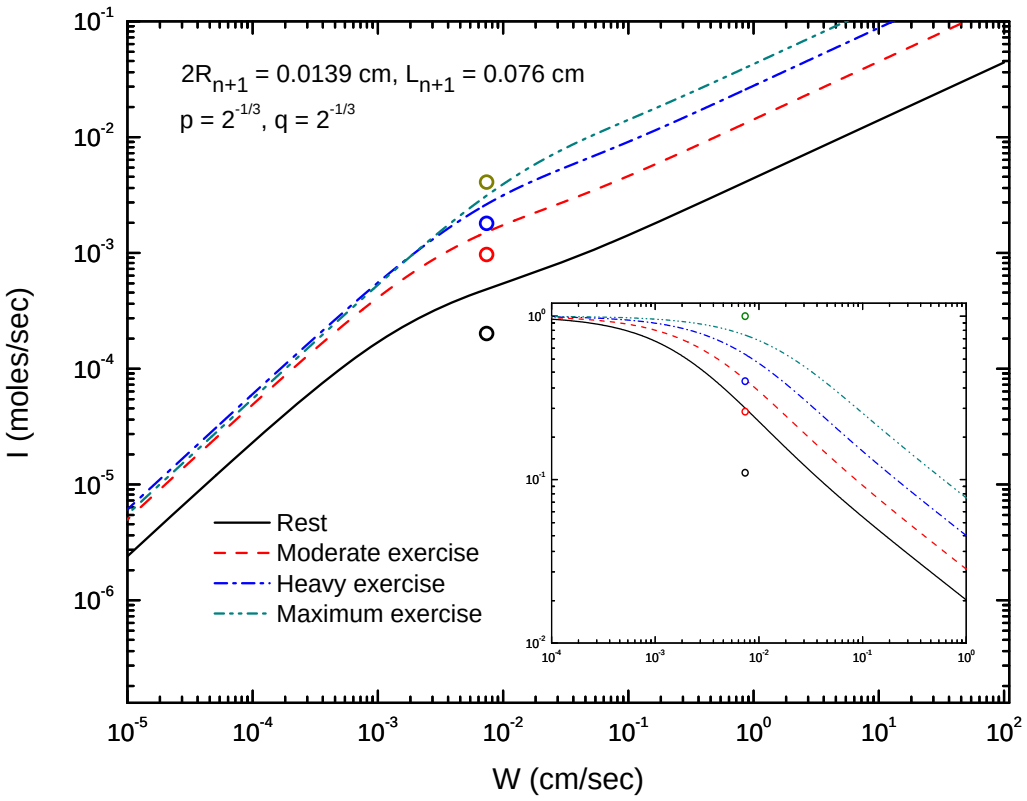

Figure 7.8: Oxygen currents in all regimes of exercise computed with Equation 7.5.13, using the efficiency of the fractal Cayley tree model with $D_f = 3$, and data from Item (4). Data from experiment are represented by circles for physiological $\Lambda = 32.8$ cm.

Chapter 8

Summary and concluding remarks

In this thesis we have developed, from the ground up, a model predicting both the oxygen current reaching the hemoglobin of the red blood cells and the pulmonary efficiency of the lung. We first developed a new model for a single acinar branch and then we derived restrictions for an approximation to the Laplacian equation of motion typically used to describe the diffusion of, and subsequent reaction of, oxygen with the alveolar membranes of the lung. This restriction is given by $R/\Lambda < 1$, which connects the structure of the branch with the transport parameters of the system.

Using our model of a single acinar branch, we developed a new anatomically branching model of the human lung acinus, and studied its properties. Specifically, we found that "smaller" trees, in a model where all branches are of equal width and length, are more efficient in transporting particles to its exterior. We also observed that "large" trees exhibit regions of permeability, in which the particle current plateaus, which demonstrates that these trees regulate the current delivered to their exterior, without the need for dynamic response of their system parameters. Specifically, we found that larger trees possessed regions insensitive to changes in permeability which were not observed in the more efficient trees. We concluded that smaller trees are more efficient, but this increase in efficiency comes at a loss of system stability against changes in its transport parameters.

We extended our model to include a fractal representation of the Cayley tree in order to study its space filling ability, and to study how such geometric configurations affect the

oxygen current reaching the blood. We found that space-filling trees ($D_f = 3$) are more efficient; however, similar to the "small" trees in the equi-length and width model, these space filling trees lose their ability to tolerate error in membrane permeability. Because there exists a finite volume between the end of the bronchial tree and the wall of the pleural cavities in the lung, we concluded that an equi-length and width model will maximally overfill the available space thus maximizing its surface area across a finite number of bifurcations. For this reason, we concluded that the human lung chooses branches that are of equal width and length to maximize its surface area, while simultaneously maximizing the homeostatic regulation of its oxygen current.

We also showed, through the equi-length and width model, that the human lung chooses $m = 2$, due to its preference for the exponential growth in the total number of its branches, $N \propto 2^n$, over a choice of polynomial growth $N \propto m^2$. An exponential growth in the number of branches across each generation not only creates a simple way to construct the tree, but also generates a tree of minimum depth, in which homeostasis emerges as a regulating mechanism of the oxygen current.

Finally, we applied physiological data to the Cayley tree model and were able to make quantitative predictions for its oxygen current, as well as make predictions for the pulmonary efficiency of the human lung. Following a simple algorithm outlined in Figure 1.1, we conducted a thorough study of the Cayley tree model under several suggested geometrical restrictions, from which we inferred the width and length of its terminal branches. Using a given width and length of the terminal branches, we predicted the oxygen current and pulmonary efficiency from the Cayley tree model with fractal dimensions $D_f \to \infty$ and $D_f = 3$.

Though we analyzed these models with several choices for the width and length of the terminal branches, we found that the model with $D_f = 3$ made predictions for the efficiencies that were generally higher than the equi-length and width model; neither the oxygen currents nor the efficiencies predicted by this model were particularly close to the experimental ones.

For the equi-length and width model we found only good agreement between the ex-

perimental values and theoretical predictions, for the pulmonary efficiency of the tree. We note that the pulmonary efficiencies computed with these physiological values of the width and length of the terminal branches, $2R_{n+1} = 0.0139$ cm and $L_{n+1} = 0.076$ cm, performed very well under all four regimes of exercise.

Independent of the model we analyzed, we found that diffusional screening plays a critical role in the regulation of the current generated by the Cayley tree. We note that perhaps the most important quantity to derive from our model is not the oxygen current, but rather the pulmonary efficiency. This is because the surface area of the alveolar membranes is crucial to the computation of the current, and the oxygen current is sensitive to poor estimates of its value. In contrast, the pulmonary efficiency may be correctly computed using unonphysical values for the surface area of the membranes, and it provides a measure of the zones active in transport. By extension, it serves as an excellent measure of those portions of the human lung relevant for transport.

Our model makes possible the quantitative study of many respiratory diseases by modeling their response as changes to the transport or structural parameters of the airways. For example, asthma affects gas exchange through the constriction of the branches in the bronchial tree and through the inflamation of the airways. Therefore, we could describe such a process using our Cayley tree model as a decrease in the generational depth of the tree coupled with a decrease in the membrane permeability. Such suggestions were first outlined by Hou and his collaborators using their renormalization treatment[1], and we apply them to our model. In Table 8.1 we present several diseases of the airways, along with an associated change in their transport or structural parameters outlined by Hou et al.[1] There are several possible avenues of investigation in which our Cayley tree model may provide further insight into the various aspects of diffusional transport in branched structures. The first of these propositions is a further analysis of the screening mechanism within the Cayley tree. The physiological value of the exploration length is approximately $\Lambda \approx 0.243/0.00739 = 32.8$ cm[1], yet the longitudinal path length of the tree is given by $L_p = 0.456$ cm[2]. It would be interesting to investigate the path distributions that diffusing particles take within the tree, and to study the dependence of such path distributions

Condition	Parameter response				
	ΔW	ΔS_{lung}	Δn	$\Delta 2R_{n+1}$	Δp
Pulmonary edema	< 0	–	–	–	–
Aerosol inhalation	< 0	< 0	–	–	–
Asthma	< 0	–	< 0	–	–
Pneumonia	< 0	–	–	< 0	–
Emphysema	–	< 0	–	–	–
Lung surgery	–	< 0	–	–	–
Hyperbaric oxygen treatment	–	< 0	–	–	> 0

Table 8.1: Respiratory diseases modeled by the Cayley tree and their associated parameter responses, first suggested by Hou et al. for use in their renormalization model of the airways.[1]

upon their chosen end points and system parameters. Such a study would be conducted by numerical simulation, and the path distributions that emerge from the Cayley tree would be compared with those found in of other geometries.

It may also be interesting to conduct a study that explored the relationship between diffusional screening and the so-called "passivation" process investigated numerically by other authors[25]. In the passivation process the permeability of the alveolar membranes becomes heterogeneous, which affects transmembrane oxygen currents local to the heterogeneity. For example if a diffusing chemical species adsorbs onto the alveolar membranes under their first impact with the membranes, then we would expect the permeability of the membranes local to these first-impacted sites to be different than the membrane permeability of the unaffected alveolar membranes.

An analytical study using our model could be conducted that explored the passivation of the alveolar membranes through the identification of its affects on the exploration length of the lung. Such an analytical study would be directly complemented by numerical simulation, possibly using the finite element method. This method relies on the discretization of the geometry into small meshes over which the diffusion-reaction equations are integrated. The number of meshes grows with system size, which has been a limiting factor in the numerical study of all but the simplest fractal geometries.

Another possible application of interest would be the exploration of bio-inspired architectures for mathematically equivalent systems, such as those in heat conduction and

Description	Symbol
Global permeability of the alveolar membranes	W
Coefficient of diffusion for oxygen in air	D
Concentration difference across the alveolar membranes	$C_{air} - C_{blood}\beta_{air}/\beta_{blood}$
Solubility of oxygen within the acinar gas	β_{air}
Solubility of oxygen on the blood side of the membranes	β_{blood}
Number of gas exchangers in the lung	N_g
Depth of the Cayley tree	n
Number of daughter branches for each branch node	m
Radius of the k^{th} branch	R_k
Length of the k^{th} branch	L_k
Scaling ratio across node generation k for branch widths	$q := R_{k+1}/R_k$
Scaling ratio across node generation k for branch lengths	$p := L_{k+1}/L_k$

Table 8.2: Parameters needed to predict the oxygen current crossing the surface of the Cayley tree model, and its efficiency.

electrochemistry. From our analysis of the human lung, we have explored properties of particle transport within the acinar airways that are applicable to identifying engineering targets for other distribution systems, in which demands for error tolerance and screening are necessary for their operation. At least one promising avenue is the application of our model to the design of efficient thermal distributors, such as heat sinks for electronic devices.

It would be a major accomplishment to extend our model to the time-dependent domain, in an effort to investigate time dependent perturbations in the mechanical stability of the alveolar membranes. Even more challenging would be the time dependent description of the transitions between regimes of exercise and its coupling to the relevant physiological mechanisms that initiate them. In particular, diseases, such as respiratory distress in infants, that lead to a change in gas exchanger volume might be modeled by the same process.

As a final remark, we provide the formulas needed to predict the oxygen current and pulmonary efficiency from our model in closed form. For a Cayley tree with $q = q^{(i)}{}_{k+1}$ and $p = p^{(i)}{}_{k+1}$ for all $i = 1, 2, \ldots, m$ and $k = 1, 2, \ldots, n$, the oxygen current and pulmonary efficiency are given by

$$I_{lung} = N_g W S_{eff,g} \left(C_{air} - C_{blood} \frac{\beta_{air}}{\beta_{blood}} \right),$$

$$\eta_{tree} = \frac{S_{eff,g}}{S_{tree}}.$$

The auxiliary expressions needed to conduct the above computations are given by:

$$
\begin{aligned}
&S_{eff,g} = \frac{D}{D_{eff}} \cdot \frac{W_{eff}}{W} \cdot \frac{\pi {R_1}^2}{mq^2}, \\
&S_{tree} = 2\pi R_1 L_1 \sum_{k=0}^{n} (mpq)^k + \pi {R_1}^2 \left(mq^2\right)^n, \\
&F_{ij}^{(k)} = \begin{pmatrix} q^{-2}\sqrt{\frac{2}{R_1\Lambda}} & q^{\frac{k-5}{2}} \tanh\left(\sqrt{\frac{2{L_1}^2}{R_1\Lambda}}(\frac{p}{\sqrt{q}})^{k-1}\right) \\ q^{\frac{1-k}{2}}\frac{2m}{R_1\Lambda}\tanh\left(\sqrt{\frac{2{L_1}^2}{R_1\Lambda}}(\frac{p}{\sqrt{q}})^{k-1}\right) & m\sqrt{\frac{2}{R_1\Lambda}} \end{pmatrix}, \\
&\prod_{k=1}^{n+1} F_{ij}^{(k)} \cdot \begin{pmatrix} D \\ W \end{pmatrix} = \begin{pmatrix} D_{eff} \\ W_{eff} \end{pmatrix}.
\end{aligned}
$$

The description of the parameters are collected in Table 8.2.

Appendix A

Concentration in the model branch

A.1 Eigenfunction expansion

Here we calculate an anlaytic expression for the oxygen concentration within a cylinder. Oxygen will propagate by diffusion from the entrance of the cylinder and ultimately react with the boundary of the cylinder to produce an oxygen current crossing the boundary. We begin with the equation of motion, the diffusion equation, for the oxygen concentration:

$$\vec{\nabla}^2 C(\vec{x}) = 0 \tag{1.1.1a}$$

$$\vec{\nabla} C(\vec{x}) \cdot \hat{n}(\vec{x}) = \frac{C(\vec{x})}{\Lambda} \text{ with } \vec{x} \text{ at the surface,} \tag{1.1.1b}$$

where $\Lambda = D/W$ is the exploration length. We will solve these equations exactly by taking advantage of the cylindrical symmetry through the following change of variables: $z = r\cos(\theta)$, $y = r\sin(\theta)$ and $x = x$, where the x-axis is the axial coordinate of the cylinder. In this coordinate system $C(\vec{x}) = C(r, \theta, x)$ and Equations 1.1.1 are given as

$$\vec{\nabla}^2 C(r, \theta, x) = 0 \tag{1.1.2a}$$

$$\vec{\nabla} C(R, \theta, x) \cdot \hat{r} = -\frac{C(R, \theta, x)}{\Lambda}, \tag{1.1.2b}$$

where we take the cylinder to have radius R and length L. We adopt the convention that the normal vector points radially inward, such that $\hat{n} = -\hat{r}$.

Boundary conditions are such that the concentration across the entrance and exit cross-sections of the cylinder depend explicitly on r and θ:

$$C(r,\theta,0) = C_{ent}(r) \tag{1.1.3a}$$

$$C(r,\theta,L) = C_{ext}(r) \tag{1.1.3b}$$

We will use the following procedure to find the solution to Equations 1.1.2 and 1.1.3; we will assume that the solution is separable, such that eigenvalued equations are applicable for each independent variable. We then solve these equations analytically and show the linear superposition of all such solutions form a vector space. The general solution will then be a projection in the vector space.

The Laplacian operator in cylindrical coordinates is

$$\vec{\nabla}^2 = \frac{1}{r}\frac{\partial}{\partial r}\left(r\frac{\partial}{\partial r}\right) + \frac{1}{r^2}\frac{\partial^2}{\partial\theta^2} + \frac{\partial^2}{\partial x^2}, \tag{1.1.4}$$

and we will assume that $C(r,\theta,x) = R(r)\Omega(\theta)X(x) \neq 0$ almost everywhere. Applying Equation 1.1.4 to Equation 1.1.2a gives

$$\frac{1}{R(r)r}\frac{\partial}{\partial r}\left(r\frac{\partial}{\partial r}R(r)\right) + \frac{1}{\Omega(\theta)r^2}\frac{\partial^2}{\partial\theta^2}\Omega(\theta) + \frac{1}{X(x)}\frac{\partial^2}{\partial x^2}X(x) = 0. \tag{1.1.5}$$

Suppose $f(x)$ and $g(y)$ are functions that can be differentiated at least twice and, for $f(x) = g(y)$, let there exist another function $h(z)$ independent of x and y such that $f(x) = g(y) = h(z)$. An obvious choice for h is one that is independent of z, and we take $h(z) =$ constant. We then express Equation 1.1.5 as

$$\frac{1}{R(r)r}\frac{\partial}{\partial r}\left(r\frac{\partial}{\partial r}R(r)\right) + \frac{1}{\Omega(\theta)r^2}\frac{\partial^2}{\partial\theta^2}\Omega(\theta) = -\alpha^2 \tag{1.1.6a}$$

$$\frac{\partial^2}{\partial x^2}X(x) = \alpha^2 X(x) \tag{1.1.6b}$$

where we have chosen the constant $h = -\alpha^2$ as the separation function. We can immediately solve Equation 1.1.6b through the following ansatz: $X(x) = e^{\beta x}$. This gives the

characteristic equation $\beta^2 - \alpha^2 = 0$, which, when solved, gives

$$X(x) = A_1 e^{\beta x} + A_2 e^{-\beta x}. \tag{1.1.7}$$

We may further separate Equation 1.1.6a by choosing the seperation function as l^2. This gives

$$r\frac{\partial}{\partial r}R(r)\left(r\frac{\partial}{\partial r}R(r)\right) + (\alpha^2 r^2 - l^2)R(r) = 0 \tag{1.1.8a}$$

$$\frac{\partial^2}{\partial \theta^2}\Omega(\theta) = -l^2\Omega(\theta) \tag{1.1.8b}$$

We assume an invariance of the concentration under a rotation of the cylinder about its axis, such that $\Omega(\theta) = \text{constant}$. A consequence is that $l^2 = 0$, and we may write Equation 1.1.8a as

$$\frac{1}{\alpha^2 r}\frac{\partial}{\partial r}\left(r\frac{\partial}{\partial r}R(r)\right) + \left(1 - \frac{l^2}{\alpha^2 r^2}\right)R(r) = 0. \tag{1.1.9}$$

Equation 1.1.9 is in the form of Bessel's differential equation [26], and has solutions $R(r) = J_l(\alpha r)$. Since $l = 0$, we find

$$R(r) = BJ_0(\alpha r), \tag{1.1.10}$$

where B and α are constants. We may construct a solution from Equation 1.1.7 and Equation 1.1.10:

$$C(r, x) = J_0(\alpha r)\left(ae^{\alpha x} + be^{-\alpha x}\right), \tag{1.1.11}$$

where $a = A_1 B$ and $b = A_2 B$ are new constants. Equation 1.1.1b provides a restriction on α:

$$\alpha_i J_1(\alpha_i R) = \frac{1}{\Lambda}J_0(\alpha_i R), \tag{1.1.12}$$

and the α_i are the ascending real positive roots of Equation 1.1.12.

Expressions in the form of Equation 1.1.12 admit only real, positive roots[23]. Therefore, they can be ordered, and we let α_1 represent the smallest such root. Since there are an infinite number of roots, there are an infinite number of solutions, and a linear combination

of these gives

$$C(r,x) = \sum_{i=1}^{\infty} J_0(\alpha_i r)\left(a_i e^{\alpha_i x} + b_i e^{-\alpha_i x}\right). \tag{1.1.13}$$

To compute the expansion coefficients we must investigate the orthogonality of the Bessel functions used in Equation 1.1.13. The first step in the determination of a_i and b_i is to show that the Bessel functions in Equation 1.1.13 are orthogonal. To this end, we rewrite Equation 1.1.9 as an eigenvalued equation:

$$\mathcal{L}R_i = -\alpha_i^2 R_i, \tag{1.1.14}$$

where $\mathcal{L}$ is the radial Laplacian operator, and $-\alpha_i^2$ is the eigenvalue spectrum associated to the operator $\mathcal{L}$. We now introduce the following theorem of orthogonality between Bessel functions:

Theorem A.1.1. *Let R_i, R_j be eigenfunctions of Equation 1.1.14, such that $R_k = J_0(\alpha_k r)$. If the inner product is given by*

$$(J_0(\alpha_i r), J_0(\alpha_j r)) := \int_0^R r J_0(\alpha_i r) J_0(\alpha_j r) dr, \tag{1.1.15}$$

then the following statements hold:

(a) $(J_0(\alpha_i r), J_0(\alpha_j r)) = 0$, *when* $i \neq j$

(b) $(J_0(\alpha_i r), J_0(\alpha_j r)) = \frac{1}{2}\left(1 + (\Lambda\alpha_i)^{-2}\right)\left(R J_0(\alpha_i R)\right)^2$, *when* $i = j$

Proof of Theorem A.1.1 (a): Since $R_i = J_0(\alpha_i r)$ and $R_j = J_0(\alpha_j r)$ are solutions to Bessel's differential equation, they can be written as:

$$\frac{R_j}{r}\frac{\partial}{\partial r}\left(r\frac{\partial}{\partial r}R_i\right) + \left(\alpha_i^2 + \frac{l^2}{r^2}\right)R_i R_j = 0 \tag{1.1.16a}$$

$$\frac{R_i}{r}\frac{\partial}{\partial r}\left(r\frac{\partial}{\partial r}R_j\right) + \left(\alpha_j^2 + \frac{l^2}{r^2}\right)R_j R_i = 0. \tag{1.1.16b}$$

Subtracting Equation 1.1.16a from 1.1.16b gives

$$r\left(\alpha_i^2-\alpha_j^2\right)R_iR_j=R_j\frac{\partial}{\partial r}\left(r\frac{\partial}{\partial r}R_i\right)-R_i\frac{\partial}{\partial r}\left(r\frac{\partial}{\partial r}R_j\right). \tag{1.1.17}$$

If we integrate both sides of Equation 1.1.17, we have:

$$\begin{aligned}\int_0^R rJ_0(\alpha_i r)J_0(\alpha_j r)dr&=\frac{R}{\alpha_i^2-\alpha_j^2}\left[J_0(\alpha_j r)\frac{\partial}{\partial r}J_0(\alpha_i r)-J_0(\alpha_i r)\frac{\partial}{\partial r}J_0(\alpha_j r)\right]_{r=0}^{r=R}\\&=0,\end{aligned}$$

where the right hand side satisfies Equation 1.1.12. □

Proof of Theorem A.1.1 (b): For the case $i=j$, we again begin with Bessel's equation and write

$$2r\left(\frac{dR_j}{dr}\right)\frac{d}{dr}\left(r\frac{d}{dr}R_j\right)+2r^2\left(\alpha_i^2-\frac{l^2}{r^2}\right)\frac{dR_j}{dr}R_j=0.$$

Since $\partial_r f^2=2f\partial_r f$, we have

$$\int_0^R r^2\frac{d}{dr}\left(R_j\right)^2dr=\frac{1}{\alpha_i^2}\left[l^2R_j^2-\left(r\frac{dR_j}{dr}\right)^2\right]_{r=0}^{r=R}$$

and the left hand side can be integrated with $r^2\frac{d}{dr}\left(R_j\right)^2=\frac{d}{dr}\left(r^2R_j^2\right)-2rR_j^2$:

$$\int_0^R rR_j^2dr=\frac{1}{2\alpha^2}\left[\left(\alpha^2r^2-l^2\right)R_j^2+r^2\left(\frac{dR_j}{dr}\right)^2\right]_{r=0}^{r=R}. \tag{1.1.19}$$

Putting the mixed boundary condition in Equation 1.1.19, we arrive at the final result:

$$\left(J_0(\alpha_i r),J_0(\alpha_i r)\right)=\frac{1}{2}\left(1+\left(\Lambda\alpha_i\right)^{-2}\right)\left(RJ_0(\alpha_i R)\right)^2.$$

□

Using Theorem A.1.1, we may expand $C(r,x)$ in Equation 1.1.13 as

$$C_{ext}(r) = \sum_{i=1}^{\infty} A_i J_0(\alpha_i r),$$

to give

$$\sum_{i=1}^{\infty} A_i J_0(\alpha_i r) = \sum_{i=1}^{\infty} J_0(\alpha_i r)\left(a_i + b_i\right). \tag{1.1.20}$$

We have shown that the Bessel functions are linearly independent; therefore the coefficients satisfy $A_i = a_i + b_i$ for each i.

Similarly, we may use $C_{ext}(r) = \sum_{i=1}^{\infty} B_i J_0(\alpha_i r)$ to produce

$$\sum_{i=1}^{\infty} B_i J_0(\alpha_i r) = \sum_{i=1}^{\infty} J_0(\alpha_i r)\left(a_i e^{\alpha_i L} + b_i e^{-\alpha_i L}\right). \tag{1.1.21}$$

Here, Equation 1.1.21 implies $B_i = a_i e^{\alpha_i L} + b_i e^{-\alpha_i L}$. We now have two equations for each of the unknown coefficients, which means that we can find unique solutions for both a_i and b_i completely in terms of A_i and B_i:

$$a_i = \frac{B_i - A_i e^{-\alpha_i L}}{e^{\alpha_i L} - e^{-\alpha_i L}} \tag{1.1.22}$$

$$b_i = \frac{A_i e^{\alpha_i L} - B_i}{e^{\alpha_i L} - e^{-\alpha_i L}}. \tag{1.1.23}$$

We can write Equation 1.1.13 in terms of A_i and B_i:

$$C(r,x) = \sum_{i=1}^{\infty} J_0(\alpha_i r)\frac{A_i \sinh\left(\alpha_i(L-x)\right) + B_i \sinh\left(\alpha_i x\right)}{\sinh\left(\alpha_i L\right)} \tag{1.1.24}$$

To compute the A_i, we expand and manipulate boundary condition 1.1.2a such that

$$rC_{ent}(r)J_0(\alpha_k r) = A_1 r J_0(\alpha_1 r)J_0(\alpha_k r) + \ldots + A_k r J_0(\alpha_k r)J_0(\alpha_k r) + \ldots. \tag{1.1.25}$$

If we integrate both sides and apply Theorem A.1.1, then we find a solution for A_k:

$$A_k = 2\left(R^2 J_0^2(\alpha_j R)\left(1 + \frac{1}{\Lambda^2 \alpha_k^2}\right)\right)^{-1} \int_0^R dr r C_{ent}(r) J_0(\alpha_k r). \tag{1.1.26}$$

Similarly,

$$B_k = 2\left(R^2 J_0^2(\alpha_j R)\left(1+\frac{1}{\Lambda^2\alpha_k^2}\right)\right)^{-1}\int_0^R drrC_{ext}(r)J_0(\alpha_k r), \tag{1.1.27}$$

for each $k = 1, 2, \ldots$.

The final solution is

$$C(r,x) = \sum_{i=1}^{\infty}\left(\frac{2}{R^2}\right)\frac{\delta_i^2 J_0(\delta_i\frac{r}{R})\left(f_i(R)\sinh\left(\delta_i\frac{L-x}{R}\right)+g_i(R)\sinh\left(\delta_i\frac{x}{R}\right)\right)}{J_0^2(\delta_i)\sinh\left(\delta_i\frac{L}{R}\right)\left(\delta_i^2+\left(\frac{R}{\Lambda}\right)^2\right)} \tag{1.1.28}$$

$$f_i(R) := \int_0^R rC_{ent}(r)J_0\left(\delta_i\frac{r}{R}\right)dr \tag{1.1.29}$$

$$g_i(R) := \int_0^R rC_{ext}(r)J_0\left(\delta_i\frac{r}{R}\right)dr, \tag{1.1.30}$$

where $\delta_i := \alpha_i R$ are the ascending roots of

$$\delta_i J_1(\delta_i) = \frac{R}{\Lambda}J_0(\delta_i). \tag{1.1.31}$$

Appendix B

Hierarchical solution for the fractal Cayley tree

B.1 About notation

We adopt the following notation for both the concentrations and currents within the cylinders: $C^{(j)}_{ent/ext,k}$ and $I^{(j)}_{ent/ext,k}$, respectively. In general, these labels take the following form:

$$A^{(j)}_{ent/ext,k},$$

where the superscript denotes the j^{th} daughter branch associated attached at its entrance to the $k-1^{st}$ node, where $k = 1, 2, \ldots, n+1$.

Subscripts ent/ext denote the position of the concentration or current within each branch, with respect to the entrance and exit. We will not consider currents or concentrations which are intermediate to the end points of each branch. In many cases it will be clear which of the branches are parent branches and which are daughter branches, without the use of separate notation. Where the branches are ambiguous, we will clearly note the hierarchy of the tree's parameters.

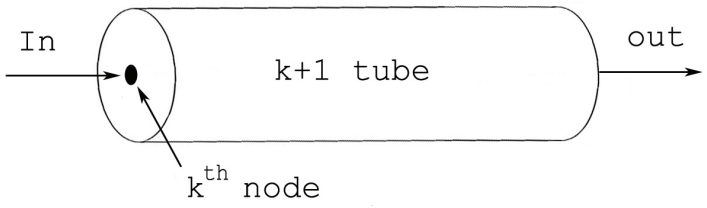

Figure B.1: Labeling of nodes and branchs in the cayley tree.

B.2 Renormalization treatment on the tree

Consider the terminal branches of the Cayley tree, where the concentrations across the terminal cross-sections are given by boundary conditions:

$$\partial_x C^{(j)}_{n+1}(x)|_{x=0} = -\frac{I^{(j)}_{ent,n+1}}{DS^{(j)}_{n+1}}, \tag{2.2.1a}$$

$$C^{(j)}_{n+1}(x)|_{x=L} = \frac{I^{(j)}_{ext,n+1}}{WS^{(j)}_{n+1}}, \tag{2.2.1b}$$

and $S_{n+1} = \pi {R^{(j)}_{n+1}}^2$ is the cross-section of a terminal branch.

In solving the equation of motion, Equation 4.2.3, we apply the boundary conditions to arrive at the following results for the terminal branch:

$$C^{(j)}_{ent,n+1} = \frac{\tanh\left(\lambda^{(j)}_{n+1}L^{(j)}_{n+1}\right)}{\lambda^{(j)}_{n+1}DS^{(j)}_{n+1}} I^{(j)}_{ent,n+1} + \frac{\Lambda}{DS^{(j)}_{n+1}\cosh\left(\lambda^{(j)}_{n+1}L^{(j)}_{n+1}\right)} I^{(j)}_{ext,n+1}, \tag{2.2.2a}$$

$$I^{(j)}_{ent,n+1} = \left(\cosh\left(\lambda^{(j)}_{n+1}L^{(j)}_{n+1}\right) + \Lambda\lambda^{(j)}_{n+1}\sinh\left(\lambda^{(j)}_{n+1}L^{(j)}_{n+1}\right)\right) I^{(j)}_{ext,n+1}, \tag{2.2.2b}$$

where

$$\lambda^{(j)}_{n+1} = \sqrt{\frac{2}{\Lambda R^{(j)}_{n+1}}}. \tag{2.2.3}$$

We are interested in finding $I^{(j)}_{ent,n+1}$ as a function of entrance concentration, which we can find through Equation 2.2.2a and Equation 2.2.2b as

$$I^{(j)}_{ent,n+1} = \frac{DS^{(j)}_{n+1}\lambda^{(j)}_{n+1}\left(1 + \Lambda\lambda^{(j)}_{n+1}\tanh\left(\lambda^{(j)}_{n+1}L^{(j)}_{n+1}\right)\right)}{\Lambda\lambda^{(j)}_{n+1} + \tanh\left(\lambda^{(j)}_{n+1}L^{(j)}_{n+1}\right)} C^{(j)}_{ent,n+1}.$$

We may now write the entrance current as

$$I^{(j)}_{ent,n+1} = \frac{DS^{(j)}_{n+1}}{f^{(j)}_{n+1}(\Lambda)} C^{(j)}_{ent,n+1}, \tag{2.2.4}$$

where we define the effective exploration length, $f^{(j)}_{n+1}(\Lambda)$, as

$$f^{(j)}_{n+1}(\Lambda) := \frac{\Lambda\lambda^{(j)}_{n+1} + \tanh\left(\lambda^{(j)}_{n+1} L^{(j)}_{n+1}\right)}{\lambda^{(j)}_{n+1}\left(\Lambda\lambda^{(j)}_{n+1}\tanh\left(\lambda^{(j)}_{n+1} L^{(j)}_{n+1}\right) + 1\right)}. \tag{2.2.5}$$

Through Equation 2.2.4 the tree original tree has been renormalized and describes a new tree of depth $n-1$. In this picture, the current which is leaving through the n^{th} node is the current which is attenuated by the surface the branches in the $n+1$ generation.

B.2.1 Terminal branches

In the previous section we found that in order to describe the current leaving through a terminal cylinder, we only need to compute the effective exploration length $\Lambda \mapsto f^{(j)}_{n+1}(\Lambda)$. In order to propagate back through the tree, we must cross the node junction. Two conditions hold at each node within the tree, and are the Cayley tree analogue of Kirchoff's laws in electrical circuits:

$$C_{ext,k-1} = C^{(1)}_{ent,k} = C^{(2)}_{ent,k} = \cdots = C^{(m)}_{ent,k} \tag{2.2.6a}$$

$$\begin{aligned} I_{ext,k-1} &= \sum_{j=1}^{m} I^{(j)}_{ent,k}, \\ &= D\sum_{j=1}^{m} \frac{S^{(j)}_k C^{(j)}_{ent,k}}{f^{(j)}_k(\Lambda)}. \end{aligned} \tag{2.2.6b}$$

At each node $k-1$, Equation 2.2.6a is a statement of continuity in the concentration, and Equation 2.2.6b is a statement of current conservation. Applying these conditions to Equation 2.2.4 gives

$$I_{ext,n} = DC_{ext,n}\sum_{j=1}^{m} \frac{S^{(j)}_{n+1}}{f^{(j)}_{n+1}(\Lambda)}.$$

At this point, we will make several assumptions that will greatly simplify our calculations

and complement our intuitive picture of the Cayley tree. For each $k \in \{1, 2, \ldots, n+1\}$, we take daughter branches to be equal. In other words, $R_k^{(1)} = R_k^{(2)} = \cdots = R_k^{(m)} = R_k$ and $L_k^{(1)} = L_k^{(2)} = \cdots = L_k^{(m)} = L_k$. We may therefore drop the superscript that will uniquely identify an individual daughter branch at the $k-1^{th}$ node. Applying these relations to Equation B.2.1, we find

$$I_{ext,n} = \frac{DS_{n+1}}{\tilde{f}_{n+1}(\Lambda)} C_{ext,n}, \tag{2.2.7}$$

where we have defined, for convenience, $\tilde{f}_{n+1}(\Lambda) := f_{n+1}(\Lambda)/m$.

B.2.2 Intermediate branches

We will continue to propagate the oxygen current back through the tree, and as a goal, we will obtain an expression for $I_{ent,1}$ in terms of $C_{ent,1}$. We begin by reporting the concentrations and currents within the intermediate branch connected to the terminal cylinders:

$$C_{ent,n} = \frac{\cosh(\lambda_n L_n) I_{ent,n} - I_{ext,n}}{\lambda_n DS_n \sinh(\lambda_n L_n)}, \tag{2.2.8a}$$

$$C_{ext,n} = \frac{I_{ent,n} - \cosh(\lambda_n L_n) I_{ext,n}}{\lambda_n DS_n \sinh(\lambda_n L_n)}, \tag{2.2.8b}$$

$$I_{ext,n} = \frac{DS_{n+1}}{\tilde{f}_{n+1}(\Lambda)} C_{ext,n}. \tag{2.2.8c}$$

Using the above expressions, we can solve for the entrance current in terms of the entrance concentration:

$$\begin{aligned} I_{ent,n} &= \frac{\left(\tilde{f}_{n+1}(\Lambda)\frac{S_n}{S_{n+1}}\right)\tanh(\lambda_n L_n) + 1}{\left(\tilde{f}_{n+1}(\Lambda)\frac{S_n}{S_{n+1}}\right) + \tanh(\lambda_n L_n)} DS_n C_{ent,n} \\ &= \frac{DS_n}{f_n \circ \frac{S_n}{S_{n+1}} \tilde{f}_{n+1}(\Lambda)} C_{ent,n}. \end{aligned} \tag{2.2.9a}$$

Equation 2.2.9a is of the form $I_{ext,n} = DS_n C_{ent,n}/\Lambda_{eff}$, and by inspection, we find that the effective exploration length is given by

$$\Lambda_{eff} = f_n \circ \frac{S_n}{S_{n+1}} \tilde{f}_{n+1}(\Lambda).$$

We can continue this iterative procedure back through the intermediate branches of the tree, where we find that the current is

$$I_{ent,k} = \frac{DS_k C_{ent,k}}{f_k \circ \frac{S_k}{S_{k+1}} \tilde{f}_{k+1} \circ \cdots \circ \frac{S_n}{S_{n+1}} \tilde{f}_{n+1}(\Lambda)}, \tag{2.2.10}$$

where $k \in \{2, 3, \ldots, n\}$ labels the chosen intermediate branch. This expression does yet not extend to $k = 1$.

B.2.3 Entrance branch

For the single entrance branch, we have

$$I_{ent,1} = \lambda_1 D S_1 \tanh(\lambda L) C_{ent,1} + \frac{I_{ext,1}}{\cosh(\lambda_1 L_1)} \tag{2.2.11a}$$

$$C_{ext,1} = \frac{C_{ent,1}}{\cosh(\lambda_1 L_1)} - \frac{\tanh(\lambda_1 L_1) I_{ext,1}}{\lambda_1 D S_1} \tag{2.2.11b}$$

$$I_{ext,1} = \frac{DS_2 C_{ext,1}}{\tilde{f}_2 \circ \frac{S_2}{S_3} \tilde{f}_3 \circ \cdots \circ \frac{S_n}{S_{n+1}} \tilde{f}_{n+1}(\Lambda)}. \tag{2.2.11c}$$

The solution for $I_{ent,1}$ in terms of $C_{ent,1}$ is straight-forward, and we find that

$$I_{ent,1} = \frac{DS_1 C_{ent,1}}{f_1 \circ \frac{S_1}{S_2} \tilde{f}_2 \circ \cdots \circ \frac{S_n}{S_{n+1}} \tilde{f}_{n+1}(\Lambda)}. \tag{2.2.12}$$

We can now describe the current entering the tree by applying our analogue of Kirchoff's laws to Equation 2.2.12. We find

$$I = \frac{DS_1 C_{ent}}{m\tilde{f}_1 \circ \frac{S_1}{S_2} \tilde{f}_2 \circ \cdots \circ \frac{S_n}{S_{n+1}} \tilde{f}_{n+1}(\Lambda)}, \tag{2.2.13}$$

where we've labeled $I = I_{ext,0}$, and $C_{ent} = C_{ext,0}$. We are now in a position to apply the scaling ratios p and q to the current and formulate an expression for the current across the fractalized Cayley tree.

B.3 Current across the fractalized Cayley tree

In chapter 5 we discussed the geometry of the Cayley tree. Here we use these results to extend Equation 2.2.13 to non-integer topological dimension. Recall from Equations 5.2.1 and 5.2.2 that $p_{k+1} = L_{k+1}/L_k$, and $q_{k+1} = R_{k+1}/R_k$, respectively. In the exposition that follows, we will take the scaling ratios across each branch generation $k \in \{1, 2, \ldots, n\}$ to be equal to all others in the tree; i.e. $p = p_2 = \cdots p_{n+1}$ and $q = q_2 = \cdots q_{n+1}$. We may then write the ratio of the cross-sectional areas, which appear within Equation 2.2.13, for each branch k, as

$$\begin{aligned} \frac{S_k}{S_{k+1}} &= \left(\frac{R_k}{R_{k+1}}\right)^2 \\ &= \frac{1}{q^2}. \end{aligned} \tag{2.3.14a}$$

For organizational convenience, we write Equation 2.2.13 as

$$I = \frac{D\pi {R_1}^2 C_{ent}}{mq^2} \cdot \frac{W_{eff}}{D_{eff}}, \tag{2.3.15}$$

where

$$\frac{D_{eff}}{W_{eff}} = \frac{\tilde{f}_1}{q^2} \circ \frac{\tilde{f}_2}{q^2} \circ \cdots \circ \frac{\tilde{f}_{n+1}(\Lambda)}{q^2}. \tag{2.3.16}$$

We will continue our discussion by describing D_{eff}/W_{eff} in the Möbius representation and express the result as a p, q-dependent matrix.

B.3.1 Möbius representation

The Möbius matrix associated with the map $\tilde{f}_k/q^2$ is given by

$$F_{ij}^{(k)} = \begin{pmatrix} \lambda_k & \tanh(\lambda_k L_k) \\ mq^2{\lambda_k}^2 \tanh(\lambda_k L_k) & mq^2\lambda_k \end{pmatrix}$$

$$= \begin{pmatrix} q^{-2}\lambda_1 & q^{\frac{k-5}{2}} \tanh\left(\lambda_1 L_1 (\frac{p}{\sqrt{q}})^{k-1}\right) \\ q^{\frac{1-k}{2}} m{\lambda_1}^2 \tanh\left(\lambda_1 L_1 (\frac{p}{\sqrt{q}})^{k-1}\right) & m\lambda_1 \end{pmatrix}, \qquad (2.3.17a)$$

where $\lambda = \sqrt{2/R\Lambda}$, and we have used the definition of the scaling exponents to express the k^{th} length and width of a branch in terms of the entrance branch: $L_k/L_1 = p^{k-1}$ and $R_k/R_1 = q^{k-1}$, respectively. D_{eff}/W_{eff} may be computed using Equation 2.3.17a:

$$\prod_{k=1}^{n+1} {F_{ij}}^{(k)} \cdot \begin{pmatrix} D \\ W \end{pmatrix} = \begin{pmatrix} D_{eff} \\ W_{eff} \end{pmatrix}. \qquad (2.3.18)$$

B.4 Solution across the symmetric tree: the equi-length and width model

An analytic solution exists for the choice $p = q = 1$. We may compute the current using the orbits of $\tilde{f}$:

$$I(\Lambda) = \frac{D\pi {R_1}^2 C_{ent}}{m\tilde{f}^{n+1}(\Lambda)}, \qquad (2.4.19)$$

where

$$\tilde{f}^{n+1}(\Lambda) = \tilde{f} \circ \tilde{f} \circ \cdots \circ \tilde{f}(\Lambda). \qquad (2.4.20)$$

In the above expression,

$$\tilde{f}(\Lambda) := \frac{\lambda\Lambda + \tanh(\lambda L)}{m\lambda^2 \tanh(\lambda L)\Lambda + m\lambda}. \qquad (2.4.21)$$

We may write the Möbius matrix for $p = q = 1$ as

$$F_{ij} = \begin{pmatrix} \lambda \cosh(\lambda L) & \sinh(\lambda L) \\ m\lambda^2 \sinh(\lambda L) & m\lambda \cosh(\lambda L) \end{pmatrix}, \tag{2.4.22}$$

where $R_i = R$ and $L_i = L$ for all $i = 1, 2, \ldots, n+1$, and $\lambda = \sqrt{2\ R\Lambda}$.

According to Equation 2.3.18, we calculate the current by computing powers of the matrix given by Equation 2.4.22. To this end, Equation 2.4.22 can be diagnolized yielding an analytic expression for Equation 2.3.18. If $p = q = 1$, we can write Equation 2.3.18 as

$$\prod_{k=1}^{n+1} {F_{ij}}^{(k)} \cdot \begin{pmatrix} D \\ W \end{pmatrix} = {F^{n+1}}_{ij} \cdot \begin{pmatrix} D \\ W \end{pmatrix}.$$

Diagonalizing F_{ij} allows one to forumulate an analytic expression for ${F_{ij}}^{n+1}$. To illustrate this, let D_{ij} be diagonal, such that F_{ij} can be decomposed as

$$F_{ij} = P_{ik} D_{kl} {P^{-1}}_{lj},$$

therefore, ${F^{n+1}}_{ij} = P_{ik} {D^{n+1}}_{kl} {P^{-1}}_{lj}$, since $P_{ik} {P^{-1}}_{kj} = {P^{-1}}_{ik} P_{kj} = \delta_{ij}$ is the Kronecker delta, and serves as the identity. The diagonalized matrix has the form

$$D_{kl} = \begin{pmatrix} \zeta_+ & 0 \\ 0 & \zeta_- \end{pmatrix}, \tag{2.4.23}$$

where $\zeta_\pm$ are the eigenvalues of F_{ij} and satisfy $F_{ij} Q_{j,\pm} = \zeta_\pm Q_{j,\pm}$. Here $Q_{j,\pm}$ are the eigenvectors associated to each respective eigenvalue, and are used to construct the unitary matrix P_{ij}. The eigenvalues of F_{ij} are given by

$$\zeta_\pm = \frac{\lambda}{2} \cdot \left((m+1)\cosh(\lambda L) \pm \sqrt{((m+1)\cosh(\lambda L))^2 - 4m} \right), \tag{2.4.24}$$

and its eigenvectors are given by

$$Q_{j,+} = \begin{pmatrix} \sinh(\lambda L) \\ \zeta_+ - \lambda \cosh(\lambda L) \end{pmatrix}, \tag{2.4.25a}$$

$$Q_{j,-} = \begin{pmatrix} \zeta_- - m\lambda \cosh(\lambda L) \\ m\lambda^2 \sinh(\lambda L) \end{pmatrix}. \tag{2.4.25b}$$

We can now write the unitary matrix in terms of the eignvectors:

$$P_{ij} = \begin{pmatrix} \sinh(\lambda L) & \zeta_- - m\lambda \cosh(\lambda L) \\ \zeta_+ - \lambda \cosh(\lambda L) & m\lambda^2 \sinh(\lambda L) \end{pmatrix}, \tag{2.4.26}$$

while its inverse is given by

$${P^{-1}}_{ij} = \begin{pmatrix} m\lambda^2 \sinh(\lambda L) & m\lambda \cosh(\lambda L) - \zeta_- \\ \lambda \cosh(\lambda L) - \zeta_+ & \sinh(\lambda L) \end{pmatrix}. \tag{2.4.27}$$

In Equation 2.4.27, we exclude its determinant because it multiplies all four of its entries. Therefore, after we map the result back to $\tilde{f}$, any common prefactor will divide out. In this way, we consider any operation on the Möbius matrix that results in such an arbitrary prefactor to be a symmetry operation. We are restricted, however, to such cases in which $\det(P_{ij}) \neq 0$ so that P_{ij} is invertible.

We are now in a position to compute ${F_{ij}}^{n+1}$ as

$${F^{n+1}}_{ij} = P_{ik} \cdot \begin{pmatrix} {\zeta_+}^{n+1} & 0 \\ 0 & {\zeta_-}^{n+1} \end{pmatrix} \cdot {P^{-1}}_{lj}, \tag{2.4.28}$$

and its entries can be calculated analytically. We find these to be

$$F^{n+1}{}_{11} = {\zeta_+}^{n+1} m\lambda^2 \left(\sinh\left(\lambda L\right)\right)^2 + {\zeta_-}^{n+1} \left(\zeta_- - m\cosh\left(\lambda L\right)\right)\left(\lambda\cosh\left(\lambda L\right) - \zeta_+\right), \tag{2.4.29a}$$

$$F^{n+1}{}_{12} = {\zeta_+}^{n+1} \sinh\left(\lambda L\right)\left(m\lambda\cosh\left(\lambda L\right) - \zeta_-\right) + {\zeta_-}^{n+1} \sinh\left(\lambda L\right)\left(\zeta_- - m\lambda\cosh\left(\lambda L\right)\right), \tag{2.4.29b}$$

$$F^{n+1}{}_{21} = m\lambda^2 \sinh\left(\lambda L\right)\left(\zeta_+ - \lambda\cosh\left(\lambda L\right)\right)\left({\zeta_+}^{n+1} - {\zeta_-}^{n+1}\right), \tag{2.4.29c}$$

$$F^{n+1}{}_{22} = {\zeta_-}^{n+1} m\lambda^2 \left(\sinh\left(\lambda L\right)\right)^2 - {\zeta_+}^{n+1} \left(\zeta_- - m\cosh\left(\lambda L\right)\right)\left(\lambda\cosh\left(\lambda L\right) - \zeta_+\right). \tag{2.4.29d}$$

The Möbius matrix with elements given by Equation 2.4.29 can be connected to $\tilde{f}^{n+1}(\Lambda)$ through

$$\tilde{f}^{n+1}\left(\Lambda\right) = \frac{D_{eff}}{W_{eff}} = \frac{F^{n+1}{}_{11}\Lambda + F^{n+1}{}_{12}}{F^{n+1}{}_{21}\Lambda + F^{n+1}{}_{22}},$$

and simplifying this expression gives

$$\tilde{f}^{n+1}(\Lambda) = \frac{\frac{\sinh\left(\lambda L\right)}{\lambda} + \frac{\Lambda}{2}\left(\left(-m+1\right)\cosh\left(\lambda L\right) + \sqrt{\cdot}\right) + \frac{\Lambda\sqrt{\cdot}}{\left(\frac{1}{4m}\left(\left(m+1\right)\cosh\left(\lambda L\right)+\sqrt{\cdot}\right)^2\right)^{n+1}-1}}{m\lambda\Lambda\sinh\left(\lambda L\right) + \frac{1}{2}\left(\left(m-1\right)\cosh\left(\lambda L\right) + \sqrt{\cdot}\right) + \frac{\sqrt{\cdot}}{\left(\frac{1}{4m}\left(\left(m+1\right)\cosh\left(\lambda L\right)+\sqrt{\cdot}\right)^2\right)^{n+1}-1}},$$

where

$$\sqrt{\cdot} := \sqrt{\left(m+1\right)^2\cosh^2\left(\lambda L\right) - 4m},$$

and $\lambda = \sqrt{2/R\Lambda}$.

Bibliography

[1] C. Hou, S. Gheorghiu, V.H. Huxley, and P. Pfeifer. Reverse engineering of oxygen transport in the lung: Adaptation to changing demands through space-filling networks. Unpublished.

[2] E. R. Weibel, B. Sapoval, and M. Filoche. Design of peripheral airways for efficient gas exchange. *Respiratory Physiology and Neurobiology*, 148:3–21, 2005.

[3] E. R. Weibel. *The Pathway for Oxygen.* Harvard University Press, Cambridge, MA and London, England, first edition, 1984.

[4] B. Haefeli-Bleuer and E. R. Weibel. Morphometry of the human pulmonary acinus. *The Anatomical Record*, 220:401–414, 1988.

[5] M. Felici, M. Filoche, and B. Sapoval. Renormalized random walk study of oxygen absorption in the human lung. *Physical Review Letters*, 92(6):068101, Feb 2004.

[6] M. Felici, M. Filoche, C. Straus, T. Similowski, and B. Sapoval. Diffusional screening in real 3d human acinia theoretical study. *Respiratory Physiology and Neurobiology*, 145:279–293, 2005.

[7] D. S. Grebenkov. What makes a boundary less accessible. *Physical Review Letters*, 95(20):200602, 2005.

[8] B. Mauroy, M. Filoche, J. S. Andrade Jr., and B. Sapoval. Interplay between geometry and flow distribution in an airway tree. *Physical Review Letters*, 90(14):148101, Apr 2003.

[9] B. Sapoval, M. Filoche, and E. R. Weibel. Smaller is better-but not too small: A physical scale for the design of the mammalian pulmonary acinus. *Proceedings of the National Academy of Sciences of the United States of America*, 99:10411–10416, July 2002.

[10] C. Hou. *Scaling Laws for Oxygen Transport Across the Space-Filling System of Respiratory Membranes in the Human Lung.* PhD dissertation, University of Missouri, Department of Physics and Astronomy, 2005.

[11] D. S. Grebenkov, M. Filoche, B. Sapoval, and M. Felici. Diffusion-reaction in branched structures: Theory and application to the lung acinus. *Physical Review Letters*, 94(5):050602, 2005.

[12] P. Pfeifer and B. Sapoval. Optimization of diffusive transport to irregular surfaces with low sticking probability. In *Materials Research Society Symposium - Proceedings*, volume 366, pages 271–276, Boston, MA, USA, 28 Nov 1994 to 1 Dec 1995 1994.

[13] P. Pfeifer and P. J. Hagerty. *Screening Transition in Diffusion To and Across Fractal Surfaces*, volume 2 of *Fractals and Chaos in Chemical Engineering.* World Scientific, Rome, Italy, second edition, September 1997.

[14] B. Sapoval, M. H. A. S. Costa, J. S. Andrade Jr., and M. Filoche. Laplacian transport towards partially passivated 2d irregluar interfaces: A conjectural extension of the makarov theorem. *Fractals*, 12:381–387, 2004.

[15] B. Sapoval. General formulation of laplacian transfer across irregular surfaces. *Physical Review Letters*, 73(24):3314–3316, December 1994.

[16] E. R. Weibel. *Symmorphosis: On Form and Function in Shaping Life.* Harvard University Press, Cambridge, MA and London, England, first edition, 2000.

[17] H. Risken. *The FokkerPlanck Equation: Methods of Solutions and Applications.* Springer-Verlag, New York, NY, second edition, September 1996.

[18] P. Pfeifer, K-Y Liu, and P. J. Hagerty. Wetting transition and screening transition on fractal surfaces: Critical phenomena which do not exist on flat surfaces. Unpublished.

[19] M. Filoche and B. Sapoval. Transfer across random versus deterministic fractal interfaces. *Physical Review Letters*, 84(25):5776–5779, Jun 2000.

[20] C. Hou, S. Gheorghui, M-O Coppens, V. H. Huxley, and P. Pfeifer. *Gas Diffusion through the Fractal Landscape of Lung: How Deep Does Oxygen Enter the Alveolar System?*, volume 4 of *Fractals in Biology and Medicine*. Birkhauser Verlag, Basel, Switzerland, first edition, 2005.

[21] J. S. Andrade Jr., M. Filoche, and B. Sapoval. Analytical approximation for diffusion-reaction processes in rough pores. *Europhysics Letters*, 55:573–579, 2001.

[22] K. Falconer. *Fractal Geometry: Mathematical Foundations and Applications*. John Wiley and Sons, West Sussex, England, March 1993.

[23] G. N. Watson. *A treatise on the theory of Bessel functions*. Cambridge University Press, second edition, 1966.

[24] B. Mandelbrot. *The Fractal Geometry of Nature*. W. H. Freeman, 1983.

[25] M. Filoche, D. S. Grebenkov, J. S. Andrade Jr., and B. Sapoval. Passivation of irregular surfaces accessed by diffusion. *Proceedings of the National Academy of Sciences of the United States of America*, 105(22):7636–7640, June 2008.

[26] M. Abramowitz and I. A. Stegun. *Handbook of Mathematical Functions*. Dover, New York, NY, June 1965.

VITA

Michael Louis Mayo was born April 24^{th} 1979 in Charleston, South Carolina. He graduated in August of 2002 with a Bachelor of Science degree in physics from the University of Wyoming, Laramie. He joined the Department of Physics and Astronomy at the University of Missouri in August of 2004, where he received a Master of Science degree in May of 2006. He began working with Dr. Peter Pfeifer in January of 2006, and graduated with a Doctor of Philosophy degree in physics in July of 2009.

He is married to Anne Marie Mayo and they welcomed their son, Isaac Joseph Mayo, into the world on May 5^{th} 2009 at the Columbia Regional Medical Center in Columbia Missouri.